Exploring molecular ion formation, trapping and detection in hybrid system

by

Jyothi S

a thesis submitted to
Jawaharlal Nehru University
for the degree of

Doctor of Philosophy

2015

Raman Research Institute
Bangalore 560 080
India

Declaration

I hereby declare that the work reported in this thesis is entirely original. This thesis has been composed by me at Raman Research Institute under the supervision of Dr. S. A. Rangwala. I further declare that, to my best knowledge, the matter presented in this thesis has not formed the basis for the award of any degree, diploma, membership, associateship, fellowship or any other similar title of any university or institution. I also declare that I have run it through **Turnitin** plagiarism detection software.

Jyothi S

Countersigned:

Dr. S. A. Rangwala
Light and Matter Physics Group
Raman Research Institute
Bangalore-560 080

Certification

This is to certify that the thesis titled **"Exploring molecular ion formation, trapping and detection in hybrid system"** submitted by Jyothi S for the award of the degree of Doctor of Philosophy of Jawaharlal Nehru University is a bona-fide work. This has not been submitted to any other university for any other degree, diploma or title.

Dr. S. A. Rangwala
(Thesis Supervisor)
Light and Matter Physics Group
Raman Research Institute
Bangalore-560 080

Prof. Ravi Subrahmanyan
Director
Raman Research Institute
Bangalore-560 080

Acknowledgments

I wish to express my thanks to Dr. Sadiq Rangwala for giving me the opportunity to work in his group, and also for his constant supervision and guidance of my thesis work. I gratefully acknowledge his support and contribution towards the completion of this work .

My sincere thanks to Prof. Krishna Rai Dastidar, Indian Association for the Cultivation of Science, Kolkata, for her active collaborations and fruitful discussions which helped in developing the molecular calculations.

I gratefully acknowledge Prof. A. R. Allouche, Universite de Lyon, France for providing the molecular data crucial for our calculations.

G Werth, Johannes Gutenberg University, Germany and Olivier Dulieu, Laboratoire Aime Cotton, France are acknowledged for useful discussions.

I thank Dr. Andal Narayanan and Dr. Pramod Pullarkat for their support and for conducting the annual review of my thesis work.

I gratefully thank Dr. E. Krishnakumar (TIFR) for providing us the technical support for high voltage switching.

I thank senior lab members Ravi, Arijit, Seunghyun, Tridib and Bhargav and the current lab members Rahul, Niranjan, Sourav, Rajarshi, Sreyas and Sagar for providing a nice working environment in the lab, and for sharing instruments and knowledge.

Special thanks to Tridib Ray for sharing experimental skills and knowledge, for useful discussions and for his help in the lab.

I thanks Nandan, Deepak , Jagdeesh, Surya, Raviranjan, Priya, Shafi, Asha, Harsha, Samim, Debashish, Rajib, Wasim, Meera and Sreeja for all sort of academic and non-academic discussions. Having them around was a nice and memorable experience.

I thank the director and the administrative department of RRI for facilitating the scientific environment. I acknowledge the technical support by N. Narayanaswamy and all the other members of the precision and general workshops. I sincerely thank Mrs. Sujatha and Shivi for crucial electronics fabrication.

I wish to thank Harini, Latha and Savitha for their help. Shiva and Manju are ac-

knowledged for all their support and hard work.

I sincerely thank all the Library staffs for providing a pleasant environment throughout my PhD work. My grateful thanks to all the staff of the institute including computer department, E and B department and canteen for their support.

Thanks to all my friends to make my time at RRI enjoyable.

Finally, I am deeply indebted to my family for their appreciation and tremendous support towards my thesis work.

Synopsis

Our ability to describe phenomena in nature is critically dependent on the detailed understanding of two and many particle interactions. Collisions, both elastic and inelestic are the experimental key for unlocking the details of interactions. The effort to understand elastic and inelastic collisions between atoms and ions at ultra-cold temperatures, specifically in the range 1000 K to 10^{-6} K, has led to the development of hybrid trap systems comprising either an ion trap and a Magneto Optical Trap (MOT) [1–5] or an ion trap and a degenerate quantum gas [6,7]. The state selection and long interrogation time provided by these traps, enable the pursuit of collisional studies at cold temperatures, where the collisions are dominated by the interaction potential. In such a system, energy can be exchanged between atoms and ions, opening possibilities for sympathetically cooling one species by the other [3–5]. Another advantage of hybrid traps is that it sets a platform for reactive interactions of atoms and molecules with ions to form complex molecules and molecular ions [8]. A key objective of our experiment is the association of atoms and ions, mediated by photons. In the above scenarios, the identification and detection of the product species and their stability in the presence of the trap fields (static or time varying electric and magnetic fields or light field) are extremely important.

In this thesis, we propose to demonstrate a novel hybrid experimental system, comprising an atom trap, ion trap, molecule trap, all built within a Fabry- Perot cavity. We employed a Magneto Optical Trap [9–12] to cool and trap the atomic species. Atom temperature of the order of few hundred μK can be realized in a MOT. A remarkable feature of the MOT is that the same magnetic field can be used for cooling and trapping multiple atomic species simultaneously. As the cold ion temperatures are orders of magnitude larger than the cold atom temperature, the collision energy is dominated by the velocity of ions. Hence to study ion-atom collisions for our present experiments, a MOT was deemed as opposed to degenerate gas of atoms, the execution of which is relatively complicated.

The ions can be trapped either by an oscillating radio frequency (rf) electric field

(Paul trap) or by a combination of static electric and magnetic fields (Penning trap) [13]. In a hybrid trap system, the performance of individual traps should not interfere by the fields used for the other. The Penning trap uses high magnetic fields and hence is not compatible with the MOT, due to non-linear Zeeman effect. Hence in our setup, we use Paul trap for ions, whose compatibility with MOT is studied in detail [14].

Like atoms, the studies on ultra-cold molecules is a rapidly progressing field. Laser cooling of molecules is challenging as the technique is limited to very particular electronic transitions in a small number of molecular species [15] with closed cycling transitions, which in molecules is hard to find. As the density of atoms in the MOT is of the order of $10^{10}/\text{cm}^3$, the formation of molecules due to three body collision is very unlikely. A widely used method for producing ultra-cold molecules (polar/non-polar) is photo-association, which is a light assisted association of a pair of colliding atoms. We employ this method for producing diatomic molecules in our experiment. In our setup, the polar/non-polar molecules can be trapped in a gradient electric field or in an optical dipole trap within the cavity mode respectively. Cold molecules are rich in applications in a vast area from precision clocks to quantum computation [16]. As the molecules can have electric and/or magnetic dipole moments and are spatially anisotropic, they are good candidates to load into optical lattice potentials and study a number of condensed matter systems [17].

An important goal in the experiment is the creation, trapping and detection of molecular ions produced from the cold atoms and study their stability in the hybrid trap. The combination of theoretical and experimental studies presented here prepare a solid foundation for future experiments with hybrid trap systems. The main objective of the work are

- to characterize individual traps in the hybrid apparatus.
- ensure reliable ion detection technique and reliable mass spectroscopy.
- set a basis for production of molecules and molecular ions.
- develop numerical codes to calculate transition rates and branching ratios in

molecular transitions.

- investigate the stability of complex species in the hybrid trap to study the possibilities for reactive molecular production and detection.

In order to create molecules in a specific internal state, it is essential to know their energy level structure and transition rates between allowed transitions. This is accomplished partly with resources from literature and partly by developing numerical codes and will be discussed in detail. All the work presented in this thesis is carried out with Rubidium (Rb) atoms and their derived ions and molecules (Rb^+, Rb_2 and Rb_2^+). The Rb_2^+ molecular ions are created by resonant enhanced multi photon ionization (REMPI) process using a pulsed dye laser, from Rb_2 molecules produced directly in the MOT. The ion trap is characterized for the optimal trapping of Rb_2^+ ions both experimentally as well as by numerical simulations. The ions are detected using a charged particle detector (channel electron multiplier, CEM) and the reliability of the mass spectrometry when a mixture of Rb^+ and Rb_2^+ ions are extracted together, is demonstrated. The stability of Rb_2^+ ions when held with the Rb MOT is studied in detail. It is observed that the Rb_2^+ ion numbers decay rapidly in the presence of trapping light field of the Rb MOT. The possible dissociative transitions in Rb_2^+ ions, mediated by the MOT trapping light field is discussed.

Experimental system: design and characterization.

The main challenge in developing the hybrid trap presented is in designing the electrode geometry to work as an ion trap or as a polar molecule trap and to incorporate a MOT and a Fabry-Perot cavity. Our final design [18–20], as shown in Fig. 1, comprises four thin tungsten wire loops wound over a quadrupole electrode structure, which can be used to trap ions in a linear or a spherical Paul trap or as a polar molecule trap by appropriate electrical configuration. Prior to assembling the apparatus, a detailed numerical simulation is performed to determine the stable operating parameters, ion motional resonances and an estimation of the trap depth and spatial extend. These numerical studies are carried out by explicitly solving the ion equation of motion, in the

time varying potential, and the results for both the spherical and linear ion traps are presented in detail. Proper care is taken to screen the ion trap centre from potentials applied for tuning the cavity length.

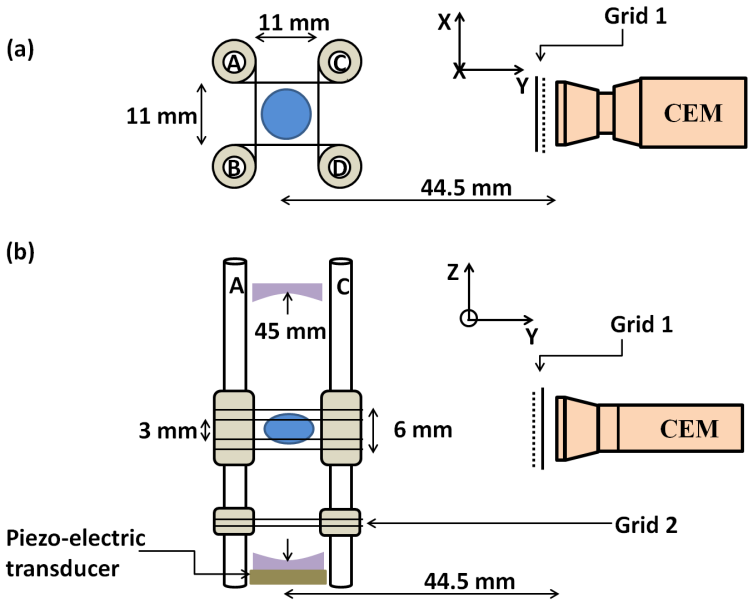

Figure 1: A schematic of the electrode geometry and the CEM is shown with dimensions. Panel (a) and (b) are the axial and top view respectively. The system can serve independently as, a spherical Paul trap: by an rf voltage on inner pair of wires; a linear Paul trap: by an rf voltage between diagonally opposite pair of rods; a polar molecule trap by a static high voltage on the wires to create a gradient electric field. The blue circle and ellipsoid in the trap centre represents the limiting spatial extend for a trapped ^{85}Rb ion with optimal trapping parameters in the spherical ion trap geometry. The trap centre is shielded from voltages applied on the CEM cone and the piezo electric transducer, using grounded grid pairs Grid 1 and Grid 2 respectively.

The trap centres are designed to coincide at the centre of the moderate finesse Fabry-Perot cavity. The addition of cavity serves to enhance interactions and allows frequency sensitive measurements in a mixture. Although single atom-cavity coupling is in the weak coupling regime, collective strong coupling of MOT atoms to cavity modes can be observed when the cavity is tuned to atomic resonance. We have used this atom-cavity collective strong coupling to estimate the MOT temperature by a time of flight method [18,21].

Another experimental prospects for the electrode structure also is described in the thesis. A relatively large electric field can be applied to trapped ensembles of atoms and molecules, which could then be probed by the cavity to make precision measurements on cold gases with tunable electric fields [22]. Moreover, polar molecules can be trapped in the apparatus by a straight forward implementation of a gradient field trap, as demonstrated by Kleinert et. al. [23]. The trap depth for various molecules which can be created in the experiment is presented.

Cold molecules: production and numerical methods

As the molecules possess rich internal energy level structure, in order to prepare them in a desired state and to study the interactions, it is essential to know the level structure accurately. We have developed codes to calculate the diatomic collision wave functions and to find the rates of transitions between ro-vibrational states in two electronic levels while using the electronic potential energy curves [24–26] and vibrational energy level calculation codes from literature [27]. The relevant energy level structure of Rb_2 and Rb_2^+ molecules involved in the experiment are presented in Fig. 2.

Photo-association (PA) of cold Rb atoms in the MOT to produce Rb_2 molecules is experimentally demonstrated and the spectra is compared with calculated excited state vibrational levels and the rates and branching ratios of transitions are calculated and presented. The Rb_2 molecules directly produced in the MOT by a photo-associative process mediated by the trapping laser (in the absence of a PA laser) is demonstrated and characterized.

Phase sensitive radial extraction and mass spectrometry of ions

As already mentioned, a hybrid trap is a platform to explore cold collisions. When atoms, ions and molecules are trapped together in the same spatial volume, the identification of resulting product ions are very important. Mass spectrometry is a conventional method for mass identification in a mixture. Because of constrains in the design of a hybrid apparatus, in particular the transverse extraction to the ion trap symmetry

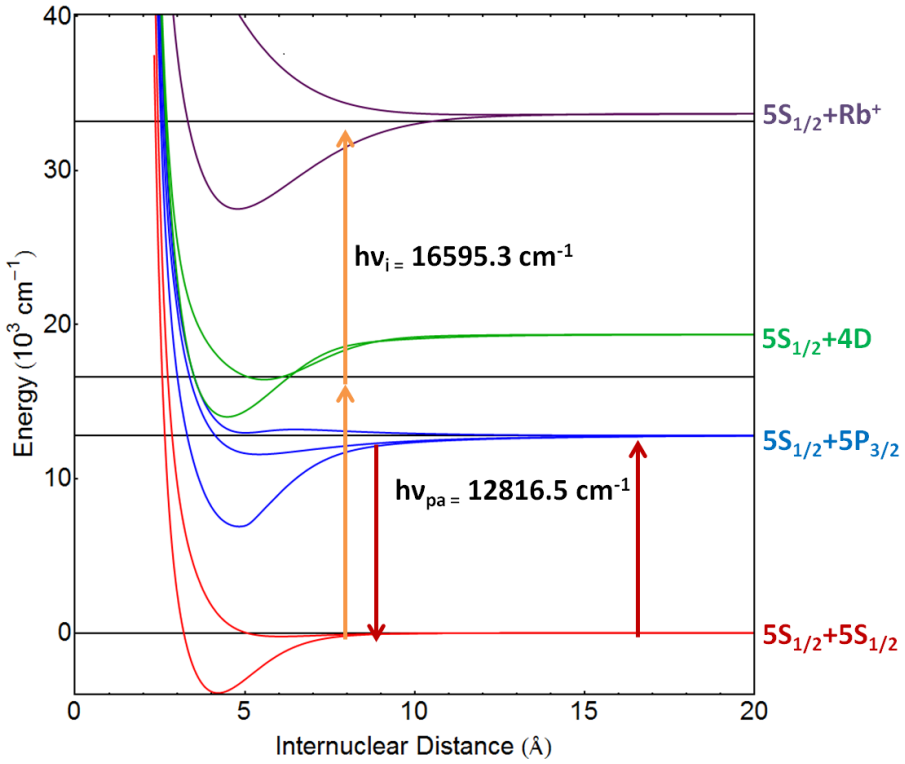

Figure 2: The potential energy curves of Rb_2 and Rb_2^+ molecules associated with the production of Rb_2^+ ground state molecular ions is shown in the figure. The asymptote corresponding to each PEC is marked. Rb_2 molecules are formed using 12816.546 cm^{-1} photons, (shown in red arrows) and are ionized using two photons of 16595.3cm^{-1} (shown in orange arrows) to form Rb_2^+ molecules.

axis, and the fact that, the maximum distance between the trap centre and the detector is limited to few cm, conventional mass spectroscopic techniques for mass resolution is not applicable. To demonstrate the mass spectrometry, both Rb^+ and Rb_2^+ ions are created simultaneously using the same laser source by different processes. The extracted ion signal is shown in Fig 3. Mass spectrometry in presence of rf field is studied at various rf phases using Rb^+ and Rb_2^+ ions [28]. The experimental results are in close agreement with the numerical simulation.

An ion extraction design quite different from the conventional method is studied numerically in detail and demonstrated in the experiment [28]. In the channel electron multiplier, the dead time of the detector ($\approx$ 8 nsec) leads to ion pile up and limit the ion detection. Hence an ion extraction method is devised with the trapping radio fre-

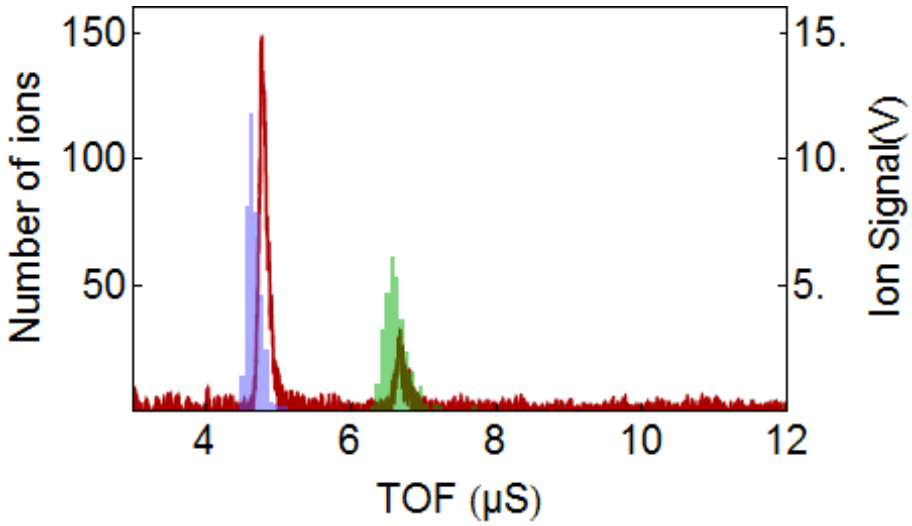

Figure 3: The figure shows the TOF signal of Rb^+ and Rb_2^+ ions extracted onto the channeltron. The Rb^+ and Rb_2^+ ions have mean time of flight of 4.7 μs and 6.7 μs respectively and are clearly resolved. The red curve is the experimental data which is the sum of 4000 data. The blue and green histograms are simulated TOF signal for Rb^+ and Rb_2^+ ions respectively. The left ordinate represents the ion number for the simulated histogram and the right ordinate represents the voltage corresponding to experimental signal.

quency (rf) field kept ON and precisely timing the extraction event with respect to rf field. This rf phase dependency of extraction efficiency of ions is studied in detail, both by experiment and by numerical simulation using Rb^+ ions. The temporal dispersion of different masses in the time of flight signal is explained by explicitly solving the ion equation of motion in the time dependent extraction electric field. The temporal dispersion in ion time of flight signal when extracted at specific rf phase is utilized to reduce the ion pile up issue in the detector.

Creation and stability of Rb_2^+ ions in the hybrid trap

The Rb_2^+ molecular ions are created from the directly formed Rb_2 molecules in the MOT by resonant enhanced multi photon ionization (REMPI) process using a pulsed dye laser. The ion trap is characterized for Rb_2^+ ions and the stability of Rb_2^+ ions when held with MOT is studied in detail. The Rb_2^+ decay rate from the ion trap is measured in three cases: (i) in the absence of atoms and MOT trapping light field, which shows

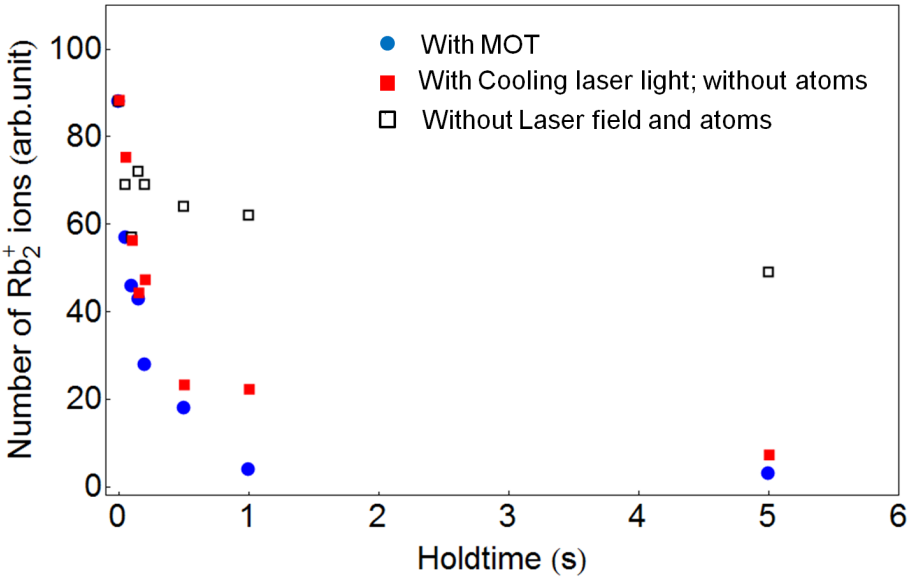

Figure 4: Figure shows the lifetime of Rb_2^+ ions in the ion trap with optimized parameters. The black open squares represents the lifetime in the absence of MOT atom and light fields. The blue circles represents the lifetime in the presence of MOT and the red squares shows the lifetime in the presence of cooling laser field without atoms. It is clear that the trapping light field is responsible for the short lifetime of Rb_2^+ ions.

that the Rb_2^+ ions can be held in the trap for 10s of seconds. (ii) when held with the MOT, ie., in the presence of atoms and light field, which resulted in a much faster decay, $\approx$ few hundreds of milliseconds, of Rb_2^+ ions from the trap. (iii) in this case the Rb_2^+ ions are held only in the presence of MOT cooling light field in the absence of atoms. The result clearly shows that the Rb_2^+ ions in the state distributions produced in the molecular ion formation process, are unstable in the presence of MOT cooling light field. The three cases for Rb_2^+ ion lifetime are shown in Fig. 4. Numerical simulations are performed to model the different possibilities of Rb_2^+ ion dissociation in presence of MOT light field.

Summary

In summary, a unique hybrid apparatus is presented in detail giving a characterization of individual traps. The creation of molecules from MOT atoms is demonstrated and the transitions rates are calculated using the numerical codes developed. The stability

of molecular ions is studied in the hybrid trap and possible ion dissociation channels are discussed. A radial ion extraction method is demonstrated and its dependency on trapping rf phase is studied in detail for single species as well as for mass spectroscopy. The experimental apparatus is built keeping options to work with Potassium, Cesium and Calcium in addition to Rb. This gives opportunity to study cold collisions ranging from $1/r$ to $1/r^6$. The numerical codes developed for ion trapping and molecular transitions are general and sets a basis to study all species in the system.

Contents

CHAPTER 1

Introduction

1.1 Overview

The understanding of the structure of matter and interactions on the atomic scale is at the heart of physics. Experimentally, various approaches are taken to investigate the details of interactions on the atomic and subatomic scales. A primary tool for such investigations were technologies developed to produce beams of atomic particles. Collision studies carried out by beam-target experiments or cross-beam experiments help to understand a variety of phenomena and mechanisms and to measure interaction cross sections [29–32].

The technique of confining atomic and molecular particles in a spatial volume for fundamental studies was introduced in 1950s. These developments are a consequence of the development and success of beam techniques. Here the particles are confined by interactions with electric and/or magnetic fields instead of constraining their motion by material walls. A remarkable feature of this technique is that it provides a stationary ensemble for repeated interrogation. Since the confining potentials are finite in their energy, and there are several mechanisms and imperfections that heat particles in traps, the cooling of the trapped particle goes together with the trapping in order to maintain the trapped ensemble. The advantage trapping provides is the ability to perform repeated measurements on the same particles and therefore also permit very accurate initial state preparation, both motional and internal, which allows interactions to be measured with high accuracy and precision.

Charged particles were the first to be confined in a spatial volume as confining them was easier than neutrals, since their motion could be easily controlled by electric and magnetic fields. Since for a static electric field, a potential minimum cannot be created in three dimensions [33], either a time varying electric quadrupole field (Paul trap) or a

combination of static electric and magnetic field (Penning trap) is used to dynamically confine the charged particle [13]. The ion trapping technique soon became a standard instrument to perform a variety of experiments. It enabled precise measurement of g factor of free electron [34], improving the precision of electron mass measurement [35] etc. As a mass spectrometer, quadrupole rf ion trap found applications in many areas [36]. In 1975, Hansch and Schawlow and independently Wineland and Dehmelt suggested the use of radiation pressure of laser light to cool atoms and ions. Ba^+ ions were the first laser cooled species by optical sideband cooling technique in 1978 [37]. The application of laser light to produce an ion cloud close to the trap centre with low energy, made remarkable improvement in precision measurements [38]. When cooled to a limit where the ion's kinetic energy is less than the mean Coulomb energy, the ions form an ordered crystalline structure [39, 40]. The combination of trapping and cooling ions paved the way for ion based frequency standards [41, 42], sensitive tests for quantum mechanics and QED and more recently quantum computation [43, 44]. The pioneers of ion trapping, Wolfgang Paul [45] and Hans Dehmelt [46] were awarded the Nobel prize in physics in 1989.

The first demonstration of laser cooling of neutral atoms was done by Chu et.al. in 1985 [9] using Sodium atoms. Two years later, Raab et.al. [10] demonstrated simultaneous cooling and trapping of Sodium atoms by means of an inhomogeneous magnetic field in conjunction with the laser light. The so called magneto optical trap (MOT) holds atoms with density $\sim 10^{10}/\mathrm{cm}^3$ in the μK temperature range. Further cooling of the atom cloud by evaporative techniques in a magnetic trap to reach quantum degeneracy led to the observation of Bose-Einstein condensed (BEC) state in a system of trapped, dilute atomic gas with an effective repulsive interaction [11, 12]. The MOT has become a standard technique for producing cold dilute ensemble of atoms and has been used for a variety of experiments for the study of fundamental interactions [47, 48], quantum computation [49], few and many body physics etc. [50]. For the development and understanding of laser cooling of atoms, a Nobel Prize was awarded to Steven Chu, Claude Cohen-Tannoudji and William Phillips in 1997 and for the con-

tributions in the field of BEC, Eric Cornell, Carl Wieman and Wolfgang Ketterle were awarded Nobel prize in 2001.

The interactions between cooled and trapped atoms are written in terms of scattering properties. As this thesis concerns the simultaneous cooling, trapping and manipulation of atoms, molecules and their ions, we carefully consider the nature of collisions between these. The collisions between atoms in the temperature range roughly from 1 mK to 1 μK are termed as cold collisions. A pair of ground state alkali atoms (S+S) interacts via electrostatic dispersion force with long range behaviour of potential being C_6/R^6 in nature. Whereas an alkali atom pair, one in the ground and the other in the excited state (S+P), interact via resonant dipole-dipole force with a long range C_3/R^3 potential. Two colliding ground state atoms, can get excited to a bound ro-vibrational level in the excited state potential by the absorption of a red-detuned photon, with respect to the S+P asymptote. This 2 particle +1 photon process is termed as photo association (PA) and is a very efficient technique to produce homo/hetero nuclear diatomic molecules [51–54]. As the molecules are formed from cold atoms, they are translationally cold. Apart from PA, there are several other techniques developed in the last few decades to produce and trap cold molecules. Buffer gas cooling [55], molecule filtering and trapping [56–58], cooling by decelerating the molecular beams by Stark, Zeeman or collisional deceleration [59–61] etc., have been demonstrated. The molecules slowed down using these techniques can be loaded to a magnetic trap for further cooling by evaporative methods [62]. Sisyphus cooling of electrically pre-trapped molecules has been shown recently [63], where a temperature of 30 mK has been demonstrated. Remarkably enough a MOT of SrF molecules [15] has been reported recently, but this is not a widely applicable method to produce a variety of ultra-cold molecules because of the in general lack of closed transitions in molecules due to the nuclear motion, that results in a large number of internal states. Studies with ultra cold molecules are rapidly increasing in numbers because they offer insights into low energy collision dynamics, precision measurements, quantum computation and open new lines of inquiry with dipolar gases [16, 64, 65].

Another very fruitful development was the development of atom-cavity physics. This system is the window to precision physics and QED measurements with atoms. Both atoms and molecules have been studied within an optical or microwave cavity. Atom cavity coupled system in weak coupling regime has been extensively used to investigate on optical bistability [66,67] and nonlinear processes [68]. Coupling cold atoms or ions into a cavity in strong coupling regime paved the way to the realization of many exciting results. Single photon generation from single atom or ion coupled to the cavity [69,70], collective strong coupling of cold atoms or coulomb crystal to cavity [18,71] are to name a few. The system is ideal to investigate quantum nonlinearity [72], cavity QED [73] and quantum computation [74]. Serge Haroche and David Wineland shared the Nobel prize in 2012 for their contribution towards the field of quantum manipulation and control, and in the experiments of Serge Haroche, cavities were integral to the method.

After the development of trapping atoms and ions individually, the mixed species interactions were studied in beam-target method, where a beam of one species was allowed to interact with the trapped species [75,76]. The idea of simultaneously trapping atoms and ions in the same spatial volume was introduced by W. W. Smith [1] in 2005. The hybrid trapping opened up a new platform for mixed species experiments. Hybrid traps comprising either trapped ions combined with a MOT [2–5, 19] or trapped ions in a quantum degenerate gas [6,7] have been developed in various labs to investigate specific interactions or chemical processes.

1.2 Motivation

Above, we have briefly covered the evolution of all the major threads that we shall utilize in our experiments at RRI. In our experimental apparatus, the possibility of simultaneous trapping of atoms, ions molecules and light exists so that a large variety of interactions can be studied in detail, with control over the numbers of trapped particles, their internal states and their motional states. So the primary motivation in our

Table 1.1: The interaction energy for different inter-species interaction is tabulated.

interacting particles	interaction energy
ion-ion	C_1/R
ion-dipole	C_2/R^2
dipole-dipole	C_3/R^3
ion-atom	C_4/R^4
atom-atom	C_6/R^6

experiments is to investigate the interactions between multiple species and if possible, incorporate the cavity as the primary tool for non-destructive detection of interactions. A mixed system of atoms, ions and molecules cooled and trapped in the same spatial volume enables the study of a variety of interactions as tabulated in Table 1.1.

The cold temperatures of the systems make it ideal to study non-kinetic energy driven interactions and to extract the effects due to the quantum nature of interactions. Moreover, trapping ensures measurements with long observation time. The optical cavity around the mixed species permits the enhancement or inhibition of specific interactions and allows for frequency sensitive measurements. Further, our hybrid trap system enables us to explore the details of accumulation of atoms and ions to form complex molecules and molecular ions.

1.3 The statement of the thesis problem

The simultaneous cooling and trapping of atoms and ions permits the study of photon assisted cold chemical reactions under "ab-initio" conditions. Several experiments around the world now exist where ab initio reactive processes can be systematically studied. In such experiments we can determine the reaction rate constants for specific states in the mK collision energy regime [8]. Zipkes et.al. [6] have demonstrated sym-

pathetic cooling of a single Yb^+ ion by a condensate of Rb atoms and determined their scattering cross section. In this experiment, each collision leads to loss of atoms from the BEC. Lee et.al. [77] have measured the collision rate coefficient between trapped Rb atoms in a MOT and the daughter Rb^+ ions in an ion trap. By combining a MOT as opposed to a degenerate gas with the ion trap, we can reach a steady state mixture of ions and atoms since the MOT can be continuously loaded.

An interesting feature of such experimental system is that we can replicate the processes in nature in a table top experiments. For example, from astrophysical observations to study the evolution of universe, the presence of H^+ (proton) and H_3^+ has been detected but the presence of H_2^+ has not been observed. Theoretical [78] and experimental [79, 80] studies suggest that the collision of H_2^+ and H_2 results to form $H_3^+ + H$. H_2^+ also undergoes direct photo dissociation in presence of electro-magnetic field [79,81]. The example of hydrogen suggests the complexity in modeling the details of a chain of interactions even with the simplest molecular ion. Several effects have to be considered as the molecule possesses a complex energy level structure. Thus it is essential to develop numerical codes to find the energy level structure which helps in state preparation and model various processes involving molecule light interactions.

A crucial point when mixtures are studied is the characterization of the production, trapping and detection of individual species. As in all the experiments leading up to the present day state of the art, our experiments rely heavily on theoretical and numerical work to design, analyze and interpret the experimental results. In our earlier experiments, we have seen that the ion-atom mixture $Rb^+ - Rb$ is stable in the presence of trapping field of each other [14]. Hence they can be co-trapped to study their collisional interactions and therefore sympathetically cool Rb^+ ions by collisions with the parent cold Rb atoms [4, 19]. Sympathetic cooling is a routinely used method now to cool species which cannot be laser cooled. Moreover, sympathetic cooling of Rb_2^+ ions with cold Rb atoms in the MOT gives more insight into their collisional properties. To accomplish this it is important to study the mutual stability of species in their respective traps. Keeping all these in mind, we perform few experiments to check the

stability of Rb_2^+ ions with the Rubidium MOT.
The key objectives of the thesis are enumerated as follows.

- To develop numerical codes for the characterization and interpretation of experimental results. These codes allow the understanding of ion traps and the detection process of the trapped ions.
- To device and demonstrate experimentally as well as by numerical simulations a detection scheme for the ions from the modified spherical ion trap.
- To demonstrate reliable mass spectroscopy in ion detection.
- To construct experimental arrangement for cold molecule and molecular ion production.
- To develop numerical codes for the calculation of molecular transition rates and branching ratios.
- To study the stability and co-existence of mixed species in the hybrid trap.
- To model the dissociation of molecular ions formed in specific internal state distribution.
- To numerically demonstrate the polar molecule trap in the hybrid apparatus.

1.4 Organization of the thesis

The structure of the thesis, chapter wise is given below.
The chapter 2 is formulated to describe the experimental apparatus with essential theoretical concepts based on which the system is developed. The concepts of cooling and trapping of neutral atoms, trapping charged particles, basics of Fabry-Perot cavity are briefly covered in the beginning. The details of the experimental apparatus, including the vacuum system, the role of Fabry- Perot cavity, MOT of ^{85}Rb atoms (laser system and detection setup) are then presented. The numerical simulations carried out for the

design and characterization of the ion trap and polar molecule trap are explained in detail.

In chapter 3, the transverse extraction of ions from the modified spherical ion trap is demonstrated in detail, both experimentally and using numerical simulations. The dependency of extraction efficiency on the phase of trapping rf field is explained. The condition for reliable mass resolution for Rb^+ and Rb_2^+ ions is presented. The experimental data are compared with numerical simulation, showing good agreement with each other.

The chapter 4 is dedicated to molecules. An introduction to molecules including the angular momentum coupling scheme, the electronic and vibrational energy levels and collisional wave functions, for the understanding of the rest of the thesis, is given in the beginning of the chapter. The potential energy curves involved in the production of Rb_2 and Rb_2^+ molecules are presented. The details of the numerical codes developed to find the transition rates are explained with the example of Rb_2 molecule. The experimental arrangement for PA to create Rb_2 molecule is discussed. The experimental signal of molecules created close to the dissociation limit is presented and the vibrational levels are identified. The numerical codes developed are used in modeling the results in chapter 5.

In chapter 5, the production of Rb_2^+ molecular ions by resonance-enhanced-multi-photon-ionization (REMPI) of Rb_2 molecule is discussed. The experimental sequence to study the stability of Rb_2^+ ions in the hybrid trap is given and the results of experiment are presented. The numerical modeling of possible channels of molecular ion interaction with the MOT trapping light field is explained.

The thesis concludes with a summary of the results and a discussion on the future prospects of the multi species experiments in the hybrid apparatus.

CHAPTER **2**

Experimental Concepts and the Hybrid Trap

In this chapter, we describe the background concepts for the experiment and the details of the hybrid trap. In section 2.1, a brief description of the theoretical concepts of cooling and trapping atoms, trapping charged particles and basics of Fabry-Perot cavity are given. In section 2.2, the experimental setup and the vacuum system are described. The details of the magneto optical trap for atoms is given in section 2.3. In section 2.4, a detailed description of the ion trap by electrically configuring the electrodes to operate as a linear quadrupole ion trap or as a spherical ion trap is then provided as it is crucial for the experiments in the present thesis. The possibility for trapping neutral polar molecules in the experimental system is discussed in section 2.5. Results of numerical simulations which serve to compliment and supplement are presented to explain the traps in detail.

2.1 Theoretical concepts

2.1.1 Cooling and trapping neutral atoms

Cooled and trapped atoms are required for a variety of studies and applications as they can be prepared in specific internal quantum states. In this section, we first see how to precisely set laser light to provide a velocity dependent force in order to slow down the velocity of the atoms (laser cooling). We then move on to the magneto optical trapping (MOT), where a magnetic field is used in conjunction with the optical field to provide a position dependent force and to define a trap centre.

Laser cooling: optical molasses

In laser cooling, the radiation force on the atom moving in the laser field is used to slow down the velocity of the atom. When an atom at rest absorbs a resonant photon of frequency ω_0 and wavevector $\vec{k}$, it gains momentum equivalent to $\hbar\vec{k}$. The subsequent spontaneous de-excitation of the atom results in the emission of a photon of wavevector $\vec{k'}$ oriented randomly with respect to $\vec{k}$ and the atom again gains a momentum $-\hbar\vec{k'}$. To understand the process of cooling, let us consider a simple case of a two level atom in one dimension and its interaction with light. For slowing down the velocity $\vec{v}$ of an atom, the atom should absorb a photon with wavevector opposite in direction to $\hat{v}$, $-\hat{k}$. A counter propagating pair of red detuned laser beam is used, such that an atom moving in either direction always sees the counter propagating laser beam Doppler shifted closer to resonance than the laser beam in the co-propagating direction with respect to the atom's velocity. As a result, the atom preferentially scatters the photons from the opposing beam and its velocity slows down in each absorption. The spontaneous isotropic emission results in a random walk and cancels out on average over many cycles. The force, $\vec{F_{\pm}}$ on the atom from photons of momentum $\pm\hbar\vec{k}$ is expressed as [82]

$$\vec{F}_{\pm} = \pm\frac{\hbar\vec{k}\Gamma}{2}\frac{\frac{I}{I_{sat}}}{1+\frac{I}{I_{sat}}+4\frac{(\delta\mp kv)^2}{\Gamma^2}} \tag{2.1}$$

where I is the laser light intensity, I_{sat} is the saturation intensity for the transition given by $I_{sat} = \pi hc\Gamma/3\lambda^3$, c is the velocity of light in free space, λ is the wavelength of the laser light, Γ is the natural linewidth of the excited state and δ is the detuning of the laser from the resonance. The net force $\vec{F}_{total}$ on the atom is

$$\vec{F}_{total} \cong \frac{8\hbar k^2\delta\frac{I}{I_{sat}}}{\Gamma(1+\frac{I}{I_{sat}}+4\frac{\delta^2}{\Gamma^2})^2}\vec{v} \equiv -\beta\vec{v} \tag{2.2}$$

For small atomic velocities, the force by the laser field is proportional to the atom velocity and results in viscous damping as illustrated in Fig. 2.1. Even if the average momentum gain in spontaneous emission cancels out over many cycles, the rms momentum gain is finite, which results in random walk in momentum space, giving a

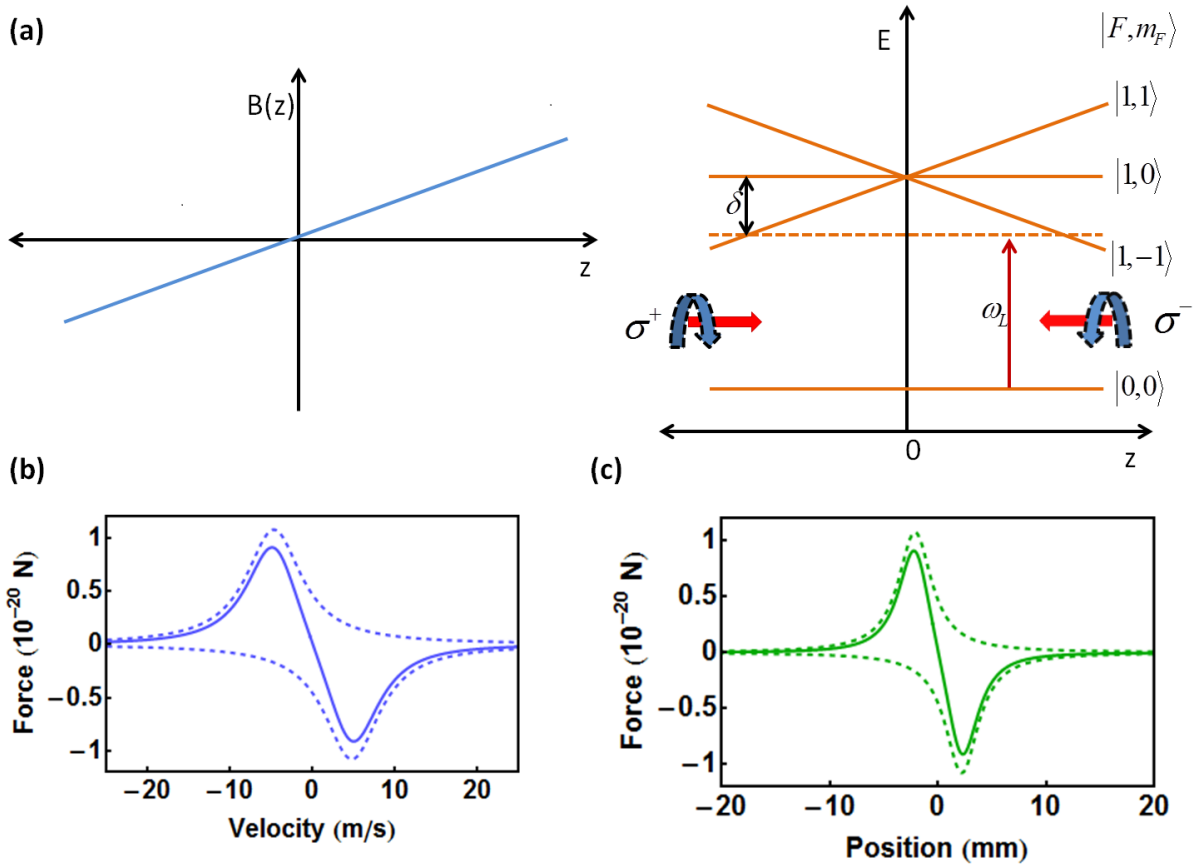

Figure 2.1: Panel (a) schematically represents the spatial variation of magnetic field, corresponding energy level splitting and light fields for the one dimensional laser cooling in a magneto-optical trap for a two level system with ground and excited state quantum number $F_g = 0$ and $F_e = 1$. In panel (b), the velocity dependence of the scattering force on a ^{85}Rb atom by a red detuned photon in an optical molasses setup is shown. The dotted curves represents the force due to each counter propagating beams and the solid curve represents the resultant force. In panel (c), the scattering force as a function of position in the MOT setup is shown for a ^{85}Rb atom. The counter-propagating red detuned $\sigma^{\pm}$ beams ensures that the atoms scatter photons preferentially from the counter-propagating beam which pushes the atoms towards the trap centre.

finite temperature $\hbar\Gamma/2k_B$ for the atom and is called the Doppler cooling limit.
The atomic motion can be cooled down in a three dimensional (3D) volume by applying 3 mutually orthogonal counter propagating beams intersecting in that volume. This technique, called optical molasses, can cool the atoms in the intersection of the 3 pairs of counter propagating beams but the atoms are not trapped as their diffusive motion can lead them out of the intersection region. Hence, for trapping, a position dependent force is required, which is explained below.

Magneto optical trap

The magneto optical trap uses a combination of magnetic and optical fields to cool and trap the atoms. The MOT uses an inhomogeneous magnetic field $\vec{B}(z) = B_0 z$, which can be produced by a pair of coils in anti-Helmholtz configuration. For simplicity, once again consider a two level atom with angular momentum of the ground state F_g=0 and the excited state F_e=1, moving in one dimension ($\hat{z}$). In a magnetic field of magnitude B_0, the atomic level degeneracy is lifted by $\Delta E_{|F,m_F\rangle} = \mu_B\ g_F\ m_F\ B_0$ due to Zeeman effect and the levels are labelled by the magnetic quantum number, $m_F = 0, \pm 1$. Here μ_B is the Bohr magneton and g_F is the Lande g factor. The dipole allowed transitions can occur from $0 \leftrightarrow 0, \pm 1$ by absorbing a π, $\sigma^{\pm}$ polarized photons respectively.
For positions $z > 0$, B_0 is positive and the energy of the state $m_F = +1$ is shifted up linearly with z and the state $m_F = -1$ is shifted down with respect to the unshifted level, $m_F = 0$, as shown in Fig.2.1(a). Hence an atom moving in $+\hat{z}$ direction, sees the red detuned light with wave vector $-\vec{k}$ as more resonant to the closest $m_F = -1$ level than with wavevector $\vec{k}$. Therefore the application of $\sigma^{\pm}$ polarized lights respectively in $\pm\vec{k}$ direction will cause the atoms to preferentially scatter the opposite beam. The reverse is true for an atom moving in the $-\hat{z}$ direction. This result in a position dependent force to drive the atoms towards the spatial centre. The force on the atom from the counter-propagating beams can be expressed as [82]

$$\vec{F}_{\pm} = \pm\frac{\hbar\vec{k}\Gamma}{2}\frac{\frac{I}{I_{sat}}}{1 + \frac{I}{I_{sat}} + 4\frac{(\delta \mp kv \pm \mu' \frac{dB}{dz} z/\hbar)^2}{\Gamma^2}} \tag{2.3}$$

where $\mu' \equiv (g_e M_e - g_g M_g)\mu_B$ is called the effective magnetic moment for the transition, where M_g and M_e are the magnetic quantum number of the ground and excited states. The net force is

$$\vec{F} = -\beta\vec{v} - \kappa\vec{r} \tag{2.4}$$

where $\kappa = \mu' B_0 \beta/\hbar k$ and β is defined in eq. 2.2. The position dependance of the force expressed in eq.2.3 is plotted in Fig.2.1(c). Thus in a MOT, the atoms are cooled and trapped simultaneously. For a variety of collision experiments envisaged in our apparatus, it is required to have different atomic species in the same spatial volume. The MOT has the important feature that the same magnetic field can be used for different atomic species with their corresponding resonant lasers to simultaneously trap the mixture.

2.1.2 Trapping charged particles

The motion of a charged particle can be controlled easily by electric and magnetic fields. However since an electrostatic potential minimum in three dimensions in free space is not achievable (Earnshaw's theorem [33]), either an oscillating electric field (Paul trap) or a combination of static electric and magnetic fields (Penning trap) is employed to trap the charged particle in a three dimensional volume.
In the Penning trap configuration, a dc electric field is applied between a ring and endcap electrodes to produce an axial potential minimum and a magnetic field $B = B_z\hat{z}$ is applied in the axial direction. The axial trapping is ensured by the electric field and radial trapping is ensured by the cyclotron motion produced by the crossed electric and magnetic fields. As large magnetic fields are required for the Penning trap, it is not suitable for a hybrid trap employing a MOT for atom trapping.

Paul trap

In an ideal Paul trap, a potential saddle is created between $\hat{r}$ (radial) and $\hat{z}$ (axial) directions which rotates at appropriate frequency to produce a three dimensional secular potential to trap the charged particle. In the original design, a voltage of the form

$V_{rf}Cos\Omega t$ is applied between a hyperbolic electrode and two endcap electrodes to produce a potential of the form

$$\phi(r,z,0) = \frac{\phi_0}{2d^2}(r^2 - 2z^2) \tag{2.5}$$

This is referred as a spherical Paul trap. However any electrode geometry which can produce a potential of the form in eq. 2.5 can be used as a Paul trap. In our experimental apparatus, a radio frequency(rf) voltage applied on a four wire electrode geometry is used to produce such a field. The details of the design and experimental demonstration of this modified spherical Paul trap can be found in [19,21].

The design of Paul trap electrodes have evolved and the most widely used design is a linear quadrupole electrode geometry with various forms of endcap electrodes. Here the trap potential takes the form $\phi(x,y,0) = \frac{\phi_0}{2d^2}(x^2 - y^2)$ in the radial direction and a parabolic static potential form in the axial direction. This is produced by applying an rf voltage $V_{rf}Cos\Omega t$ between the diagonally opposite electrodes in the quadrupole structure and a dc voltage on the endcap electrodes. This geometry has an advantage that the rf field is zero along the trap axis and hence multiple ions can be cooled and positioned at the field null of this rf potential. In our trap, the four wires constituting the spherical trap are wound over a quadrupole electrode geometry which are electrically isolated from each other. Hence by applying an rf voltage on the rods and a dc voltage on the wires, a linear quadrupole trap can also be achieved in the system. Both the traps, the modified spherical Paul trap and the linear quadrupole trap, are characterized in detail in section 2.4.1 and 2.4.2.

2.1.3 Fabry-Perot cavity

A Fabry-Perot cavity consists of two high reflectivity spherical or planar mirrors, facing each other and separated by a distance D. Let us consider a symmetric spherical mirror cavity (Fig. 2.2.a) with radius of curvature of the mirrors being R_M. The electric field distribution of an electromagnetic field within the cavity is determined by the boundary condition. The electromagnetic modes supported by the cavity can be

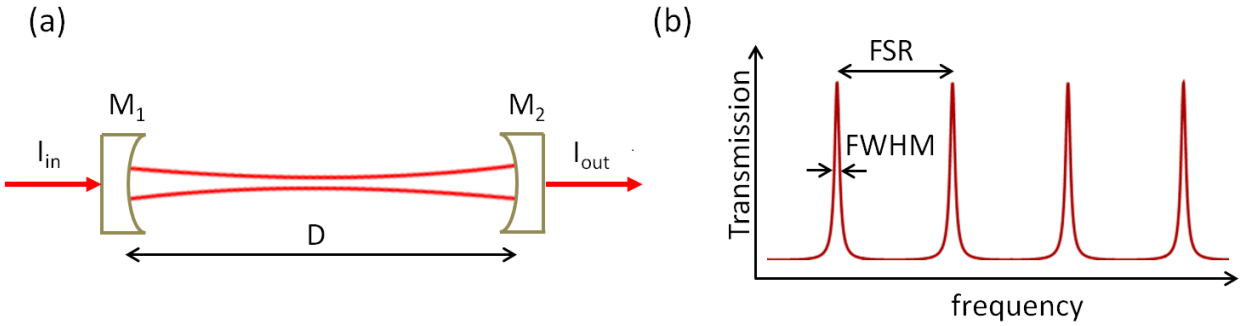

Figure 2.2: A Fabry-Perot cavity made of two spherical mirrors of identical radius of curvature is schematically represented in panel (a). The transmission profile of the cavity with a laser input scanning in frequency is shown in panel (b).

written as $TEM_{m,n,l}$, where m, n, and l are integers, with a transverse part (m, n) and a longitudinal part (l). The fundamental transverse mode, $TEM_{0,0,l}$, has a Gaussian field distribution in the transverse plane. The non zero l value represents the large number of longitudinal modes that are supported by the cavity, whose length $D >> \lambda$, the wavelength of the light fed into the cavity. The mode will sustain in the cavity provided the radius of curvature of the beam matches with that of the mirror at the boundaries and the frequency ν of the beam satisfy the resonance condition [83]

$$\nu = \frac{c}{2D}(l + \frac{1}{\pi}Cos^{-1}(1 - \frac{D}{R_M})) \tag{2.6}$$

Under this resonance condition, the electromagnetic wave forms a standing wave by back and forth reflections between the mirrors. Two adjacent resonant frequencies are separated by $c/2D$ and is called the free spectral range (FSR) of the cavity.

In real cavities loss of light originating from the finite reflectivity of the mirrors, scattering and absorption of light by the mirrors, etc., leads to broadening of the resonances. The transmitted intensity profile of the cavity, when seeded with a laser light scanning in frequency, has a finite width as shown in Fig. 2.2.b. Considering only the loss resulting from the finite reflectivity, r_M <1, the full width at half maximum (FWHM) of the transmitted light is given by

$$FWHM = FSR\frac{1 - r_M}{\pi\sqrt{r_M}} \tag{2.7}$$

The quantity $\pi\sqrt{r_M}/(1-r_M)$ is called the finesse ($\mathcal{F}$) of the cavity and $\mathcal{F}/2\pi$ corresponds to the number of round trips a photon takes before exiting the cavity [83]. The real measured linewidth depends on the total loss rate κ, which is the sum of all the losses. Hence from the measured linewidth, the true finesse of the cavity can be calculated as $\mathcal{F}$=FSR/FWHM.

2.2 Experimental setup

The experiment is designed for studying the inter-species interaction between alkali metal atoms, diatomic molecules and their derived atomic and molecular ions. In order to study the ion-atom interactions in steady state, hybrid traps, incorporating a MOT and a Paul trap as traps for atom and ion respectively, has been established in earlier work from our lab [14]. The system presented here has additional features like, a molecular trap for neutral polar molecules. All these traps are within the mode volume of the Fabry-Perot cavity which can be used to interrogate the trapped species and perform frequency sensitive measurements on the trapped systems with the longer term goal of measuring interactions between the trapped species. The experimental system consists of a vacuum system, laser systems and associated control electronics, photon and charged particle detectors and electronics for controlling the experimental sequence and instruments for measuring and recording the data. The experimental setup for MOT is discussed in section 2.3.1 and the ^{85}Rb MOT and detection schemes is discussed in section 2.3.2. The configuration and characteristics of the spherical and linear ion trap are discussed in detail in sections 2.4.1 and 2.4.2 respectively, and results of simulations are presented. Finally, in section 2.5, the possibility of the system to trap neutral polar molecule is presented with a discussion on the trap depth for various molecules which can be produced in the experimental system.

Vacuum system

The vacuum system consists of a compact stainless steel chamber, vacuum pumps and gauges all mounted on a vibration isolation optical table (Newport:RS4000). The required vacuum for the experiments is of the order of 10^{-10} mBar. The vacuum chamber is custom made from Kimball Physics (Kimball physics Inc: MCF600-SphHexadecagon-F2A16) with dimensions of 17.27 cm outer diameter and 3.5 cm height. The schematic diagram of the vacuum chamber, designed with 16 CF16 and 2 CF100 ports, is illustrated in Fig. 2.3. Out of 16 CF16 ports, 3 are used as electrical feedthrough, one is used for ion detector, Channel Electron Multiplier (CEM), one for connecting vacuum pumps and the others are viewports providing sufficient optical access, of which one throughport defines the cavity axis.

In order to ensure good ultra high vacuum, the flanges are tightened well using torque-wrench, with copper gaskets compressed between the CF knife edges of each flange connection. To achieve the ultra high vacuum, a diaphragm pump (Pfeiffer: MVP 015-2), a turbomolecular pump (Pfeiffer: TMU 071), a Titanium sublimation pump (Varian) and an ion pump (Varian:VacIon Plus 919-1210) are used in a specific sequence as described below. All the pumps are connected to the same port using a conical reducer nipple and a CF40 four way cross. An ion gauge (Varian:UHV-24) is attached to the same port as for the pumps to monitor the pressure inside the chamber.

At first, the diaphragm pump is used to reduce the pressure to 10^{-1} mBar. This vacuum is required for starting the turbomolecular pump. The turbomolecular pump is then used to create the initial vacuum of $\sim 10^{-8}$ mBar. There is a slow release of adsorbed gases, mostly water vapor, from the inner surface of the chamber, a phenomenon called outgassing which limits the achievable vacuum. The chamber is baked uniformly to a temperature 130 $^{\circ}C$ for one week in order to accelerate the outgassing rate, keeping the turbomolecular pump ON. This process helps to get a vacuum of 10^{-9} mBar after a few days of bake-out and cooling down the system. The next step in the pumping sequence is to operate the Ti: sublimation pump and start the ion pump. The pressure measured in the ion gauge goes under range (5×10^{-11} mBar) and the turbomolecular

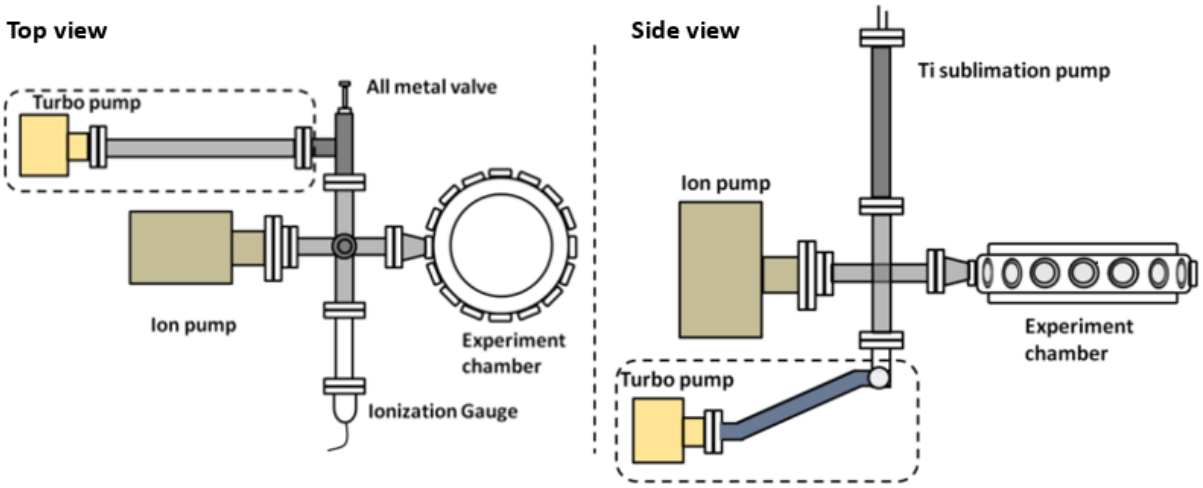

Figure 2.3: A schematic representation of top and side view of the experimental chamber is shown with the vacuum pumps used to achieve ultra high vacuum. The 5×10^{-11} mBar vacuum obtained is maintained by an ion pump.

pump is decoupled and that arm is sealed using an all metal seal valve. The ion pump is always operational to maintain the ultra high vacuum.

Fabry-Perot cavity

The Fabry-Perot cavity is made with two concave mirrors of 0.9997% reflectivity at 780 nm and radius of curvature 50 mm in a near-confocal configuration. The length of the cavity is 45.7 mm and can be scanned using a piezoelectric transducer (pzt) attached to one of the mirror. The initial linewidth of the cavity installed in the vacuum system is measured to be 1.4 ± 0.2 MHz giving a finesse of 2350. The cavity is probed with a home built external cavity diode laser which can be tuned to $5S_{1/2}$ to $5P_{3/2}$ transition. The transmitted light from the cavity is collected and is divided into two parts using a non-polarizing beam splitter. One part is used to image the cavity mode and the other part falls on a photomultiplier tube followed by a current preamplifier, both are calibrated. In Fig.2.7, the optical detection arrangement is schematically shown.

2.3 The atom trap

2.3.1 Magneto optical trap

Atom source

The experimental chamber contains dispensers (getters) as source of atoms. The dispensers are mounted inside the chamber and connected via feedthroughs and emits atomic vapour when current of few amperes pass through it. To ensure a constant rate of emission of atoms, the dispenser is operated using a constant current source. All the studies described in this thesis are carried out with Rubidium atoms and their derived ions and molecules (dispenser: SAES: Rb / NF / 4.8 / 17FT10+10). However, to enable inter species interaction studies, we have mounted dispensers of group 1 elements, Rubidium(^{85}Rb(72.2%, bosonic),^{87}Rb(27.8%, bosonic)), Potassium (^{40}K(8.4% enriched, fermionic), ^{39}K (bosonic)) and Cesium (^{133}Cs, bosonic) and one group II element, Calcium (^{40}Ca(99.9%)), of which the Ca^{+} ions are laser coolable and forms crystals at milli Kelvin temperatures.

Magnetic field coils

The magnetic field coils to produce the gradient magnetic field for the MOT are made of copper windings on a copper former and is mounted outside the vacuum chamber. The coils are mounted using brass plates of dimensions such that they just fit to the top and bottom CF100 viewports of the chamber. Each coil has 100 windings of 1.2 mm diameter copper wires. When passing current in anti-Helmholtz configuration, an inhomogeneous magnetic field, with zero at the centre and linearly increasing magnetic field in all directions results. In typical operating conditions, a current of 5A is used resulting in a magnetic field gradient of 22 Gauss/cm. As the current used are small, additional cooling method is not required.

2.3.2 MOT of ^{85}Rb atoms

Rubidium(Rb) belongs to group 1 elements in the periodic table of elements. For all the experiments reported in this thesis, we use the ^{85}Rb isotope. The important physical and chemical properties of ^{85}Rb are listed in Table. 2.1 [84]. The energy levels $5S_{\frac{1}{2}}$ and $5P_{\frac{3}{2}}$ and their hyperfine sublevels of ^{85}Rb atom are shown in Fig. 2.4. Out of the two available closed transitions, F=3 to F′=4 and F=2 to F′=1, we use the former one for cooling transition as it is a stronger transition. Although F′=4 to F=3 is the only dipole allowed decay channel, a small fraction of excited atoms decays to the F=2 ground state, a quadrupole allowed transition, which leads to loss of atoms from the cooling cycle in microseconds. Therefore, in order to maintain a steady state cloud of atoms, a low intensity repumping laser is used to transfer the atoms back to the F=3 state and hence to the cooling cycle. The repumper laser is locked to F=2 to F′=3 frequency. The details of the laser and optical setup for the MOT are explained below.

Laser system and frequency stabilization

We use external cavity diode lasers (ECDL) [85] as the cooling and repumping lasers. The ECDL consists of laser diode of the desired wavelength, temperature controller, a Littrow- configuration of a diffraction grating with piezoelectric transducer for wavelength tuning. For the cooling laser, we have developed the ECDL using Thorlabs: DL7140 laser diode and use the Toptica Photonics electronic module (DC110) for current and temperature control, controlling the voltage applied to the pzt and laser frequency stabilization. The frequency of the laser is monitored using a saturated absorption spectroscopy (SAS) in a Rb vapour cell. The laser is locked to a fixed wavelength using an active feedback to the laser when the wavelength shift. The SAS is used as the reference signal for laser locking. A schematic of the optical arrangement for the cooling and repumper laser is shown in Fig. 2.5 and 2.6. Briefly, a small part of the cooling laser beam is frequency shifted by $\sim$ 52 MHz using a combination of acousto-optic modulators (AOM). A SAS setup is made using the frequency shifted light beam. The

Table 2.1: The important properties of ^{85}Rb atom are tabulated and the values are taken from [84].

Atomic Number	37
Mass Number	85
Atomic mass	$1.409993199(70)\times10^{25}$ kg
Relative natural abundance	72.17%
Nuclear spin	5/2
Ionization limit	33690.7989 cm^{-1}
	(4.177eV)
$5S_{1/2} \longleftrightarrow 5P_{3/2}$ transition	
wavelength (vacuum)	780.241368 nm
Natural linewidth	$2\pi\times$ 6.0666 MHz
Saturation Intensity, I_{sat}(F = 3 $\rightarrow$ F′= 4)	3.89509(81) mW/cm^2
Lande g factor $g(5S_{1/2})$	2.00233113
$g(5P_{3/2})$	1.3362

laser is locked on the first cross over line of this shifted SAS signal using a proportional-integral-differential regulator (PID) and Pound-Drever-Hall (PDH) combination. The frequency of the unshifted part of the laser beam is thus $\approx$ 12 MHz red detuned to the F=3 to F′=4 transition and is injected to a tapered amplifier (BOOSTA) for amplifying the power. The cooling light can optionally switched using an AOM in the path.

We use a Toptica: DL100 commercial laser as the repumping laser along with a Toptica Photonics DC110 for laser control. A SAS setup is arranged for frequency monitoring and the laser is locked to F=2 to F′=3 line frequency. An AOM setup in the repumper path allows switching or modulation of the laser intensity.

In our setup, all lasers and the optics for the experiment are prepared on one optical table and the prepared light beams are transported to the experimental table using single mode polarization maintaining fibers (SMPMF). On the experimental table, the

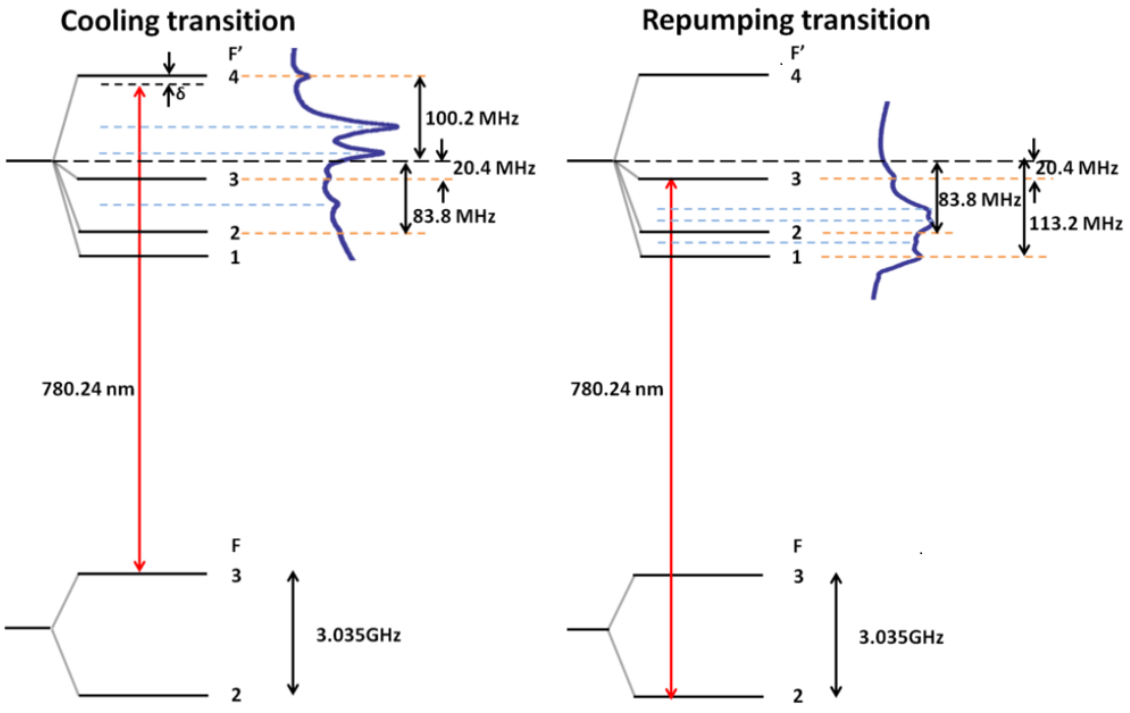

Figure 2.4: The schematic shows the energy levels of ^{85}Rb atom relevant for laser cooling scheme. The cooling and repumping transitions are marked and the SAS signals for transition from both the ground hyperfine levels are shown in inset.

cooling and repumper beams are mixed using a beam splitter, expanded to $\sim$ 8 mm using a telescope arrangement, divided into six beams and fed to the chamber with appropriate circular polarization for counter-propagating beams. The MOT is formed at the centre of the chamber, where the three pairs of beams and the magnetic field centre intersect.

Detection of the MOT atoms

Atom number and density:

The MOT atom number, spatial profile and density can be determined using the scattered fluorescence from the atom cloud. A spatial filtering setup is arranged which collects light through one of the viewport and filters out the scattered fluorescence from the atoms from the centre of the chamber while blocking all the scattered light from any part of the chamber. This means that the background light from the lasers is

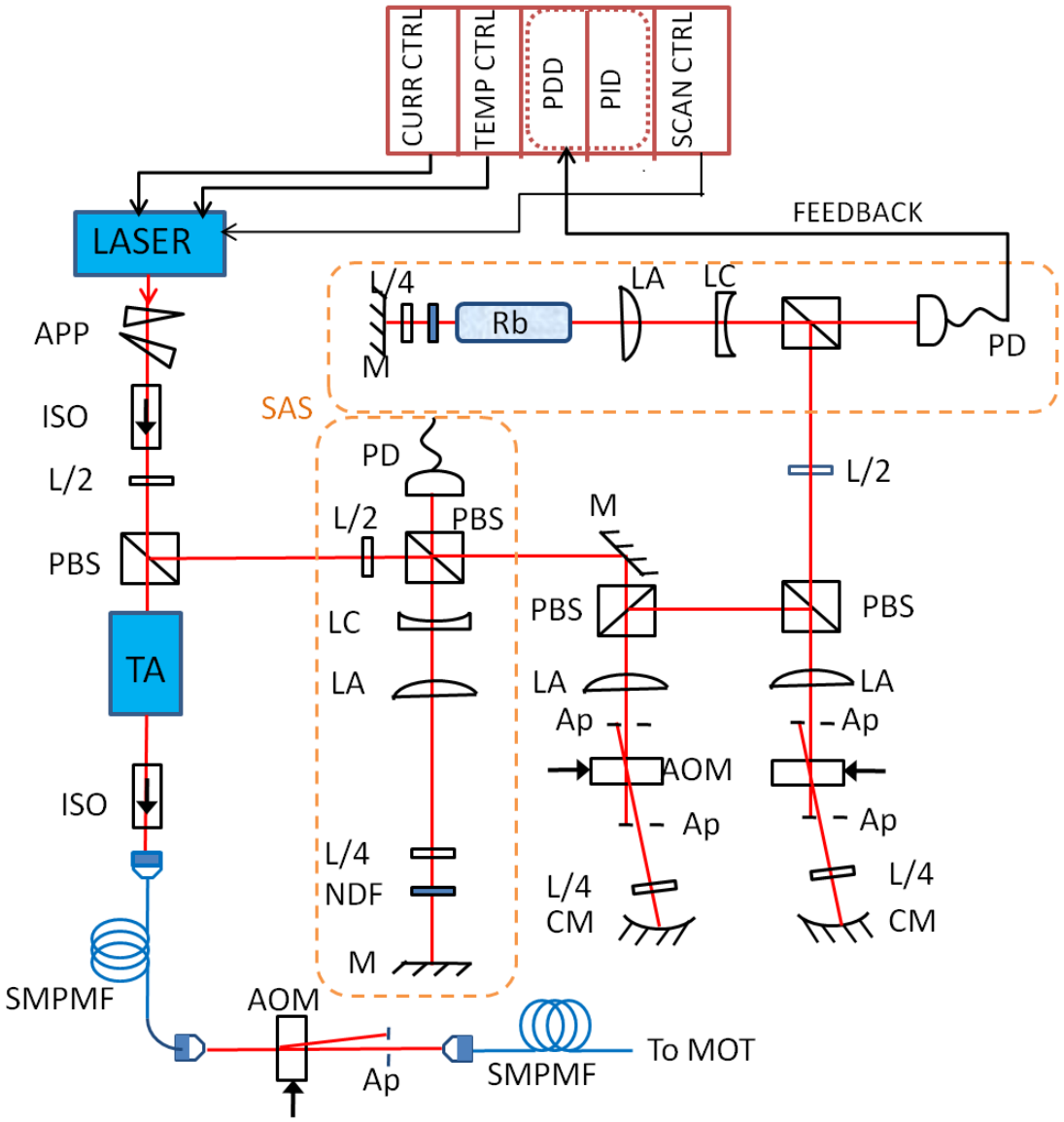

Figure 2.5: The optical arrangement for the cooling laser is schematically represented. The abbreviations used are as follows: AOM: acousto-optic modulator, APP: anamorphic prism pair, Ap: aperture, CM: concave mirror, ISO: optical isolator, LA: plano-convex lens, LC: plano-concave lens, L/2: half wave plate, L/4: quarter wave plate, M: plane mirror, NDF: neutral density filter, PBS: polarizing beam splitter, PD: photo diode, SMPMF: single mode polarization maintaining fiber and TA: tapered amplifier.

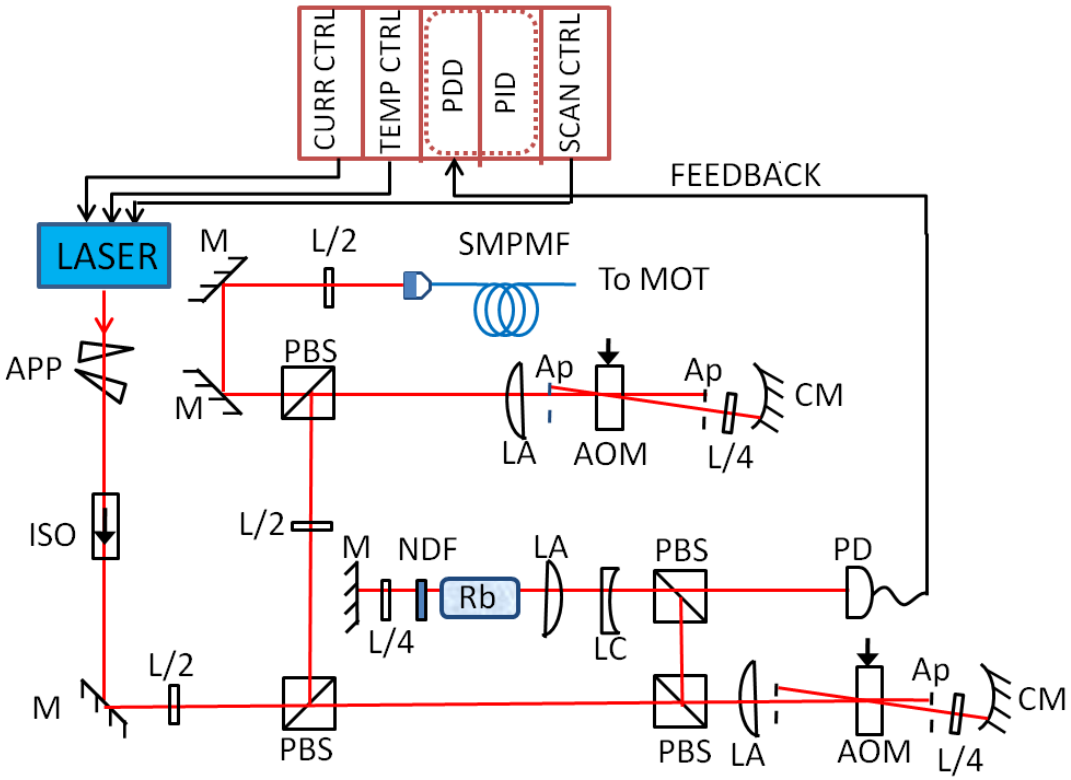

Figure 2.6: The optical arrangement for the repumper laser is schematically represented. The abbreviations used are same as in Fig. 2.5.

very efficiently suppressed while allowing the complete light emission from the atoms, in the solid angle to be detected. The setup is shown in the Fig. 2.7(a) and is made with a 2f-2f combination of plano-convex lenses with an aperture in between. The collected fluorescence is then divided into two parts using a non polarizing beam splitter, one part is fed to a CCD camera (Thorlabs: DCU224M) and the other part falls on a photo-multiplier tube (PMT)(Hamamatsu Photonics: R636-10).

The scattering rate of the photons by an atom is given by

$$R = (\frac{\Gamma}{2})\frac{\frac{I}{I_{sat}}}{1 + \frac{I}{I_{sat}} + 4\frac{\delta^2}{\Gamma^2}} \tag{2.8}$$

Where Γ is the natural linewidth of the transition, δ is the detuning of the light from the resonance, I is the laser light intensity and I_{sat} is the saturation intensity of the transition. The PMT output is a small current signal proportional to the incident light and is amplified using a preamplifier (Hamamatsu Photonics: C7319) and the combination

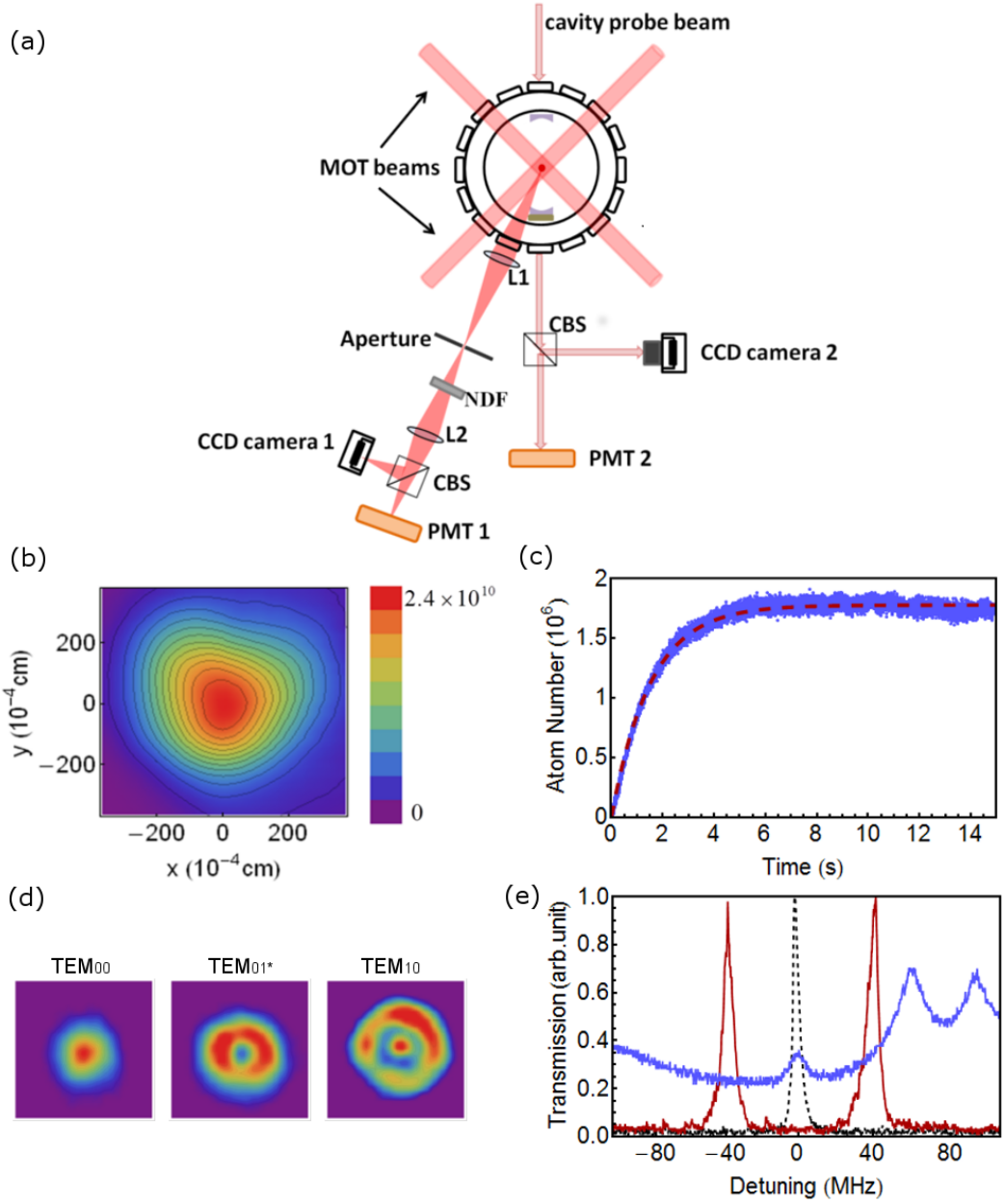

Figure 2.7: Panel (a) illustrates the optical detection schemes. A spatial filtering arrangement is made in free space to eliminate the background scattered light. The CCD cameras are used to image the spatial profiles and PMTs are used to measure the light levels. In panel (b), the CCD image of the spatial profile of the MOT in a plane perpendicular to the detection axis is shown. The loading of the MOT measured on the PMT is shown in panel (c). The light coupled from the MOT atoms into TEM_{00},TEM_{01^*} and TEM_{10} modes of the cavity, imaged on the CCD is shown in panel (d). An experimental data illustrating the vacuum Rabi split, as a result of collective strong coupling of MOT atoms to a cavity mode is shown in panel (e).

is calibrated with a light source of known power. Hence from the output signal, the power of scattered light in the solid angle considered is known and the total fluorescence in 4π direction is calculated. Knowing the rate at which a single atom scatters light (eq. 2.8) and the total power of the emitted light of known wavelength, the atom number for non-interacting atoms can be calculated. The code in Appendix B gives the details of the optical signal to atom number conversion.

The spatial profile of the MOT which is approximately spherically symmetric, is obtained in one plane from the CCD camera image. Knowing the total atom number and the FWHM of the distribution, the density of atoms in the MOT is estimated to be 2.4×10^{10} cm^{-3}. The MOT spatial profile is shown in the Fig. 2.7(b) and the MOT loading from Rubidium vapour is shown in Fig. 2.7(c).

MOT temperature determination:

As mentioned earlier, the MOT is formed at the centre of the Fabry-Perot cavity. The atoms within any cavity mode volume collectively couple to that mode and can be detected using the CCD-PMT detection arrangement in the cavity output (Fig.2.7(a)). The scattered light from the MOT atoms coupled to the TEM_{00},TEM_{01^*} and TEM_{10} modes is shown in the Fig. 2.7(d).

In our setup, as the finesse of the cavity is moderate, the coupling of a single atom to the cavity is in the weak coupling regime, i.e., $\gamma > g_0 > \kappa$, where g_0 is the atom-cavity coupling constant, γ is the atom's spontaneous emission decay rate in free space and κ is the empty cavity photon decay rate. However, when N_c number of atoms collectively couple to a cavity mode, the coupling constant $g = g_0\sqrt{N_c}$ can be greater than γ and κ. In this collective strong coupling limit, the degeneracy between the atomic and photonic dressed state is lifted to give resonances at $\pm g_0\sqrt{N_c}$ which is known as vacuum Rabi splitting (VRS). We have used this strong atom-cavity coupling to estimate the MOT temperature [18]. Details of this measurement are in the thesis of Tridib Ray [18, 21]. For completeness, we briefly describe the temperature measurement.

The temperature of MOT atoms is estimated by a time of flight method, using the col-

lective strong coupling of the atoms to the Fabry-Perot cavity. In Fig. 2.7(e) the vacuum Rabi split is demonstrated. Here, the cavity is tuned to the Rubidium $F = 3$ to $F' = 4$ transition and is probed using a laser scanning through $F = 3$ to the excited state hyperfine levels. The blue line in the figure shows the SAS signal used for the frequency reference of the probe laser. When the atoms are absent in the cavity mode volume, a Lorentzian output as shown by the black dotted line results. The collective coupling of a large number of atoms to the cavity mode results in splitting the energy levels and is shown by the red thick line in the figure.

In the first step, the VRS is measured for known atom numbers in the TEM_{00} cavity mode, and fitted with equation $VRS = 2g_0\sqrt{N_c}$ to deduce the atom-cavity coupling constant g_0. Using the value of g_0 (130$\pm$3.9 kHz, measured for $F = 3$ to $F' = 4$ transition), the number of atoms in the cavity mode can be determined for a measured VRS. To estimate the temperature, the cooling and the repumper lasers are sequentially switched off to prepare the atoms in $F = 3$ ground state and the ballistically expanding cloud is probed through the cavity using a laser scanning through $F = 3$ to the excited state hyperfine levels. Keeping the cavity resonant with $F = 3$ to $F' = 4$ transition, the VRS is measured as a function of time. This provides the expansion rate of the atom number N_c, and the initial temperature of the atoms is estimated to be $107.7 \pm 7.5\ \mu K$.

2.4 The ion trap

In a hybrid apparatus, the fields used for the traps should not interfere the performance of each other. The mutual compatibility of ion trap (Paul trap) and a MOT is already studied in our lab [14, 86]. The challenge was in designing the geometry of an ion trap to incorporate a MOT and a Fabry-Perot cavity. Our final design of the hybrid apparatus can be used to trap ions in a linear or a modified spherical Paul trap. Moreover, the electrodes for the spherical trap can be biased appropriately to trap polar molecules, which will be explained in section 2.5. Another difference of the design of the hybrid geometry from the conventional way is regarding the ion extraction. The highest sym-

metry axis of the ion traps share the cavity axis and hence the ion extraction from the trap for detection has to be transverse to the axis of the ion trap.

Electrode geometry

The trap consists of four Tungsten wire loops wound in square geometry as illustrated in Fig. 2.8. The wires are wound over the groves on the ceramic sleeves jacketing four stainless steel (SS316) rods. The ceramic sleeves electrically isolates each wire loop and the rods and hence all the electrodes can be biased independently. The rods and the hollow ceramic sleeves are 3 mm and 6 mm in diameter respectively. The rods are assembled in a quadrupole geometry with a center to center distance of 17 mm. The Tungsten wires are 80 μm in diameter, and are wound with a separation of 1.5 mm, 3 mm and 1.5 mm, respectively. The trapped ions can be detected destructively using a charged particle detector or non-destructively by fluorescence. Except for Calcium, the ions of other elements in the apparatus do not have a transition accessible for optical detection. We use a channel electron multiplier (Dr. Sjuts KBL10RS) for the detection of the trapped ions. As mentioned earlier, it is mounted transverse to the symmetry axis, 44.5 mm from the trap centre. For the proper functioning of the trap, the trap volume should be screened from the voltages applied on all other electrodes in the chamber. For example, the CEM is always maintained at a high voltage (HV) of -2.4 kV and depending on the experiment, voltage up to 100 V is applied on the pzt for cavity tuning. A set of two shielding electrodes (Grid 1 and Grid 2) are used to shield the trap centre from voltages applied on the CEM cone and the pzt respectively. They are maintained at ground potential while the trap is operational and switched to appropriate voltages for ion extraction.

Extensive simulation has been performed prior to the assembly, to characterize the trapping and ion extraction and to design shielding electrodes. A software package SIMION 8.0 [87] is used to generate the electrode geometry in three dimensions and to numerically solve the Laplace equation with electrodes at a given voltage, to get the potential $\phi(x, y, z)$ in the spatial volume considered. Fig. 2.9 shows the SIMION gen-

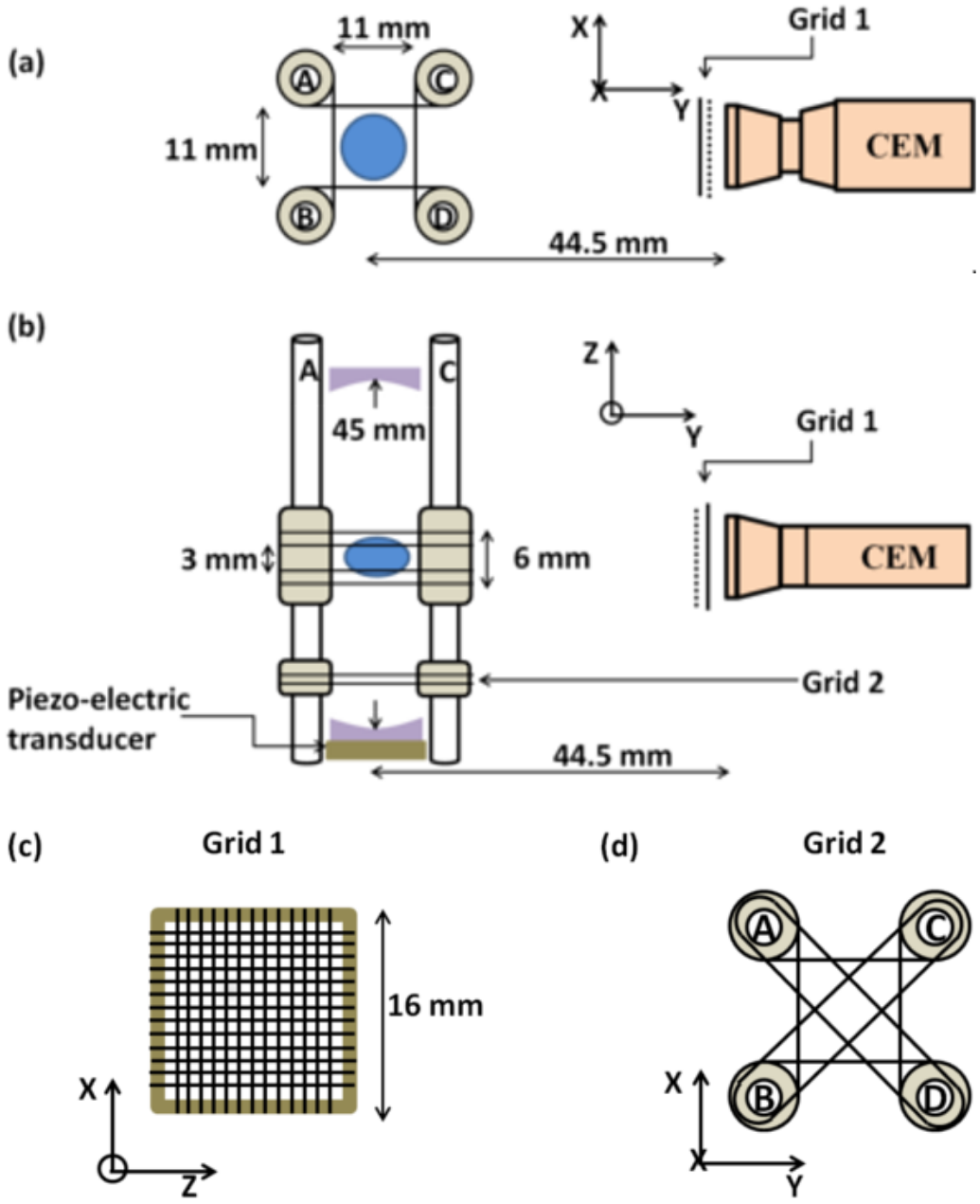

Figure 2.8: A schematic of the ion trap electrode geometry and the CEM is shown with dimensions roughly on scale. Panel (a) and (b) are the axial and top view respectively. The blue sphere and ellipsoid in the trap centre represents the limiting spatial extent for a trapped ^{85}Rb ion with optimal trapping parameters as mentioned in the text. The trap centre is shielded from voltages applied on the CEM cone and the pzt, using grounded grid pairs Grid 1 and Grid 2 respectively. The grids 1 and 2 along their respective axis are shown in panel (c) and (d) respectively.

erated electrode geometry of the whole chamber and the code developed to generate the electrode geometry is given in Appendix A. The trajectory of the ion in the trap can be simulated in two ways: (i) using the SIMION software itself or (ii) by importing the SIMION generated potential to Mathematica and solving for the equation of motion. In the second method, the potential due to each electrode set to 1 V while all the other electrodes at ground potential is solved separately in SIMION and multiplied with desired voltages and superposed in Mathematica. The trajectory of the ion in the trap is then examined to check for ion stability in the trap with the parameters used. All the simulation results presented in this chapter are performed in this method for single $^{85}Rb^{+}$ ions, while the first method is used to explain few experimental results and is presented in chapter 3.

In the following two subsections we describe the biasing of the electrodes to work as a spherical and linear ion trap, stable operating parameters, ion motional resonances and an estimation of the ion trap depth and spatial extent.

2.4.1 The modified spherical Paul trap

The secular potential for the ion trap is produced by applying a radio frequency voltage of appropriate amplitude and frequency on the inner pair of wires. The outer pair of wires can be biased with (i) an equal voltage on both to change the trap depth in the radial and axial directions [19] or (ii) with a slightly unequal voltage to shift the ion trap centre to increase the spatial overlap with the MOT atoms. Fig. 2.10 shows the biasing of the ion trap electrodes and the resulting potentials in XY and XZ planes.

For an ideal spherical Paul trap with hyperbolic electrodes, when a voltage $U_{dc} + V_{rf}Cos\Omega t$ is applied between the ring and the endcap electrode, the resulting potential has the form

$$\phi(x, y, t) = \frac{2z^2 - x^2 - y^2}{2d^2}(U_{dc} + V_{rf}Cos\Omega t) \tag{2.9}$$

with $d = \sqrt{\frac{r_0^2}{2} + z_0^2}$ where r_0 and z_0 are the distance of the ring and the endcap electrodes from the trap centre respectively. For an ion with mass M and charge Q, the ion

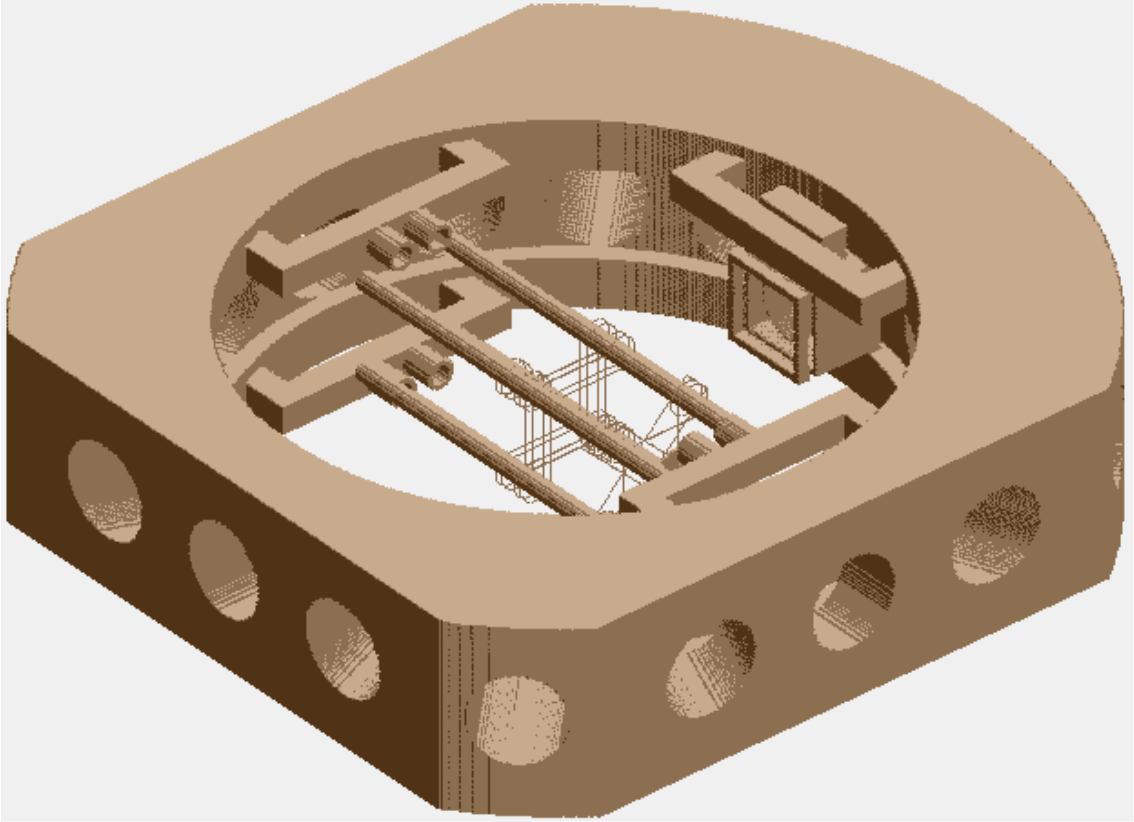

Figure 2.9: Figure shows the the SIMION generated electrode geometry including the vacuum chamber. The CEM, mounted transverse to the ion trap axis, is housed in a grounded metal structure with a grid in front to shield the ion trap centre from high voltage on the CEM. The various electrodes are identified in Fig. 2.8.

trajectory in this field is governed by the equations of motion:

$$\begin{aligned} \ddot{x} &= \frac{Q}{Md^2}(U_{dc} + V_{rf}Cos\Omega t)x \\ \ddot{y} &= \frac{Q}{Md^2}(U_{dc} + V_{rf}Cos\Omega t)y \\ \ddot{z} &= \frac{-Q}{Md^2}(U_{dc} + V_{rf}Cos\Omega t)z \end{aligned} \tag{2.10}$$

This set of equation can be expressed in a general form of Mathieu equations using the following parametrization.

$$\begin{aligned} a_x = a_y = -\frac{-4QU_{dc}}{M\Omega^2 d^2} \quad ; \quad q_x = q_y = \frac{2QV_{rf}}{M\Omega^2 d^2} \\ a_z = -\frac{8QU_{dc}}{M\Omega^2 d^2} \quad ; \quad q_z = \frac{-4QV_{rf}}{M\Omega^2 d^2} \quad ; \quad \tau = \frac{\Omega t}{2} \end{aligned} \tag{2.11}$$

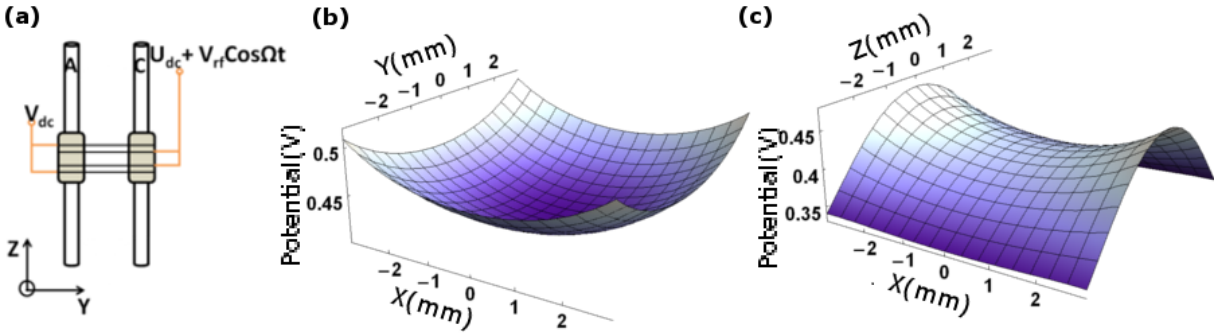

Figure 2.10: Panel (a) shows the biasing of the wire electrodes to obtain a spherical ion trap potential in the trap centre. The resulting potentials in the XY and XZ planes are shown in panels (b) and (c) respectively.

and the equation of motion takes the form

$$\frac{\partial^2 u_i}{\partial \tau^2} + (a_i - 2q_i Cos2\tau)u_i = 0 \quad , \quad \text{i=1, 2, 3} \tag{2.12}$$

The Mathieu equation has non-diverging solutions for a combination of a and q parameters, which are referred as the stability regions. The first stability region for an ideal spherical Paul trap is shown in Fig. 2.11(a). For a fixed rf frequency, a and q defines the U_{dc} and V_{rf} voltages for which an ion of charge to mass ratio Q/M is stable. For a range of U_{dc} and V_{rf} voltages at 500 kHz, the ion trajectory in the spherical trap is calculated and the stable points are plotted in the $a - q$ parameter space as shown in Fig. 2.11(b). Here, the a and q are calculated using eq. 2.11 with the value of d found from a quadratic fit of the secular potential. The numerical code to solve the equation of motion and to generate the a-q stability diagram is given in Appendix B. The stable operating voltages for other species mounted in the chamber are also calculated. Fig. 2.12 shows the region of stability as a function of applied voltages for K^+, Ca^+, Rb^+ and Cs^+ ions at rf frequency 500 kHz.

The modified spherical ion trap has been experimentally characterized for its trapping [19] and the transverse extraction for ion detection [28] using $^{85}Rb^+$ ions. The details of the experimental trap optimization is presented in [19] and the thesis of Tridib Ray [21] and briefly discussed in chapter 3 for completeness, as the experiments are performed with the optimized parameters. In the following simulations, we use the

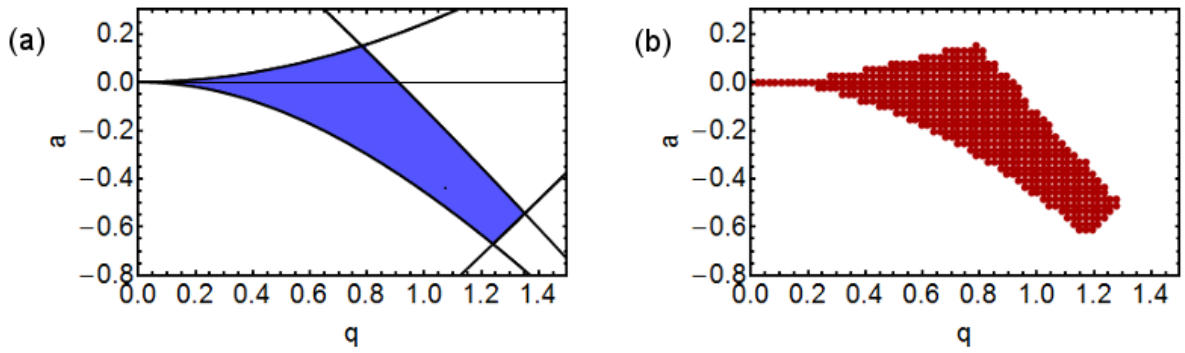

Figure 2.11: The panel (a) shows the first stability region, which is the solution of eq. 2.12, for an ideal spherical Paul trap. For a fixed ion mass and rf frequency, the parameters a and q are linear functions of trapping voltages U_{dc} and V_{rf} respectively. The panel (b) shows the stability region for the modified spherical Paul trap. The experimentally optimized voltage, $V_{rf} = 80$ V corresponds to $q = 0.34$.

experimentally optimized voltages, $U_{dc} = 0$ and $V_{rf} = 80$ V at 500 kHz which corresponds to $(a, q) = (0, 0.34)$.

Trap frequency:

Consider the adiabatic condition, where the variation in the amplitude of the high frequency rf field is approximately constant over the ion's oscillation amplitude. When averaged over the rf field oscillation, the ion's motion is governed by the effective potential $U_{eff} = Q^2 E_\Omega^2 / 4M\Omega^2$, where E_Ω is the amplitude of the rf electric field. Hence the ions trajectory can be decomposed into two: (i) the micromotion which is the small amplitude oscillation induced by the rf field and (ii) the macromotion (secular motion), which is the slow oscillatory motion in the effective potential, both are shown in Fig. 2.13.

The secular motion frequency can be determined experimentally by resonant excitation method. Here, a small amplitude rf voltage $V_{exc} Cos 2\pi f t$ is added to the trapping rf voltage and is scanned over a range of frequencies in the sub-MHz range. When this excitation frequency matches with the secular frequency or its harmonics and subharmonics, the ions are resonantly excited and lost from the trap [13]. The trap fre-

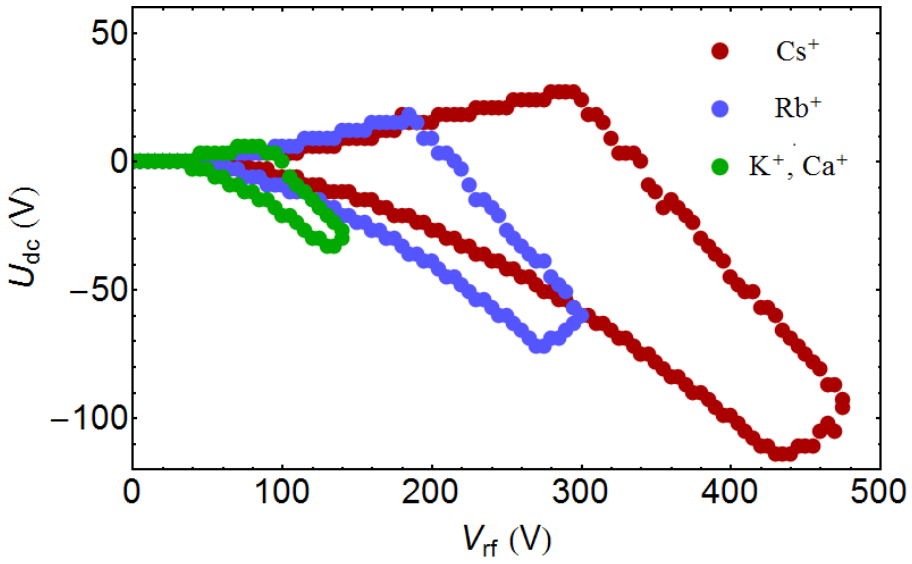

Figure 2.12: The figure shows the region of stability as a function of applied voltages for the Cs^+, Rb^+, K^+ and Ca^+ ions at rf frequency 500 kHz.

quency depends on mass and is directly proportional to the rf trapping voltage. The importance of determining the secular frequency is that specific ion species can be selectively removed from a mixture of different species of ions in the trap.

The secular frequency, $f_{r,z}$ can be numerically estimated by two methods. One method is to Fourier transform the ion trajectories [21]. The Fourier spectrum contains peaks at the micromotion frequency (applied rf frequency, ν_{rf}= 500 kHz in our experiments), at the macromotion frequencies $f_{r,z}$ and at sidebands to the micromotion frequency, $\nu_{rf} \pm f_{r,z}$. The values of f_r=45 kHz and f_z=59 kHz are in reasonable agreement with the experimentally measured frequencies f_r=43 kHz and f_z=54 kHz. The second method is similar to the experimental method. Here, a weak rf voltage $V_{exc}Cos2\pi ft$ is added to the trapping rf voltage and the ion equation of motion is solved in the resulting potential. The resonances are found by evolving the ion in the trap for a range of excitation frequencies. When f matches with the motional frequency, the ion escapes from the trap and the time of escape is found from its trajectory. In this method, unlike the Fourier transform method, the different harmonics and sub-harmonics are also observable and the spectra of Rb^+ ions at V_{rf} =80 V is shown in Fig 2.14. The numerical code for resonant excitation method is given in Appendix B. If V_{exc} or the duration

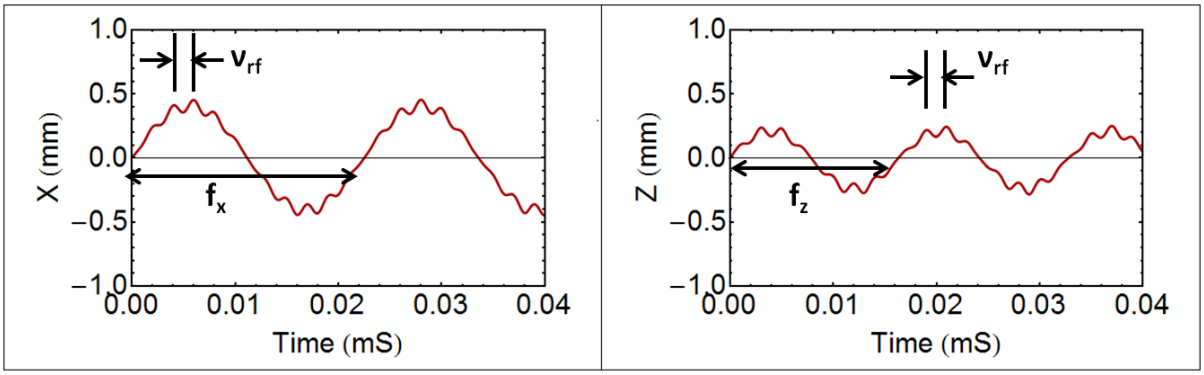

Figure 2.13: Figure shows the the micro and macro frequencies in the Rb^+ ion trajectory in $\hat{x}$ and $\hat{z}$ directions in the modified spherical ion trap operated at the optimized parameters.

of excitation is large, the resonance looks broadened in the spectrum. Since twice the resonance frequency (second harmonic) is the strongest resonance, in the simulation to generate the spectrum in Fig.2.14, a lower excitation voltage is used from 60 kHz to 150 kHz to get a narrow peak at second harmonic frequencies. Similarly, to get the sub-harmonics, a higher excitation voltage is used in the range 100 Hz to 30 kHz. The resulting secular frequencies f_r= 40 kHz and f_z= 55 kHz is in reasonable agreement with the experimentally observed resonances.

Trap extent and depth:

For an ion atom collision experiment in hybrid trap with overlapping trap volumes, the spatial extent of the traps play an important role in the interaction [4]. Therefore it is required to estimate the extent of the ion trap, i.e, the maximum displacement that an ion can have from the trap centre but still be trapped. This estimation is done in $\hat{x}$, $\hat{y}$ and $\hat{z}$ directions for the optimized trapping parameters. To find the extent in $\hat{x}$ direction, a zero velocity ion is evolved in the trap for 500 cycles with different initial positions from (-5 mm, 0, 0) to (+5 mm, 0, 0). For each case, the trajectory is examined to determine the ejection time if the ion is not trapped and the result is shown in Fig 2.15. The same procedure is repeated in $\hat{y}$ and $\hat{z}$ directions. The trap extent is found to be 4.2 mm and 3 mm respectively in the radial and axial direction for the Rb^+ ion.

The trap depth determines the maximum velocity an ion at centre can have, but still

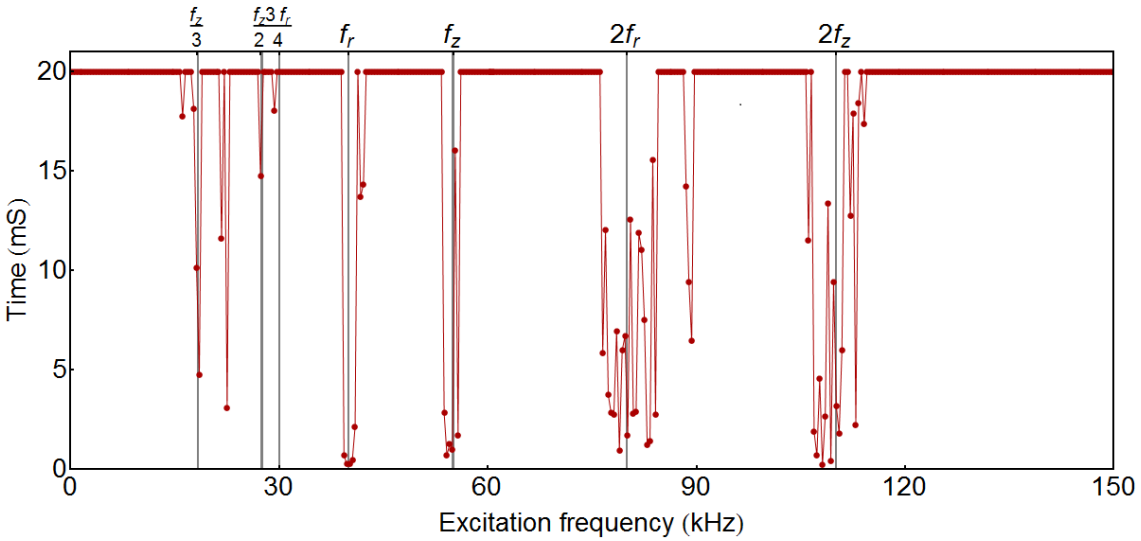

Figure 2.14: Figure shows the resonant excitation spectra of Rb^+ ions in the trap at the optimized trap parameters. The simulation is performed as explained in the text and the result $f_r = 40$ kHz and $f_z = 55$ kHz is close to the experimentally found values 43 kHz and 54 kHz respectively.

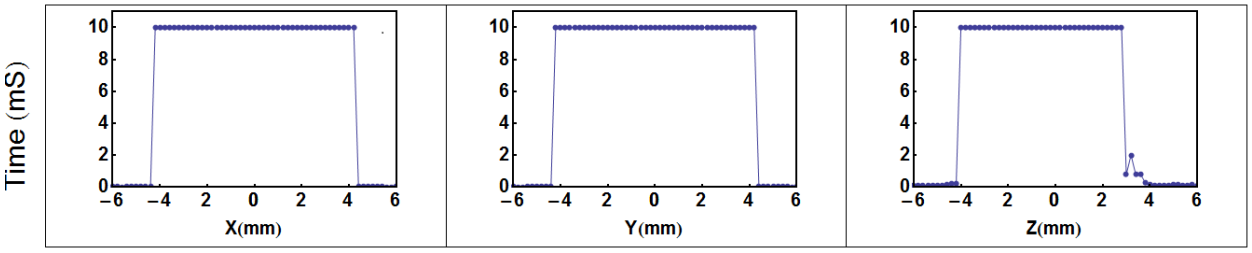

Figure 2.15: Figure represents the trap extent in the radial and axial directions for the optimized trapping parameters for Rb^+ ions.

be trapped. The depth is estimated in a similar method as for the trap extent. To find $\mathcal{U}_{r,z}$, an Rb^+ ion with initial position at the centre is evolved for 500 cycles with initial energy varying from 0 to 1 eV, keeping the velocity along the other two directions zero. Beyond $\mathcal{U}_r$=0.68 eV and $\mathcal{U}_z$=0.48 eV the ion is not stable and the results are shown in Fig. 2.16. The calculated trap depth in the radial and the axial directions are 0.68 eV and 0.48 eV respectively for Rb^+ ion. The depth is lower in $\hat{z}$ axis and is considered as the net trap depth at V_{rf} =80 V. The numerical code to determine the trap depth is given in Appendix B.

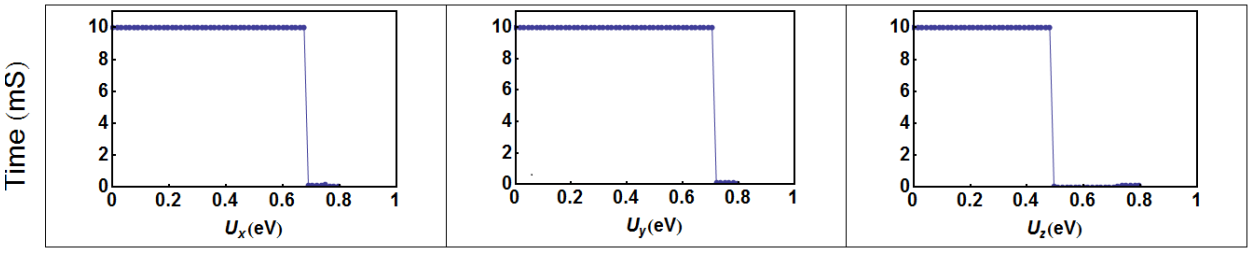

Figure 2.16: The trap depth in the radial and axial directions for the optimized trapping parameters for Rb^+ ions are shown in figure. The depth is lower in the axial direction and is considered as the depth of the ion trap.

2.4.2 The linear Paul trap

The secular field for the ion trap in XY direction is generated by applying an rf voltage between the diagonally opposite pairs of rods as shown in the Fig. 2.17. The axial trapping is ensured by creating a parabolic potential in the $\hat{z}$ direction by applying a small negative voltage on the tungsten wire pairs.

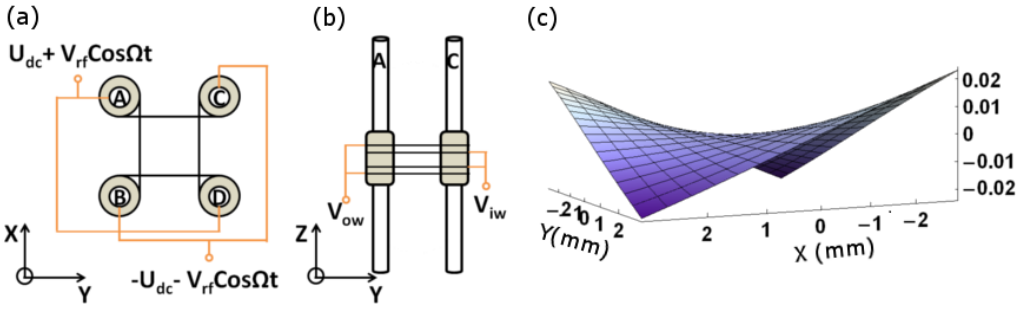

Figure 2.17: Panels (a) and (b) shows the biasing of the rod and wire electrodes to obtain a quadrupole potential in the XY plane and a harmonic potential in the z axis. The resulting potentials in the XY plane is shown in panels (c).

Near the trap centre, the generated potential can be written as

$$\phi(x,y,t) = \frac{x^2 - y^2}{2d^2}(U_{dc} + V_{rf}Cos\Omega t) \tag{2.13}$$

where d is the radial distance of the electrodes from the trap axis. The ion trajectory in the XY plane is governed by the equation of motion of the Mathieu type. For an ion of

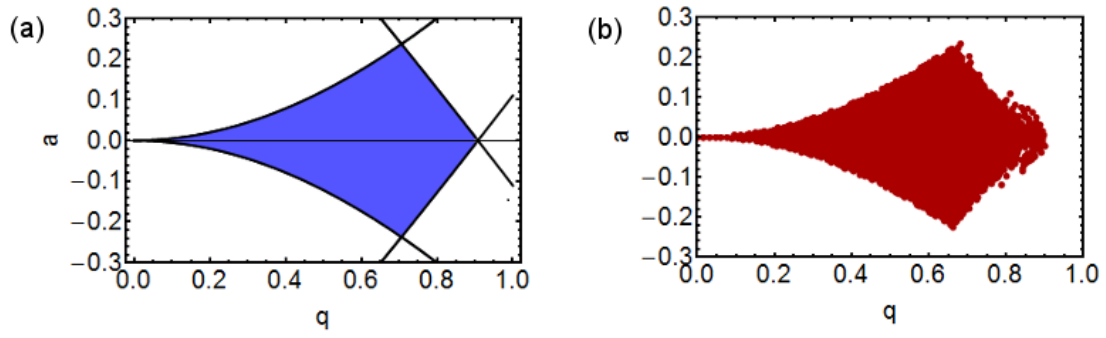

Figure 2.18: The first stability region for an ideal linear Paul trap is shown in panel (a) and the result of simulation for our linear trap is shown in panel (b).

charge Q and mass M, the equation of motion is written as

$$\ddot{x} = \frac{-Q}{Md^2}(U_{dc} + V_{rf}Cos\Omega t)x \quad ; \quad \ddot{y} = \frac{Q}{Md^2}(U_{dc} + V_{rf}Cos\Omega t)y \tag{2.14}$$

Expressing in terms of the Mathieu parameters

$$a_x = -a_y = \frac{-4QU_{dc}}{M\Omega^2 d^2} \quad ; \quad q_x = -q_y = \frac{2QV_{rf}}{M\Omega^2 d^2} \quad ; \quad \tau = \frac{\Omega t}{2} \tag{2.15}$$

the equation of motion takes the form

$$\frac{\partial^2 x}{\partial \tau^2} + (a_x + 2q_x Cos\Omega t)x = 0 \quad ; \quad \frac{\partial^2 y}{\partial \tau^2} + (a_y + 2q_y Cos\Omega t)y = 0 \tag{2.16}$$

The stability region for an ideal linear Paul trap (solution of eq. 2.16) is shown in Fig. 2.18(a). For our linear ion trap, the simulation performed in a similar way as for the spherical trap results in the $a - q$ diagram as shown in Fig. 2.18(b). The four tungsten wires are maintained at -3.5 V for axial trapping, the choice of which will be explained later. For further simulations in the linear trap, the (a, q) values are chosen to be (0, 0.34) which corresponds to the optimized voltages in the spherical trap, for comparisons.

Trap frequency

For the linear Paul trap the ion trajectory consists of micro and macro motion in the radial direction and a harmonic oscillation in the axial direction as shown in Fig.2.19.

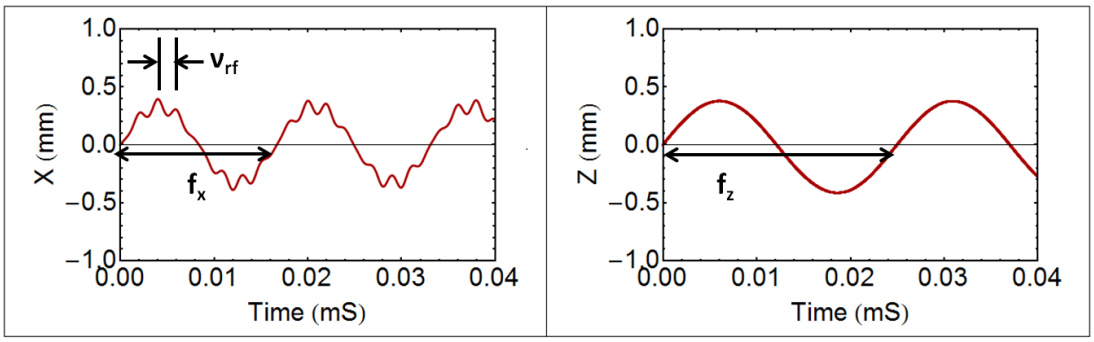

Figure 2.19: Figure shows the the micro and macro frequencies in the Rb^+ ion trajectory in $\hat{x}$ direction and the harmonic motion in $\hat{z}$ directions in the linear Paul trap operated at (a,q) = (0, 0.34) at rf frequency 500 kHz and V_{wires}= -3.5 V.

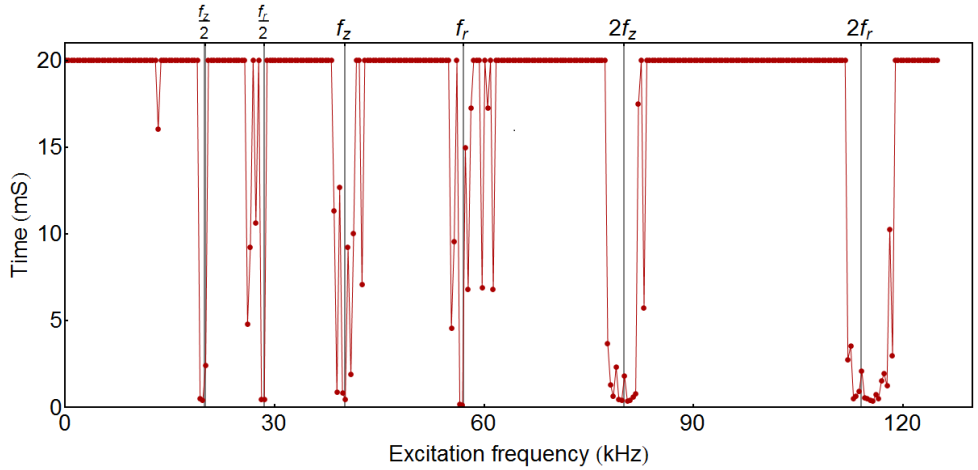

Figure 2.20: The simulated resonant excitation spectra of Rb^+ ions in the linear Paul trap with trapping voltages corresponding to (a,q) = (0, 0.34) at rf frequency 500 kHz is shown in figure. The wires are maintained at a dc voltage of -3.5 V.

The macromotion frequencies of Rb^+ ion with operating parameters (a,q) = (0, 0.34) at rf frequency 500 kHz and V_{wires}= -3.5 V, calculated by resonant excitation method is shown in Fig. 2.20. The macromotion frequencies are found to be 57 kHz in the radial and 40 kHz in the axial directions.

Trap extent and depth

The extent and depth for the linear quadrupole trap is estimated in a similar way as for the wire trap and the results are shown in Fig. 2.21 and Fig. 2.22. Clearly, even a small voltage applied on the wires for axial trapping will reduce the trap depth in the radial direction. For a given radial trapping rf voltage, the wire voltages are optimized to get reasonable trapping in all three directions as shown in Fig. 2.22. This voltage combination is found to be V_{wires} = -3.5 V for (a, q)= (0, 0.34). The trap extend for Rb^+

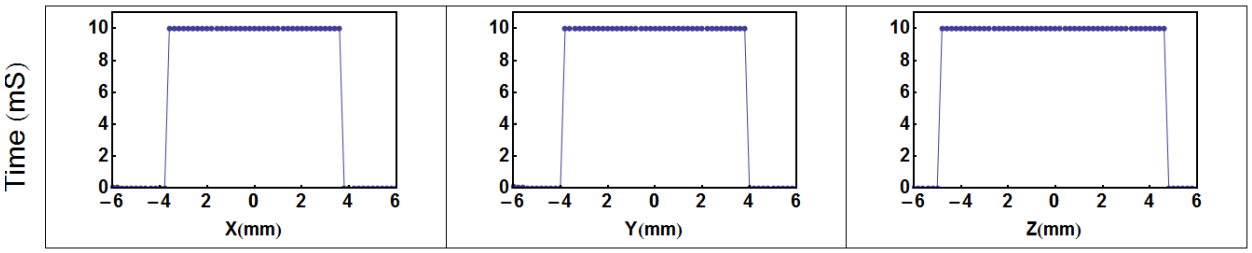

Figure 2.21: The spatial extent of the trap in radial and axial directions for Rb^+ ions are shown with the trapping parameters (a, q) = (0, 0.34) at rf frequency 500 kHz and V_{wires} = -3.5 V.

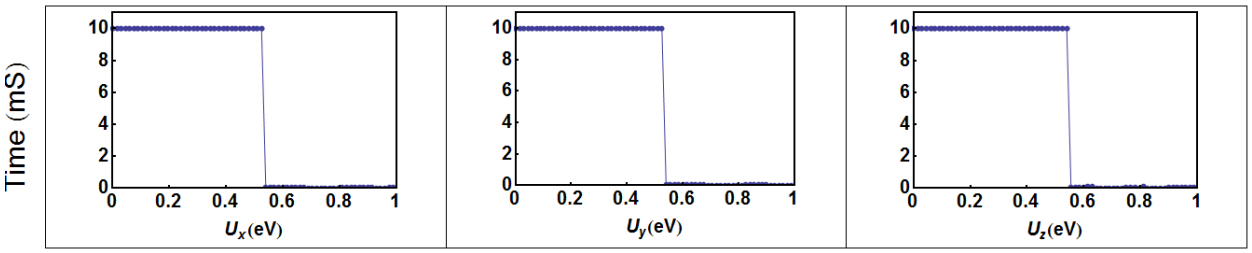

Figure 2.22: The trap depth in the radial and axial directions for Rb^+ ions in the linear Paul trap is shown in the figure with trapping parameters (a, q) = (0, 0.34) at rf frequency 500 kHz and V_{wires} = -3.5 V. The simulation is performed with different combinations of small voltages on the four wires and optimized the voltages to obtain a reasonable compromised trap depth in all three directions. This voltage combination is found to be close to V_{wires} = -3.5 V.

ions in the linear Paul trap with the above mentioned parameters is calculated to be 3.6 mm in radial and 4.6 mm in the axial directions, and the trap depth is $\mathcal{U}_r$= 0.53 eV and $\mathcal{U}_z$= 0.54 eV.

2.5 The dipole molecule trap

In principle all the experiments described so far would also be possible with a segmented linear Paul trap with an axial cavity. Where the thin-wire structure comes into its own is in its ability to allow strong constant fields about the trap volume. Fig 2.23(a) demonstrates that a relatively large electric field can be applied to trapped ensembles of atoms and molecules, which could then be probed by the cavity to make precision measurements on cold gases with tunable electric fields [22].

A further prospect with this electrode structure is the trapping of polar molecules, which can be done by a straight forward implementation of a gradient field trap, as demonstrated by Kleinert et. al. [23]. Consider a diatomic molecule in an electric field. Molecular states with non-vanishing orbital angular momentum split proportional to the electric field (linear Stark effect). For the ground state of a molecule (Σ), the only non-vanishing angular momentum is due to the rotation of the molecule and the lowest order Stark effect is quadratic in electric field given as

$$\Delta E = \frac{d^2 E^2}{B} \frac{J(J+1) - 3M_J^2}{2J(J+1)(2J-1)(2J+3)} = \alpha E^2 \tag{2.17}$$

where d is the dipole moment, B is the rotational constant, J is the total angular momentum, M_J is the projection of J onto the axis of the molecule and α is the molecular polarizability. The rotational states which are low-field seekers (positive Stark effect)

Table 2.2: The molecular constants of RbK, RbCs, KCs molecules are tabulated with the references in brackets.

Molecule	d	B	Reference
RbK	0.615	0.03839	[88,89]
RbCs	1.237	0.0169	[88,90]
KCs	1.906	0.03048	[88,91]

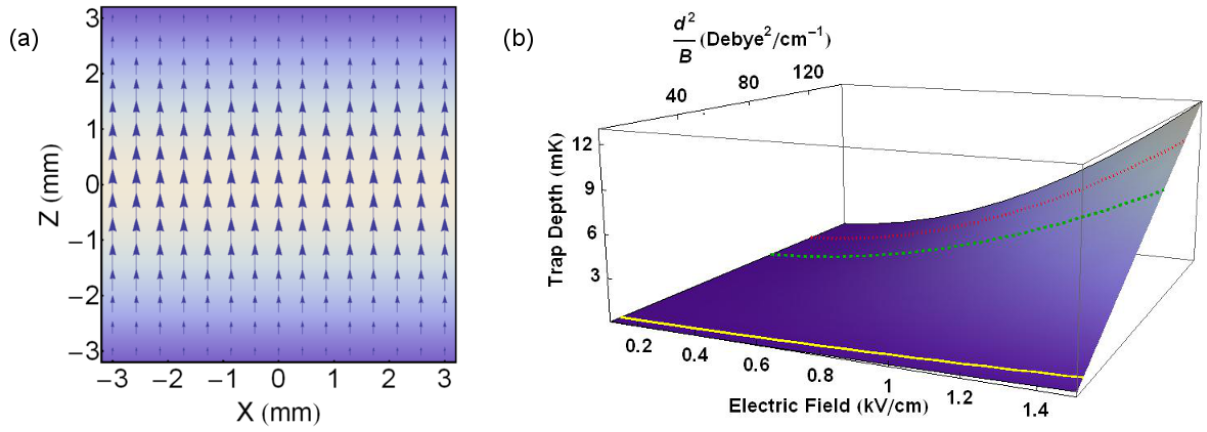

Figure 2.23: (a) Shows the electric field in the XZ plane when the inner two wires are $+1$ kV and -1 kV respectively, which can be tuned for precision measurements in uniform electric fields. (b) shows the variation of the trap depth for polar molecules with the electric field and $\frac{d^2}{B}$. The solid, dashed and dotted lines represents the trap depths for RbK, RbCs and KCs molecules respectively.

experience a force towards the field minimum. Fig. 2.23(b) shows the trap depth for hetero-nuclear diatomic molecules as a function of electric field and $\frac{d^2}{B}$. Trap depths of RbK, RbCs and KCs molecules in their rovibrational and electronic ground states are marked on this figure, where the molecular constants for the calculations are tabulated in Table. 2.2. The program is given in Appendix B.

2.6 Discussion

In this chapter, we discussed the background theoretical concepts for cooling and trapping atoms, trapping charged particles, and Fabry-Perot cavity. The hybrid trap developed is described in detail. The experimental arrangement for the production and detection of ^{85}Rb MOT is discussed. The spherical and linear ion traps are numerically characterized using Rb^+ ions. Finally trapping of neutral polar molecules in the hybrid trap is discussed. All the essential aspects of the hybrid trap have now been discussed at the level where the experiments with this system can now be presented.

CHAPTER 3

Radial Extraction and Phase Sensitive Detection

3.1 Overview

The detection of trapped ions in our hybrid trap is vital to the scientific goals of our experiment. As discussed earlier the ion-atom hybrid trap is built within a Fabry-Perot cavity for enhancing low signal levels and for frequency sensitive measurements of interactions in a mixture. As the cavity axis shares the symmetry axis of the ion trap, the conventional ion-extraction scheme along the trap axis is not practical. Hence a radial extraction method is devised and implemented. This is done by creating the conditions for imposing a potential gradient from the ion trap centre to the CEM, by the application of appropriate voltages on the electrodes in the experiment. Such a potential gradient extracts the ions out of the trap and is therefore destructive detection. The ion extraction is implemented in two cases. Case *A*: when the ions are detected by timing the ion extraction, while simultaneously switching the ion trap *off*. Case *B*: when the extraction is implemented with the ion trap kept *on*. The consequences of trapping rf *on* while transverse extraction in a spherical trap is demonstrated for the first time [28].

To reliably detect the Rb^+ and Rb_2^+ ions, we use the appropriate extraction of case *A* or case *B*, in order to do a reliable mass spectrometry or count the total number of trapped ions. In this chapter, we outline the experimental scheme for ion detection and compare the experimental data with extensive numerical simulation to put the entire technique on a firm footing.

In section 3.2, the radial extraction of a single species of ion in case *A* and *B* are discussed with example of Rb^+ ion. In section 3.3, extraction of multiple species of ions in

case A and B and mass spectroscopy with example of Rb^+ and Rb_2^+ ions are discussed.

3.2 Ion extraction with single species

3.2.1 Ion production and optimal trapping

The Rb^+ ions are created from Rb atoms in the MOT by resonant two photon ionization. The ionization potential for the Rb atom is 4.18 eV [84]. The MOT cooling laser (1.59 eV) excites the atom to excited $5P_{3/2}$ state, and are then ionized by the application of a blue laser (IBeam smart, Toptica) of 473 nm (2.63 eV). This is a very efficient production of ions in the ion trap as the ions are created at the centre and at an energy well within the trap depth.

As described in chapter 2, an rf voltage is applied to the inner pair of wires to trap the ions. The ion trap is operational during the creation of the ions. The rf source is a function generator (Agilent 33500B), the output of which is amplified using a wide band amplifier (Krohn-Hite 7602M). The rf trapping voltage for Rb^+ ions is optimized as follows. The optimal trapping parameters ensures long lifetime of the ions in the trap. For a range of trapping voltage V_{rf} at a convenient frequency 500 kHz and V_{ow}= -5 V, the ions are created in identical cycle, held in the ion trap and then extracted. The number of ions detected as a function of V_{rf} is analyzed and found that $V_{rf} \cong$ 75 V to 90 V gives a good lifetime for the ions as shown in Fig. 3.1. [19,21]. V_{rf}= 80 V is chosen for the rest of the experiments with Rb^+ ions.

3.2.2 Ion detection

The trapped ions are detected by extracting them onto a CEM mounted as described in chapter 2. The CEM is maintained at -2.4 kV even when the trap is operational, and a wire mesh (Grid 1) maintained in ground potential shields this voltage from the ion trap centre. To extract the ions, -120V (Agilent 3612A dc power supply) is switched *on* on the wire mesh and a high voltage 400V (Aplab HV DC power supply H0605) is

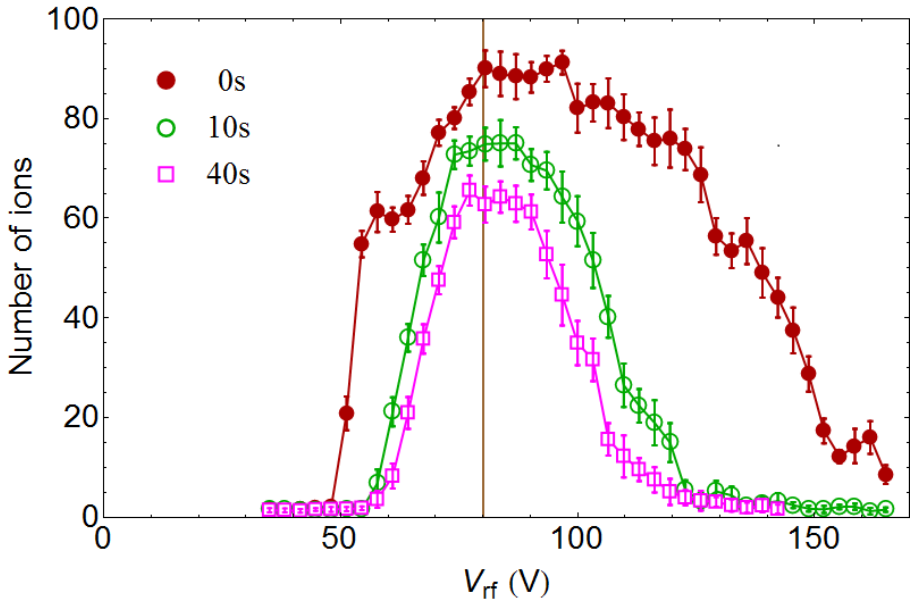

Figure 3.1: Figure shows the Rb^+ ion number vs trapping rf voltage at 500 kHz for different trap hold time [19,21]. V_{rf}= 80 V is chosen as the rf voltage for the rest of the experiments with Rb^+ ions.

switched *on* on the rods A and B while maintaining rods C and D at ground potential to accelerate the ions towards the CEM. The Grid 2 is grounded when trap is operational to shield the trap centre from any voltage applied on the cavity pzt and switched to 100 V during extraction to provide a symmetric extraction electric field. A high voltage switching circuit (Behlke switch) is used to switch these high voltages. The circuit diagram for the Behlke switch is documented in Appendix D. The resulting extraction potential in the XY plane is shown in Fig 3.2.

Ion extraction can be performed with rf *on* or rf *off* on the innerwires of the modified spherical Paul trap. If rf voltage is *on* during extraction, the arrival time distribution of the ions on the detector is found to be critically dependent on the rf phase at which the extraction voltages are switched *on* [13, 92]. To understand the extracted ion distribution in these two cases, a set of experiments at different extraction phases are performed and compared with the corresponding numerical simulations. Below we first discuss the consequences of ion extraction in the two cases when only the atomic ion of Rb^+ is created and trapped in the ion trap.

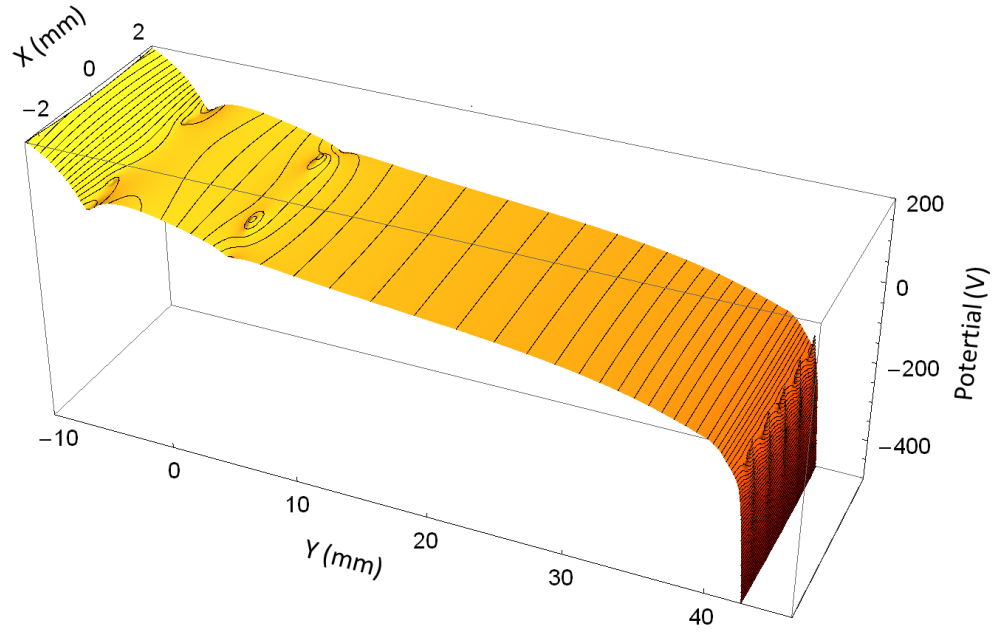

Figure 3.2: Figure shows the resultant extraction potential in the XY plane with the high voltages on the electrodes as mentioned in the text. The lines represents the equi-potentials.

While the presence of the ceramic sleeves on the extraction electrode (quadrupole rods) can be expected to modify the extraction field, in a manner that cannot be quantified numerically, the resulting change is small as borne out by the experimental measurements presented below and the close agreement with the numerical simulations of the ion extraction.

3.2.3 Ion extraction with rf *off*

The Rb^+ ions are loaded into the ion trap and held for a short time. The rf voltage on the inner wire pair is then switched *off* precisely when the rf amplitude crosses zero as shown in the inset of the Fig.3.3. In the same instant, the voltages on the extraction electrodes are switched *on* simultaneously. This results in an asymmetric time of flight (ToF) distribution, with a sharp onset and a relatively slower decline. The ToF peaks at 4.7 μS and the width of the distribution is approximately $\sim$ 0.5 μS. The red solid curve in Fig. 3.3 (a) illustrates the resulting experimentally measured ToF distribution of the Rb^+ ions. To obtain this signal, the data is collected with small ion number per

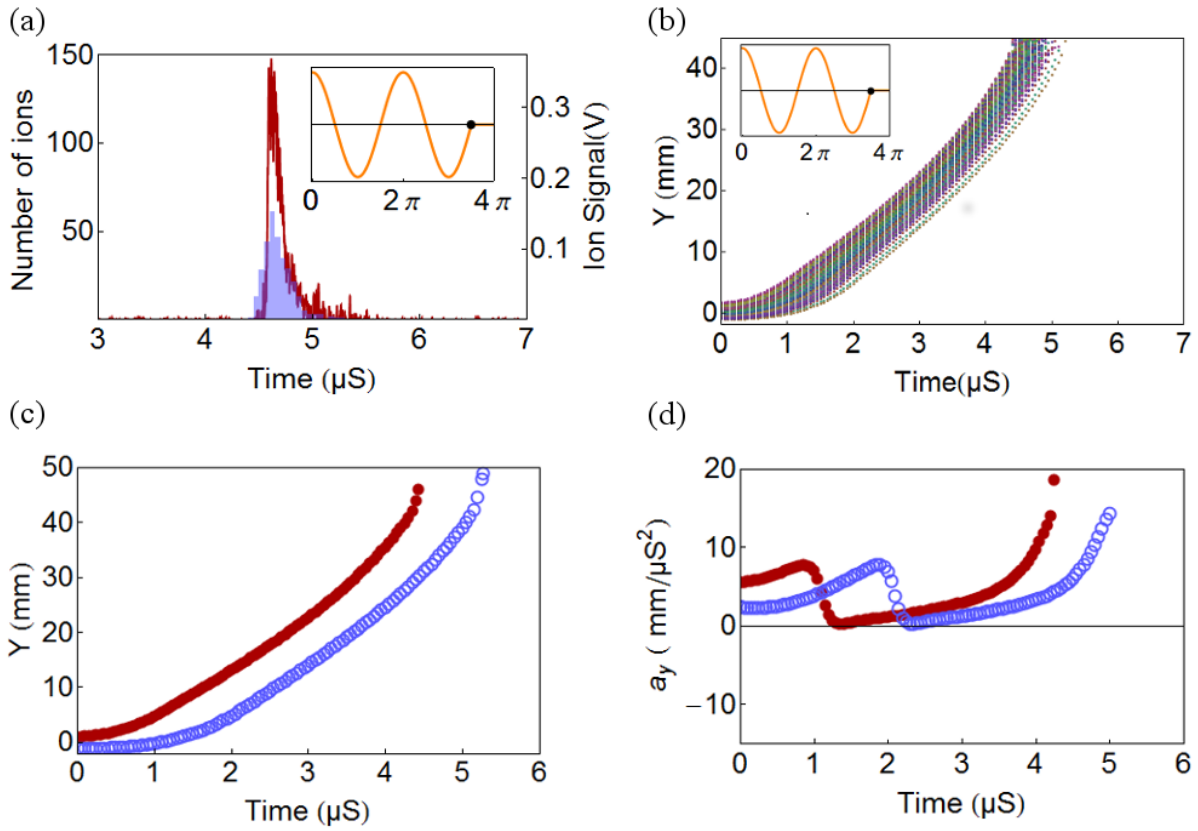

Figure 3.3: panel (a) shows the time of flight signal of Rb^+ ions. The extraction voltages are turned *on* and the rf trapping voltage is switched *off* simultaneously, when the rf amplitude crosses zero as shown in the inset. The red curve and the blue histogram represents the experimental signal and the simulation result respectively. Panel (b) shows the trajectory of 500 ions from the ion trap centre towards the CEM. As all the ions experience the same acceleration at the same spatial point, their trajectory is compact. The red and blue circles in panel (c) represents the trajectory of the ions which represents the two extremes of the ion ToF distribution. Panel (d) shows the acceleration experienced by these two ions as a function of time during their time of flight.

extraction to avoid being in the pile up regime and 20 such data are added together. The blue histogram in Fig. 3.3 (a) shows the simulated ToF distribution of Rb^+ ions. Here, 500 non-interacting ions are loaded into the trap with an initial Gaussian spatial distribution comparable to the size of the MOT and an initial Gaussian velocity distribution consistent with the trap depth. The ions are evolved for 500 rf cycles, and then extracted with the same voltage conditions as in the experiment. The simulation and experimental results are combined in the same plot with the left ordinate representing simulated ion number and the right ordinate showing the experimental signal voltage. The values on the two axes are independent and this convention holds throughout the chapter.

The trajectories of all the ions towards the CEM is shown in Fig. 3.3(b). The ions which reach at the two extremes of the ToF signal are identified and their trajectory is shown in Fig. 3.3(c). The acceleration for these two ions as they traverse the potential gradient is shown as a function of time in Fig. 3.3(d). Since the rf voltage is *off*, the extraction field is stationary in time and all the ions experience the same acceleration at the same spatial points.The potential and electric field experienced by the ions are illustrated by the blue curve (dot-dash) in Fig. 3.4(a) and 3.4(b).

3.2.4 Ion extraction with rf *on*

To understand the ion signal measured by the CEM, with rf voltage *on*, the ion trap is loaded with Rb^+ ions and held for the same duration as in the previous case. Now the extraction voltages are switched *on*, while the trap is operational. The extraction voltage is chosen to be a few times higher than the trapping rf voltage to ensure that all the ions are extracted in a single sweep and that a fraction of the ions does not oscillate in trap while extraction. Along the line of extraction, the ions experience a field which is resultant of the field due to extraction voltages and the instantaneous rf voltage. This is illustrated in Fig. 3.4(a). The different lines representing the potential along the extraction axis at different rf phases are indicated in the inset. Fig. 3.4(b) shows the corresponding electric field as a function of space. The extraction field at

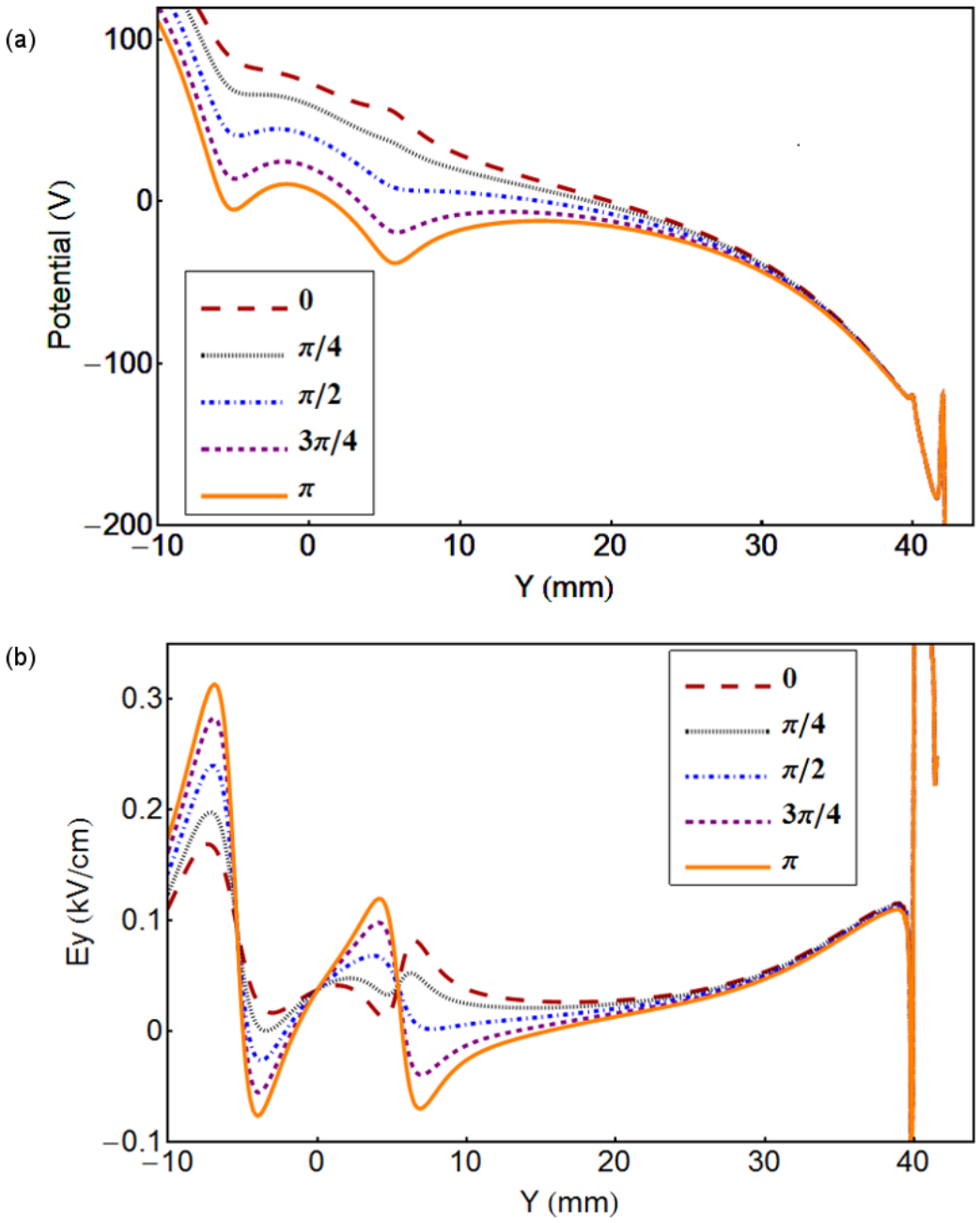

Figure 3.4: (a) shows the resultant extraction potential along the line of extraction (at x = z = 0) at different phases of the rf trapping field. The extraction potentials at different phases are plotted in different colors and line styles and the inset represents the corresponding phase points. The applied extraction voltages are described in the text. The curves in panel (b) are the corresponding electric fields along the extraction axis.

any point along the extraction axis varies in time at the rf frequency (500 kHz). Hence the acceleration that an ion gets at any spatial point is determined by the instantaneous field at that point.

Measurements are done by switching *on* the extraction voltages at different phases of the rf voltage as represented by the insets in Fig 3.5. The arrival time of the ions on the CEM from various locations in the ion trap is significantly affected by the phase of the rf voltage at which the extraction voltages are switched *on*. Hence the corresponding ToF distribution differ for different phases of extraction and is shown in Fig 3.5. The red curve and the blue histogram are the experimental signal and result of simulation respectively and they agree quite well with each other.

The trajectory of the 500 ions towards the CEM for four selected phases of extraction (a) 0, (b) $\pi/2$, (c) $5\pi/4$ and (d) $7\pi/4$ are shown in Fig 3.6. In Fig 3.7, the trajectory of the two extreme ions and their acceleration as a function of time are shown for these phases. At the instance when the extraction voltages are switched *on*, independent of the phase of rf voltage, the ions closer to the CEM experience greater acceleration as can be seen from Fig 3.7. As the ions travel towards the CEM, the distribution spreads or narrows down because of the space and time dependent extraction electric field.

For the case, when the extraction voltages are switched *on* at the rf phase $\phi = 0$ of cosine, the acceleration experienced by the ion$_n$ (the ion near to the CEM) and the ion$_f$ (the ion away from the CEM) is always positive. Therefore the ion velocity is always increased and hence the ToF distribution peaks at 4.3 μS. The ToF signal is narrow in this case because the overall acceleration experienced by all the ions are similar.

Now consider the case, when the extraction voltages are switched *on* at the rf phase $\phi = \pi/2$ of cosine. The ion$_n$ always experiences a positive acceleration but the ion$_f$ experiences deceleration at multiple points along the extraction direction. This results in widening of the arrival time distribution of the ions on the CEM.

The spread in ToF increases roughly as the extraction phase changes from $\phi = 0$ up to π and then decreases as the phase changes from $\phi = \pi$ to 2π. This is confirmed by both experiment and simulations. If the ions are extracted at the phase $\phi = 5\pi/4$

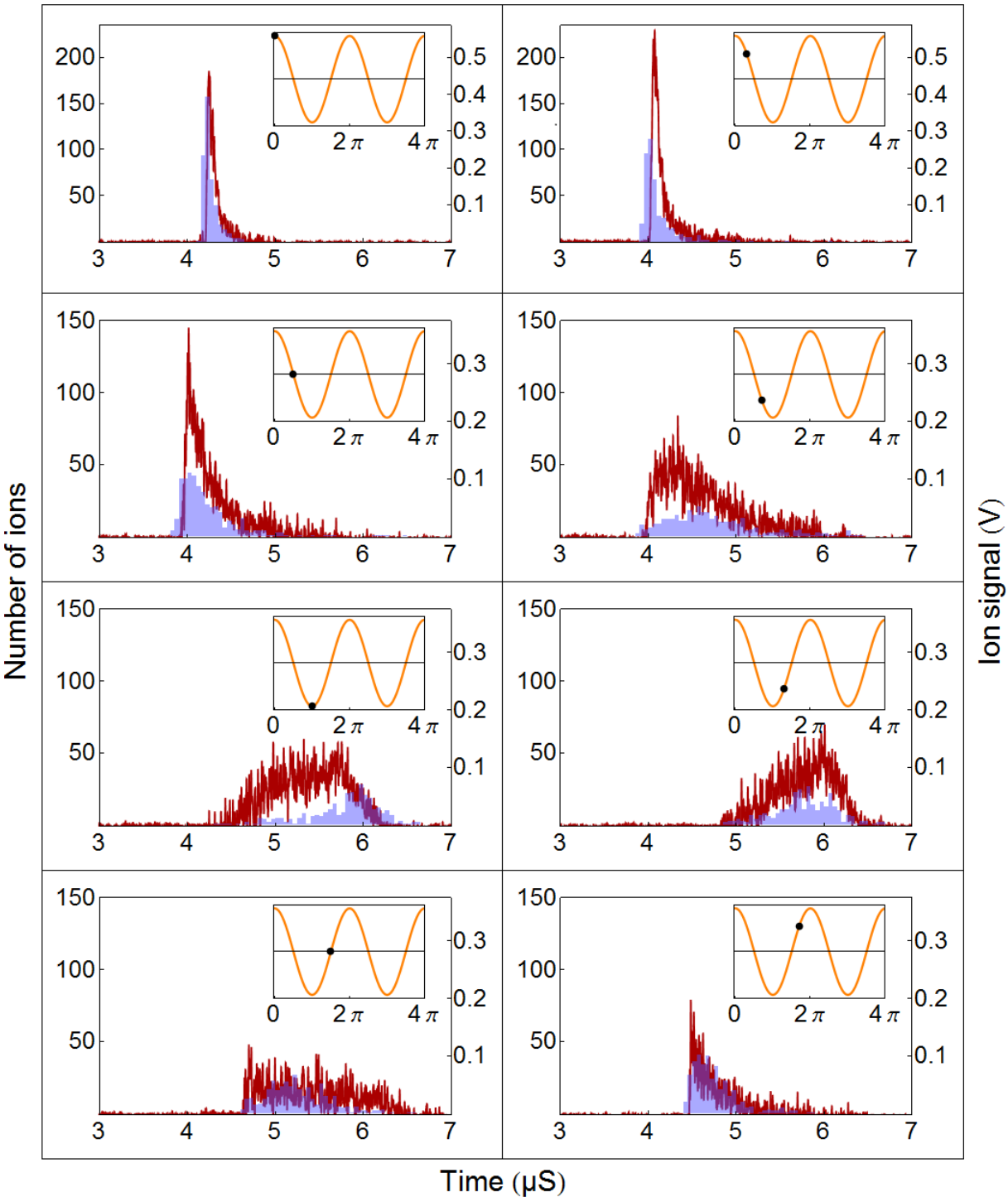

Figure 3.5: The figure shows the Rb^{+} ion ToF signal when extracted with the trapping rf field *on*. The inset in each panel represents the rf phase ϕ at which the high voltages for extraction are switched *on*. The red curve and the blue histogram are the experimental signal and the simulation result respectively.

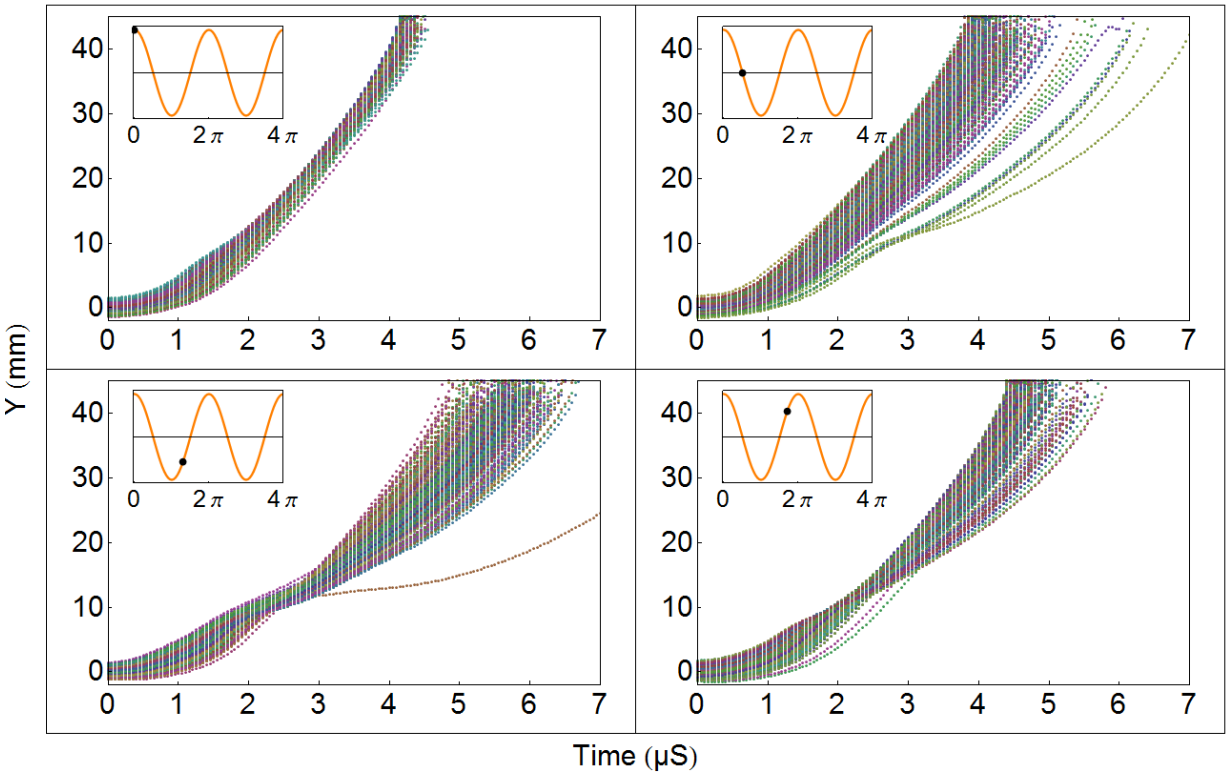

Figure 3.6: The trajectory of 500 extracted ions from the trap centre towards the CEM for selected phases of extraction are shown in the figure. For the phase ϕ =0, all the ions follows a compact trajectory. When $\phi = \pi/2$, the ion's distribution disperses in space and time. For phases $\phi = 5\pi/4$ and $7\pi/4$, the ion distribution focusses and then disperses.

of cosine function, both ion_n and ion_f experience deceleration at different points along the extraction direction, which results in an increase in the average ToF. In this case, the ion_n experiences much more deceleration than ion_f and hence the ion distribution gets spatially focussed first and then diverges, giving rise to a spread in the time of flight signal.

The evolution of ions towards the CEM in case of extraction at the phase $\phi = 7\pi/4$ is similar to that of phase $\phi = 5\pi/4$. But in this case, ion_n and ion_f experience less deceleration than at phase $\phi = 5\pi/4$. Also the difference in deceleration between the ions is less for $\phi = 7\pi/4$. Hence both the mean time of arrival and the spread of ToF decreases.

The ion detector, channel electron multiplier, has a dead time of $\sim$ 8 nS and hence a second ion arriving within $\sim$ 8 nS cannot be reliably detected as an independent

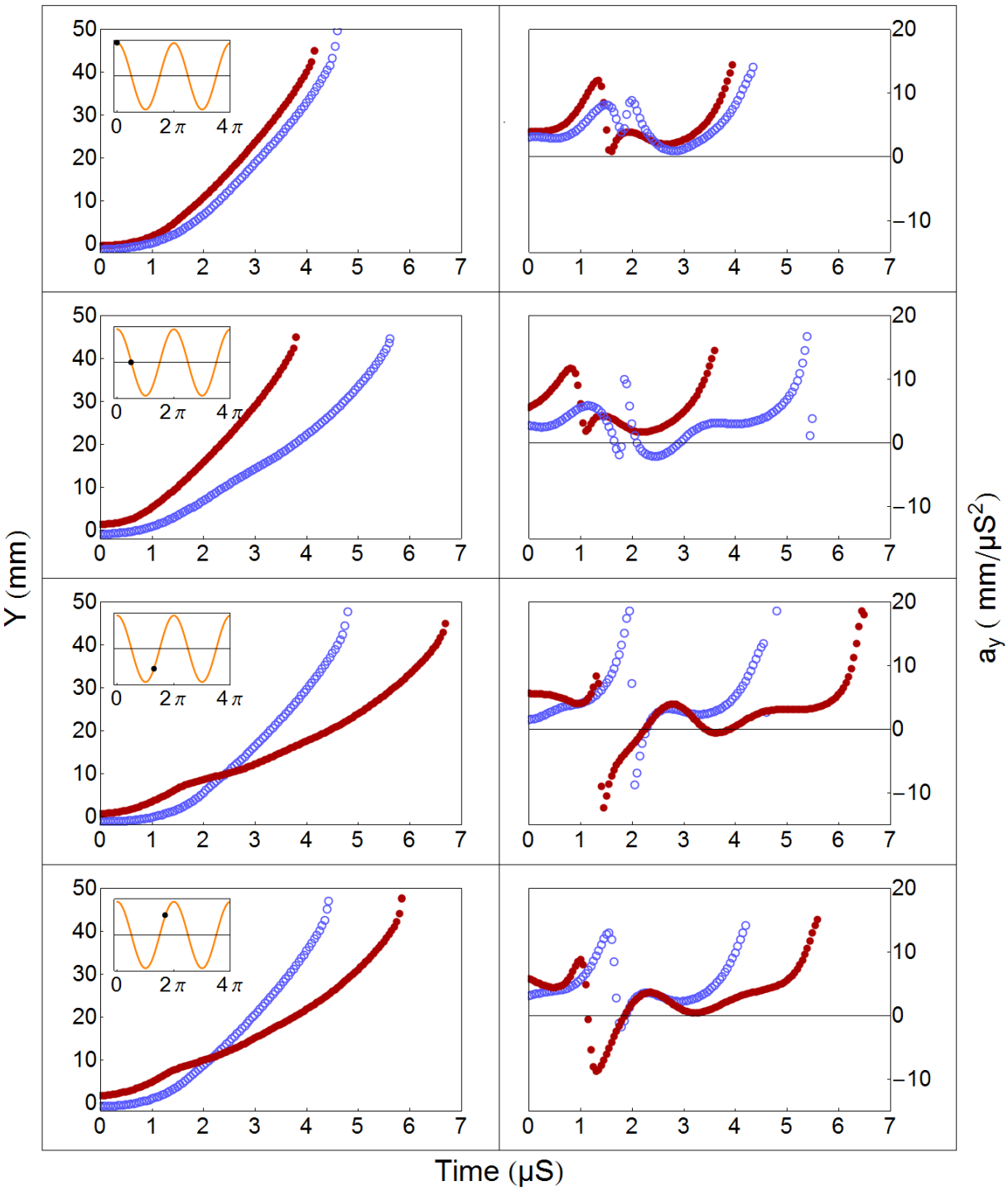

Figure 3.7: The left panels of the figure shows the trajectory of the ions reached at the two extremes of the ToF signal for four different selected phases as in Fig. 3.6. In the right panel, the acceleration experienced by these ions is shown as a function of time.

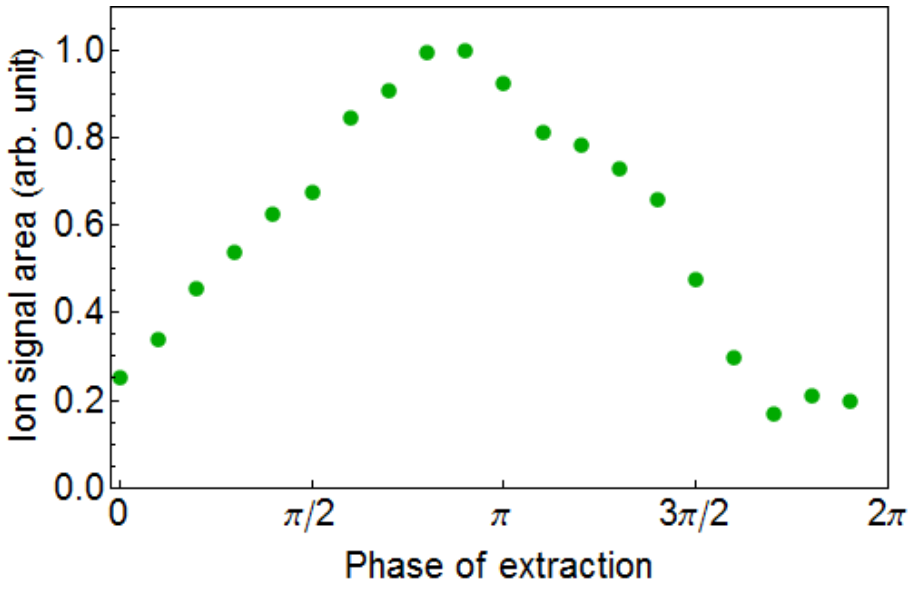

Figure 3.8: The figure shows the variation of normalized area under the curve of the ToF distribution for similar numbers of trapped ions, as a function of extraction phase. The maximum area is obtained when the extraction pulse is switched at a phase slightly below $\phi = \pi$ as this is the phase at which the ion ToF distribution is widest. When the ToF distribution is narrow, the ion detection efficiency goes down because of the pile up of ions in the detector.

event. This situation comes about when multiple ions with the same mass/charge ratio (M/Q) are extracted, and is known as pile up. As a result, the ion detection without pile up is limited to 50 ions/μS. In a conventional mass spectrometer, the basic idea for solving the ion pile up and for achieving a good mass resolution is to increase the distance between the trap centre and the detector thus increasing the flight time of like ions. This is impractical in our experimental system due to short distance between the trap and the detector in our design.

When the ion distribution is narrow, several ions reach the CEM within its dead time leading to under-counting of the ions. We make use of the temporal dispersion of ions when extracted in presence of rf field to eliminate the ion pile up in the detector. Fig. 3.8 shows the area under the curve of the ToF distribution as a function of phase of extraction. When extracting at phase $\phi \approx \pi$, the temporal dispersion is maximum resulting in least pile up and a reliable ion count. Hence this extraction phase is chosen for Rb^+ ions in our experiments.

3.3 Ion extraction with multiple species

Mass spectrometry is a general method for identification of masses in a mixture. In hybrid trap experiments, when atoms, ions and molecules are co-trapped, the identification of product ions formed is very important. Especially when the ion number is small, mass spectrometry offers reliable measurement of branching ratio of the processes. Here we study the effect of extraction phase on mass spectrometry using Rb^+ and Rb_2^+ ions.

When multiple ion species of same charge Q and different masses m_1 and m_2 ($m_1 < m_2$) are extracted in a typical mass spectrometer (having uniform extraction electric field), the ratio of the ToF of the ions is $T_{m2}/T_{m1} = \sqrt{(m_2/m_1)}$. However if the rf voltage is *on* while extraction, the temporal sequence of the ion's ToF are significantly altered and hence T_{m1} and T_{m2} are not related by the above expression. It is therefore essential to understand the possibility of performing mass spectrometry when the ions are being extracted in the presence of the rf voltage.

3.3.1 Ion production and trapping

The Rb^+ and Rb_2^+ ions are created simultaneously from the MOT using a pulsed dye laser. The details of the ion production will be described in chapter 5. Both the species of ions are trapped in the ion trap with $V_{rf} = 130$ V at 500 kHz and $V_{outer} = -5$ V. The V_{rf} is chosen to be in between the optimized voltages for Rb^+ and Rb_2^+ ions to simultaneously trap both the ion species.

The number of ions produced per shot is small and hence it ensures that any space charge effect doesn't play any role which folds into the mass spectrum. Another important advantage of working with low number of ions is that it avoids the detector pile up effect and reliable ion counting and mass spectrometry are possible.

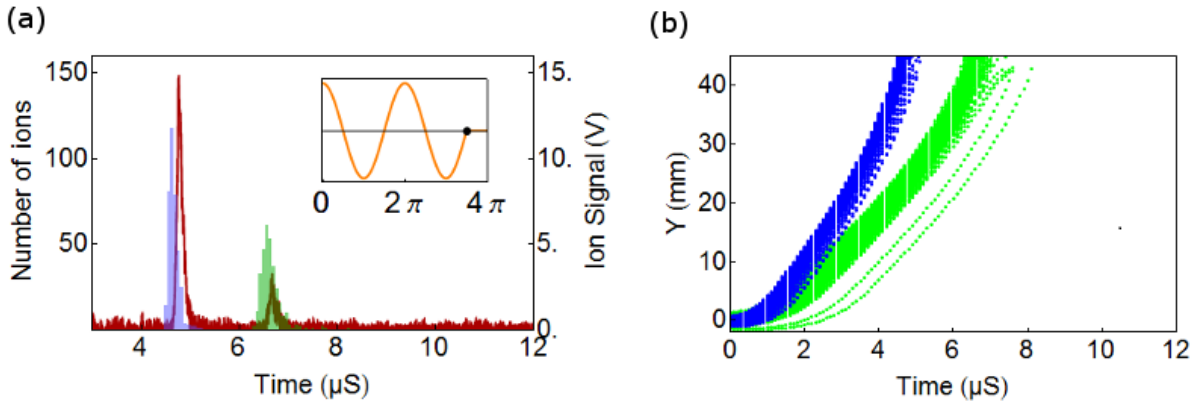

Figure 3.9: (a) The mass spectrometry for the transverse extraction of ions from the modified spherical ion trap when extracted with the trapping rf voltages on the inner wires switched *off* is demonstrated with Rb^+ and Rb_2^+ ions. The red curve is the experimental signal and the blue and green histograms represents the simulated ToF for Rb^+ and Rb_2^+ ions respectively. ToF $(Rb^+) \cong 4.7\ \mu$S and ToF $(Rb_2^+) \cong 6.7\ \mu$S satisfying the relation $T_{m2} = \sqrt{2} \times T_{m1}$. In panel (b), the trajectory of 500 Rb^+ and Rb_2^+ ions towards the CEM is shown by blue and green circles respectively.

3.3.2 Extraction with rf *off*

The ions are created in the trap, held for a short duration and extracted as discussed in section 3.2.3. The resulting ToF distribution of the Rb^+ and Rb_2^+ ions is shown in Fig. 3.9(a). The red curve is the experimental signal which is an accumulated count of 4000 creation and extraction cycles.

Here we assign the masses of Rb^+ and Rb_2^+ ions respectively as m_1 and $m_2 = 2 \times m_1$. The blue and green histograms in Fig 3.9(a) represents the simulated ToF of Rb^+ and Rb_2^+ ions respectively. From both experiment and simulation, $T_{m1} \cong 4.7\ \mu$S and $T_{m2} \cong 6.7\ \mu\text{S} = \sqrt{2} \times T_{m1}$. The trajectory of 500 Rb^+ and Rb_2^+ ions are shown in Fig 3.9(b) by blue and green points respectively.

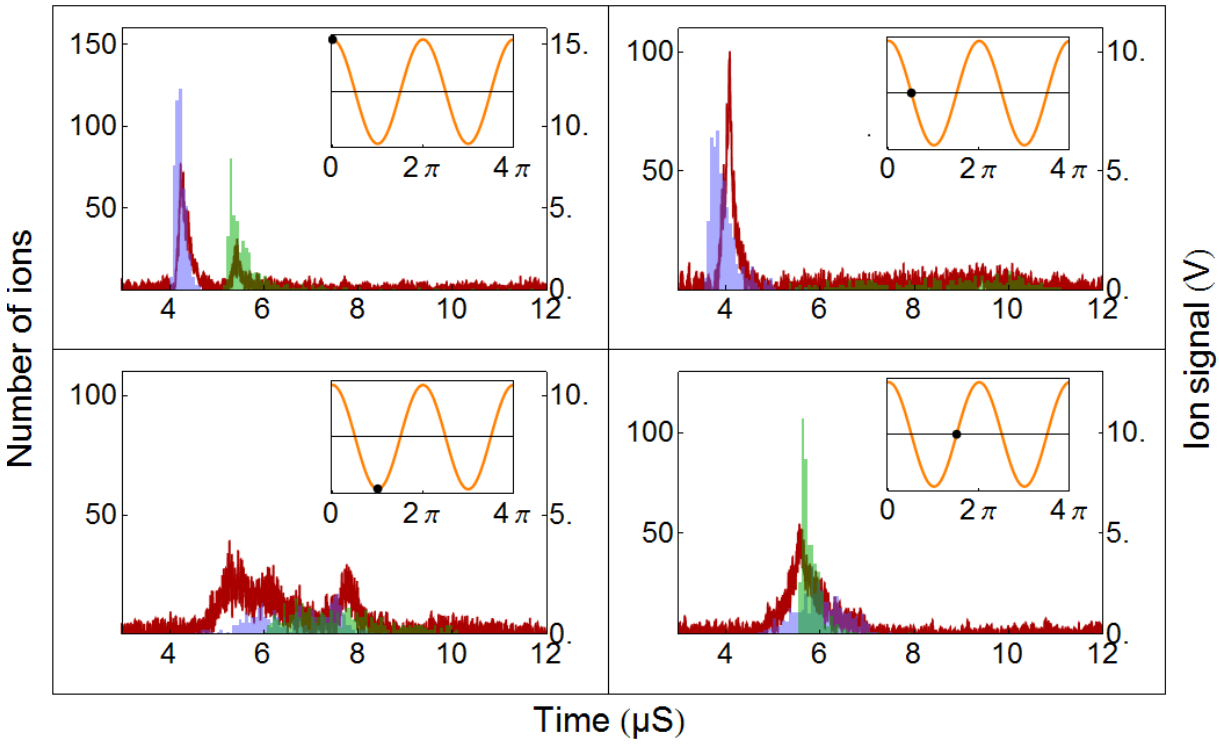

Figure 3.10: The ToF signal of Rb^+ and Rb_2^+ ions when extracted with rf voltage kept *on* is shown for the phases phases $\phi = 0,\ \pi/2,\ \pi$ and $3\pi/2$ in panels 1 to 4. The inset indicates the rf phase at which the extraction voltages are switched *on*. The red curves are the experimental signal and the blue and green histograms are simulated ToF for Rb^+ and Rb_2^+ ions respectively. The mass spectrometric relation $T_{m2} = \sqrt{2} \times T_{m1}$ is not satisfied when extracting with rf voltage *on*.

3.3.3 Extraction with rf *on*

The experiment is repeated by extracting the ions at different rf phases and the result is shown for phases $\phi = 0, \pi/2, \pi$ and $3\pi/2$ in Fig 3.10 in panels 1 to 4. The simulation for Rb^+ ions ToF is repeated with $V_{rf} = 130$ V and similar simulation is done for Rb_2^+ ions.

When the extraction voltages are switched *on* at phase $\phi = 0$ of cosine function, both Rb^+ and Rb_2^+ ions ToF peaks are distinguishable even though the average ToF and the peak separation are reduced. At extraction phase $\phi = \pi/2$, Rb^+ ion arrival time distribution is still narrow but Rb_2^+ ion arrival time distribution is spread from ~ 5 μS to ~ 11 μS. The Rb_2^+ ion signal is still distinguishable from Rb^+ ions in this case.

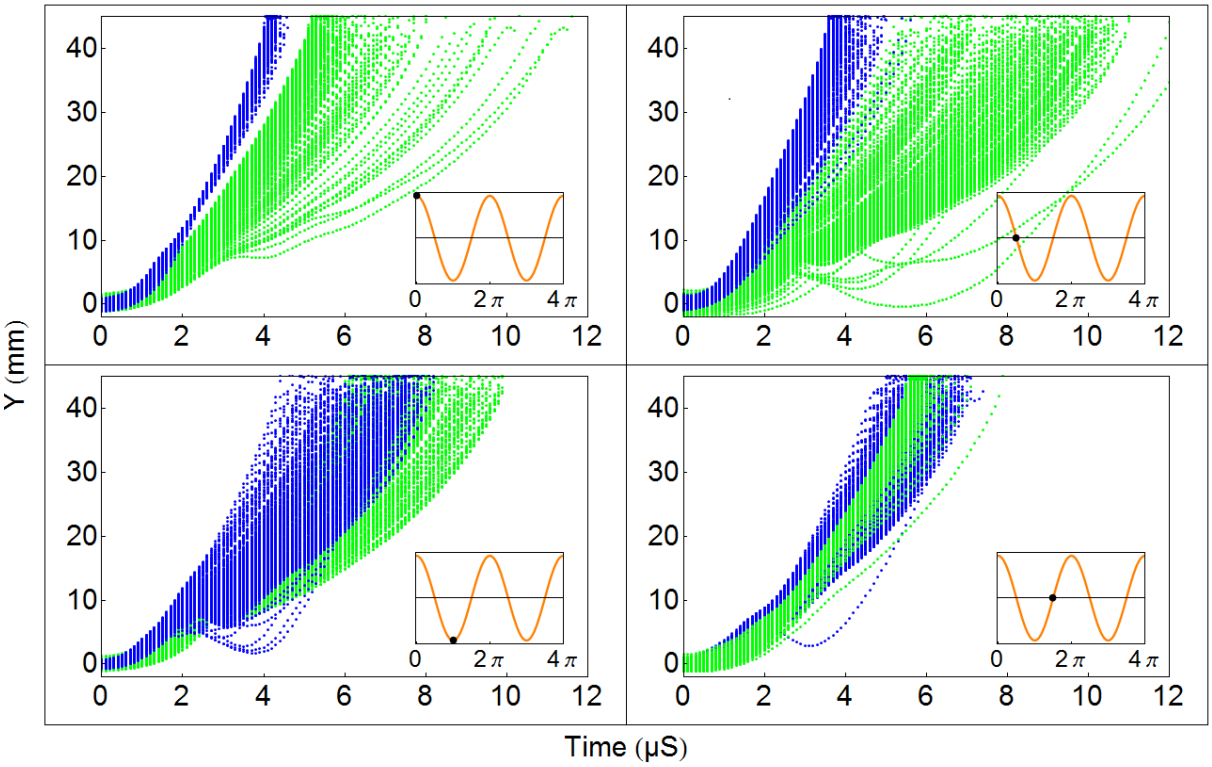

Figure 3.11: Figure shows the trajectory of 500 Rb^+ and Rb_2^+ ions represented by blue and green circles respectively when extracted at phases $\phi = 0,\ \pi/2,\ \pi$ and $3\pi/2$. For the phase ϕ =0, the Rb^+ and Rb_2^+ ions are detected separately at the detector and hence will be distinguishable in the ToF spectrum. As the phase increases from $\phi = \pi/2$ to $\phi = 3\pi/2$, the trajectories of Rb^+ and Rb_2^+ ions mixes up resulting in their indistinguishability in the mass spectrum.

As can be seen from the panels 3 and 4 of Fig 3.10, Rb^+ and Rb_2^+ ion ToF signals are merged and indistinguishable experimentally when the extraction phase are $\phi = \pi$ and $3\pi/2$. In the simulated ToF distributions,the arrival times of different ion species can be tracked and hence can be distinguished from each other in the overlapped signal.

The ToF of the two ion species with mass ratio 2 merge at these two phases because of the space and time dependent extraction field. The higher mass (Rb_2^+) experiences a more favourable overall acceleration compared to the lower mass (Rb^+). Hence both the species could arrive at the detector nearly the same time. Thus, for a mass spectrometric identification in a mixture of trapped ions, the trapping rf voltage should be switched *off* while extraction. In Fig 3.11, the trajectory of 500 Rb^+ and Rb_2^+ ions

towards the CEM is shown by blue and green circles respectively.

3.4 Discussion

The radial extraction of ions for single and multiple ion species are studied in the modified spherical ion trap. The specific cases of ion extraction with the trapping rf voltages *on*/*off* while extraction is analyzed in detail for single and multiple species of ions. In case of single ion species, the temporal dispersion in ion ToF signal when extracted at specific rf phase is utilized to solve the ion pile up problem in the detector. We demonstrated that for a reliable mass spectroscopy of multiple ion species, the extraction should be performed with trapping rf voltage switched *off*. In all cases presented, the experimental data and the result of numerical simulations performed by explicitly solving the ion equation of motion, matches very well. The techniques presented above will be utilized for future studies in trapped ion-atom mixtures. The experiments and simulations in this chapter are reported in [28].

CHAPTER 4

Diatomic molecules and photo association

4.1 Overview

In our experimental system, the production, simultaneous trapping and detection of cold atoms and ions have already been established. The next step in the realization of the hybrid trap and corresponding experiments is the addition of molecules. At present, various groups in the field are investing cold molecules, since they provide a critical element and diversify the study of interactions. As already explained in chapter 2, molecular ions and neutral polar molecules can be trapped using electric fields in the apparatus enabling to perform a variety of experiments.

Even though the field of cold molecules has open from 1980s, as we were dealing with the molecules for the first time in our experiment, we need to set the base for the production mechanisms and for understanding and modeling the results. We have extensively used the experimental and numerical results from literature such as the molecular potential energy curves, transition dipole moments and code for finding the molecular vibrational levels. In addition, we have developed few numerical codes for the calculation of continuum wave function, Frank - Condon overlap, spontaneous and stimulated transition rates and to find the branching ratio in spontaneous emission. These codes are extensively used in the chapter 5 to explain the experimental results with molecular ions.

The work in this thesis mainly deals with the studies on diatomic homo-nuclear molecules, specifically Rb_2 and Rb_2^+. This chapter starts with the basic theory for diatomic molecules and then goes to the details of the numerical codes developed. The cold molecule production methods used in the experiments are then discussed. The energy level struc-

ture of Rb_2 and Rb_2^+ molecules relevant for the experiments are given and the results of numerical calculation of transition rates are presented.

4.2 Diatomic molecules

4.2.1 Electronic energy levels

A diatomic molecule with spin-orbit angular momentum coupling is described by the time independent Hamiltonian

$$\widehat{H} = -\frac{\hbar^2}{2}\sum_{\alpha}\frac{\nabla_{\alpha}^2}{m_{\alpha}} - \frac{\hbar^2}{2m_e}\sum_{i}\nabla_i^2 + \frac{Z_{\alpha}Z_{\beta}e^2}{4\pi\epsilon_0 r_{\alpha\beta}} + \frac{e^2}{4\pi\epsilon_0 r_{ij}^2} - \sum_{\alpha}\sum_{i}\frac{Z_{\alpha}e^2}{4\pi\epsilon_0 r_{\alpha i}} + H_{SO} \tag{4.1}$$

where α, β represents the two nuclei with atomic numbers Z_{α}, Z_{β} and i, j represents the electrons. The SI system of units is adopted here. The nuclear and electronic motions can be decoupled under the Born-Oppenheimer approximation, which takes into account the fact that the electron is orders of magnitude lighter than the nuclei and hence the electron wave function can be computed to a very good approximation, assuming stationary molecular nuclei. As a result, under this approximation, the nuclear kinetic energy term is omitted in the Hamiltonian and the Schrodinger equation for the electronic motion can be written as

$$(-\frac{\hbar^2}{2m_e}\sum_{i}\nabla_i^2 + \frac{e^2}{4\pi\epsilon_0 r_{ij}^2} - \sum_{\alpha}\sum_{i}\frac{Z_{\alpha}e^2}{4\pi\epsilon_0 r_{\alpha i}} + \frac{Z_{\alpha}Z_{\beta}e^2}{4\pi\epsilon_0 R} + H_{SO})\psi_{el} = U\psi_{el} \tag{4.2}$$

where $R = r_{\alpha\beta}$ is the internuclear separation. Eq. 4.2 is solved for a range of internuclear separation R, and the eigen energy as a function of R, U(R), are the electronic potential energies for a quantum state. If U(R) exhibits a global minimum at an internuclear distance $R = R_0$, stable bound levels exist for the molecule in that electronic state. U(R$\rightarrow \infty$) is the sum of the energies of the constituting atoms in their electronic state. R_0 is called the equilibrium distance and the quantity $D_e = U(\infty) - U(R_0)$ is called the dissociation energy for that molecular state. The molecular electronic states of Rb_2 and Rb_2^+, relevant for the experiment are described in sections 4.4.1 and 4.6.1

respectively.

The transition probability between two electronic states, ψ_{el}^m and ψ_{el}^n is proportional to $\left|\left\langle \psi_{el}^m|\hat{d}|\psi_{el}^n \right\rangle\right|^2$, where $\hat{d}$ is the electric dipole moment of the molecule. The integral $\left\langle \psi_{el}^m|\hat{d}|\psi_{el}^n \right\rangle = d_{mn}$ is called the electronic transition dipole moment (TDM) of the molecule between electronic states ψ_{el}^m and ψ_{el}^n.

Since the electrons move much faster than the nuclei, for any change in the nuclear configuration, the electrons adjust to this change quickly by changing its energy. In other words, the electronic energy curves, U(R) are the potential energy for the nuclear motion and the Schrodinger equation for the nuclear motion can be written as

$$(\frac{-\hbar^2}{2}\sum_i \frac{\nabla_\alpha^2}{m_\alpha} + U(R))\psi_N = E\psi_N \tag{4.3}$$

where E is the total energy of the molecule. The nuclear motion is described in detail in section 4.2.3.

4.2.2 Angular momentum coupling and Hund's cases

The potential energy curves (PEC) determined by the solution of the Schrodinger equation 4.2 depends on the relative strength of electrostatic and spin-orbit interaction. Hund formulated different angular momentum coupling schemes and are referred as Hund's case a, b, c, d, and e. Hund's cases (a) and (c) are the coupling schemes important for the works presented and are described in this section.

Hund's case (a)

The angular momentum coupling in the Hund's (a) and (c) cases are schematically represented in the Fig. 4.1. When the internuclear distance is small, the nuclear electric field along the molecular axis is stronger than the spin-orbit interaction and hence the total orbital angular momentum $\vec{L}$ and the spin angular momentum $\vec{S}$ of the molecule precess around the internuclear axis. The projections of $\vec{L}$ and $\vec{S}$ onto the internuclear axis, Λ and Σ respectively, are conserved and are good quantum numbers. The Schrodinger equation is solved without the term H_{SO}. The orbital angular momentum

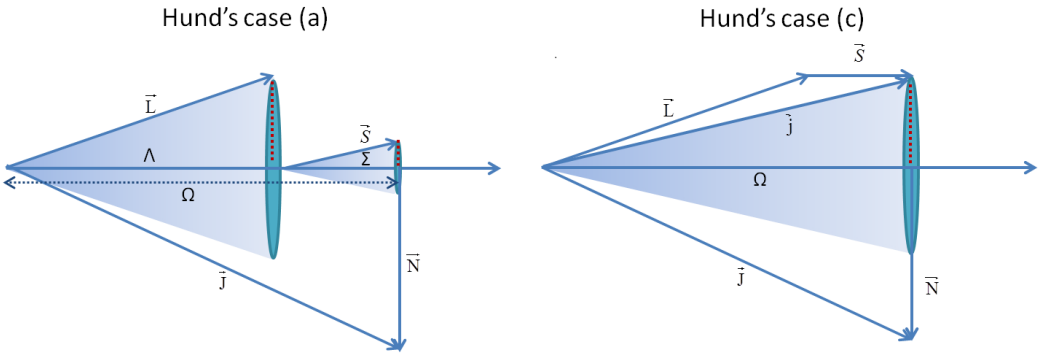

Figure 4.1: The schematics represent the angular momentum coupling in Hund's case (a) and Hund's case (c). In Hund's case (a), Λ and Σ are good quantum numbers and in Hund's case (c), Ω is good quantum number.

quantum number $\Lambda \geq 0$ and the states corresponding to Λ =0, 1, 2, 3 etc. are labeled as Σ, Π, Δ, Φ etc. Each state has a multiplicity of $2S+1$ and the states are labeled as ${}^{2S+1}\Lambda^{\pm}_{g,u}$, where the notations $\pm$ and g, u are explained below.

For a diatomic molecule, the electronic Hamiltonian is invariant under reflection in any plane containing the internuclear axis. As the state Λ=0 (Σ) has no orbital angular momentum, they are non-degenerate and to completely specify the state, the super-script $\pm$ is used. The Σ states for which the electronic wave function is left unchanged upon this reflection are specified as Σ^+ and the states whose electronic wave function changes sign upon reflection are specified as Σ^-.

For a homo nuclear diatomic molecule, there is a center of symmetry about a point at the center of molecular axis. The electronic Hamiltonian is invariant under a reflection of the coordinate of all electrons with respect to this point. The states for which the electronic wave function is left unchanged by this reflection are labeled by Λ_g and the states whose electronic wave function changes sign upon this reflection are specified as Λ_u, where g and u stands for gerade and ungerade.

Hund's case (c)

When the internuclear distance is relatively larger, the spin-orbit interaction is stronger than the electric field along the inter nuclear axis. Hence $\vec{L}$ and $\vec{S}$ couples to form $\vec{j}$ and

the projection of $\vec{j}$ onto the internuclear axis, Ω is a good quantum number. The term H_{SO} is included in the Hamiltonian and the Schrodinger equation is solved to get the molecular states. The states are labeled as $\Omega^{\pm}_{g,u}$.

As the molecules dealt with in this thesis are long range in nature, the Hund's case (c) potentials are mostly used except for Rb_2 ground state, for which the orbital angular momentum is zero and hence there is no spin-orbit interaction and the experimentally deduced Hund's case (a) potentials are available for them. Certain selection rules apply to dipole allowed transition between the electronic states of the molecules. The angular momentum can change by a maximum of one unit: $\Delta\Omega = 0, \pm 1$. Also only u $\leftrightarrow$ g and + $\leftrightarrow$ + and - $\leftrightarrow$ - transitions are dipole allowed by symmetry considerations.

In the following, we describe the nuclear motion in bound and unbound electronic levels and explain the method to calculate the wave function. This is required to understand the molecule formation process by photo association and to find the final distribution of ro-vibrational levels by calculating the free to bound, bound to bound and bound to free transition rates from one state to another. It is also required to model interaction of electromagnetic light with state prepared ground state molecule as will be explained in chapter 5.

4.2.3 Nuclear Motion

The potential energy U(R) in the Schrodinger equation for nuclear motion Eq. 4.3, depends only on the relative distance of the two nuclei and hence the Schrodinger equation can be separated into two, (i) to describe the translational motion of the entire molecule and (ii) to describe the internal relative motion of the nuclei. The motion of the nuclei relative to each other in a diatomic molecule can be described by solving the Schrodinger equation

$$(\frac{-\hbar^2}{2\mu}\nabla^2 + U(R))\psi_n = E\psi_n \tag{4.4}$$

where $\mu = m_\alpha m_\beta/(m_\alpha + m_\beta)$ is the reduced mass of the system. This central force equation can be solved in spherical coordinate system with $\psi_n = \Psi_n(R)\ Y_l^m(\theta,\phi)$, where Y_l^m are the spherical harmonics and the radial part of the Schrodinger equation

can be shown to be

$$\frac{-\hbar^2}{2\mu}\Psi_n''(R) + [U(R) + \frac{l(l+1)\hbar^2}{2\mu R^2}]\Psi_n(R) = E\Psi_n(R) \tag{4.5}$$

This equation can be solved using Cooley-Numerov method or finite-element method.

Bound levels and wave functions

When the energy E is negative, the solutions of Eq. 4.5 are discrete bound wave functions and are calculated using the LEVEL code [27], which is based on Cooley- Numerov method. A brief description of the method is given in this section. The boundary conditions for the solution of Eq. 4.5 are $\Psi_n(R) \to 0$ for $R \to 0$ and $R \to \infty$. A grid of points is defined in space from R_{min} to R_{max}, both are well within the two classically forbidden region. In Cooley method, a trial energy E_n is guessed initially and Eq. 4.5 is solved by numerical integration, to get $\Psi_1(R)$ from R_{min} to R_{mid} and $\Psi_2(R)$ from R_{max} to R_{mid}, where R_{mid} is chosen to be in the classically allowed region. For a true wave function, $\Psi_1(R)$ and $\Psi_2(R)$ and their derivatives should be continuous at R_{mid}. An energy correction formula, which determines the new trial energy from the discontinuity of $\Psi_1(R)$ and $\Psi_2(R)$ and their derivative, is used to iteratively converge to the eigen energy. The corresponding wave functions are then normalized to unity.
The vibrational levels calculated for Rb_2 molecules are presented in section 4.4.3 and compared with experimental data in section 4.5.

Continuum wave functions

In this case, $E > 0$ and hence the wave function is not bound. For a given relative kinetic energy E above the asymptote, the continuum wave functions are calculated numerically using the Numerov method. Unlike bound wave function, the continuum wave function cannot be normalized to unity and needs to be energy normalized as will be discussed later.
The Numerov method is described below based on which a numerical code is developed. In this method, the coordinate space is divided into small intervals of length s,

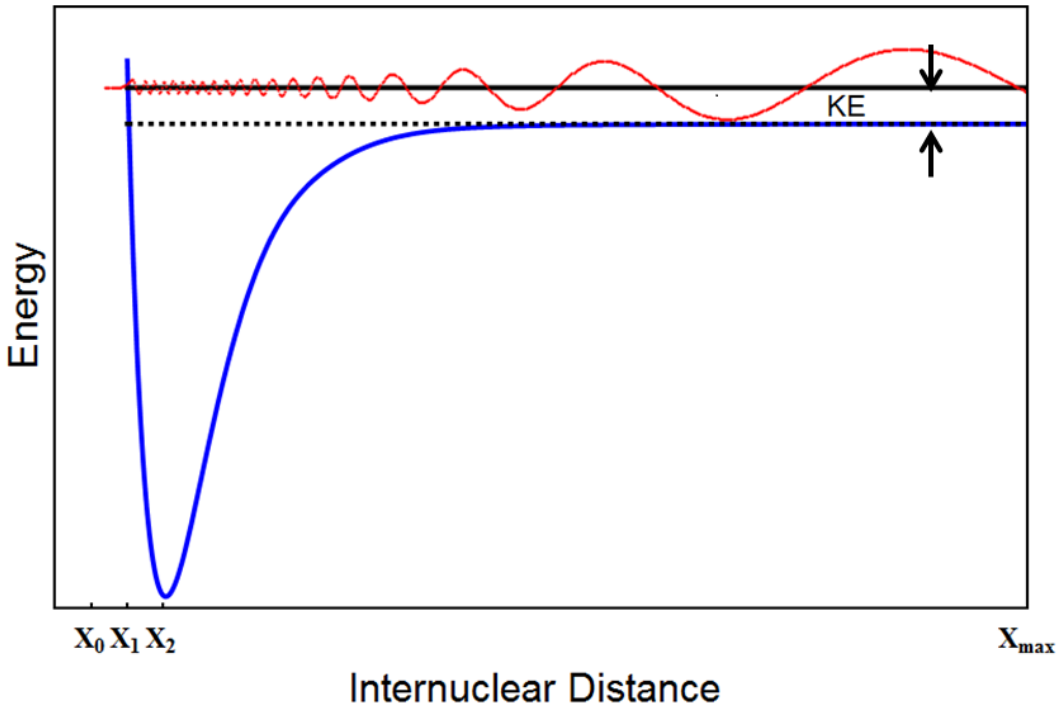

Figure 4.2: The schematic represents the Numerov method to solve the Schrodinger equation for nuclear motion. In this propagation method, at a given kinetic energy E above the asymptote, ψ_0 and ψ_1 are assigned values 0 and say 0.000001, where x_0 and x_1 are well within the classically forbidden region. The wave function at preceding points is calculated using Eq. 4.7.

from x_0 to x_{max} as shown in Fig. 4.2. The Schrodinger equation 4.5 gives $\psi^{''}(R)$ as

$$\begin{aligned} \psi^{''}(R) &= \frac{2\mu}{\hbar^2}(U_{eff} - E)\psi \\ &= G\psi \end{aligned} \tag{4.6}$$

where U_{eff} is the effective potential $U(R) + l(l+1)\hbar^2/2\mu R^2$ and $G = (2\mu/\hbar^2)(U_{eff} - E)$. Using a Taylor series expansion for ψ, arranging the terms and neglecting the terms with powers of s from s^6 as explained in detail in [93], we get the equation

$$\psi_{n+1} \approx \frac{2\psi_n - \psi_{n-1} + 5G_n\psi_n s^2/6 + G_{n-1}\psi_{n-1}s^2/12}{1 - G_{n+1}s^2/12} \tag{4.7}$$

For a kinetic energy E above the asymptote, Eq. 4.7 can be used to calculate the wave function at the point x_{n+1} (ψ_{n+1}) , knowing the values of ψ at the preceding points x_n and x_{n-1} (ψ_n and ψ_{n-1}). The point x_0 is chosen such that it is well within the classically forbidden region on the left of the inner turning point of the PEC and hence the value

of the wave function can be approximated to zero. The value of the ψ at $x_0 + s$, ψ_1, is taken to be a small number, for example 0.000001. The wave function at the point n+1, ψ_{n+1}, is then calculated using Eq. 4.7.

Choosing a value for ψ_1 is trivial. If ψ_1 was chosen to be one order of magnitude higher, the only change will be that the value of ψ in the subsequent points would be multiplied by 10. However since the wave function amplitude is going to be unit normalized before the energy normalization, as explained in the following section, eventually the wave function is independent of the choice of ψ_1 .

The continuum wave functions calculated for Rb_2 molecule are explained in section 4.4.2. The numerical code developed to calculate the continuum wave function is documented in Appendix C.

Normalization of the continuum wave function

When the value of E is greater than zero, in the asymptotic limit Eq. 4.5 takes the form $\Psi''(R) = \frac{-2\mu E}{\hbar^2}\Psi(R)$ and the solution $\Psi(R) \rightarrow A * Cos(\frac{\sqrt{-2\mu E}}{\hbar}R)$. This solution $\Psi(R)$ is not square integrable and a normalization condition as in the case of bound wave function is not applicable. Considering the constant A to be unity, the scalar product of two continuum wave functions $\Psi_\epsilon(R)$ and $\Psi_{\epsilon'}(R)$, can be written as proportional to a Dirac delta function.

$$\int_0^\infty \Psi_\epsilon(R) * \Psi_{\epsilon'}(R) dR = \delta(\epsilon - \epsilon'). \tag{4.8}$$

The wave function is then energy normalized and the normalization constant is $\frac{1}{(\pi\hbar)^{1/2}}(\frac{2\mu}{E})^{1/4}$ [94, 95]. To energy normalize the continuum wave function found using Numerov method, first the wave function amplitude is made unity at a distance where the function is sinusoidal and then multiplied with the normalization constant. For energies very close to zero, the continuum wave function becomes sinusoidal only at very large values of R and hence has to be calculated for very long range of R (R $>$ 1000 Å) to unit normalize to the cosine amplitude. For higher kinetic energies, the wave function approaches the sinusoidal form at lower value of R and has to be calculated

only till few hundreds of Å. The continuum wave function has dimensions of $E^{-1/2}$, as indicated by the Eq. 4.8 [94].

Franck-Condon overlap

The Franck-Condon factor of a ro-vibrational level in upper electronic state, $|v', J'\rangle$ and that in lower electronic state, $|v'', J''\rangle$ is give by $|\langle v', J' | v'', J''\rangle|^2$. This overlap integral estimates the relative intensities in absorption and emission processes for the same electronic states. Given the transition dipole moment between the electronic states, Einstein's A and B coefficients which gives the spontaneous emission rate and stimulated absorption/emission rate respectively can be calculated.

4.3 Cold and ultra-cold molecules

Studies with ultra cold molecules are rapidly increasing in numbers and several techniques have been developed in the last few decades to produce and trap cold molecules. The most prevalent technique to produce ultra-cold molecules is photo association and is described in this section.

4.3.1 Photo association

Photo association (PA) is a light assisted free to bound association of a pair of colliding atoms. PA is a widely used method for producing both homo nuclear and hetero nuclear ultra-cold molecules [51, 54]. Soon after the developments leading to the cooling and trapping of alkali atoms, the PA of cold atoms was proposed and several experimental groups immediately applied the technique to get high resolution spectra in alkali dimers [52, 53, 96–98].

In photo association, two atoms with relative kinetic energy ϵ absorb a photon of energy $\hbar\omega$ and create a bound molecule in a ro-vibrational level in an excited electronic state. This results in a loss of atoms in the trap whenever $\hbar\omega + \epsilon = E_{v,J}$, where $E_{v,J}$ is the energy of the excited state ro-vibrational level with respect to the ground contin-

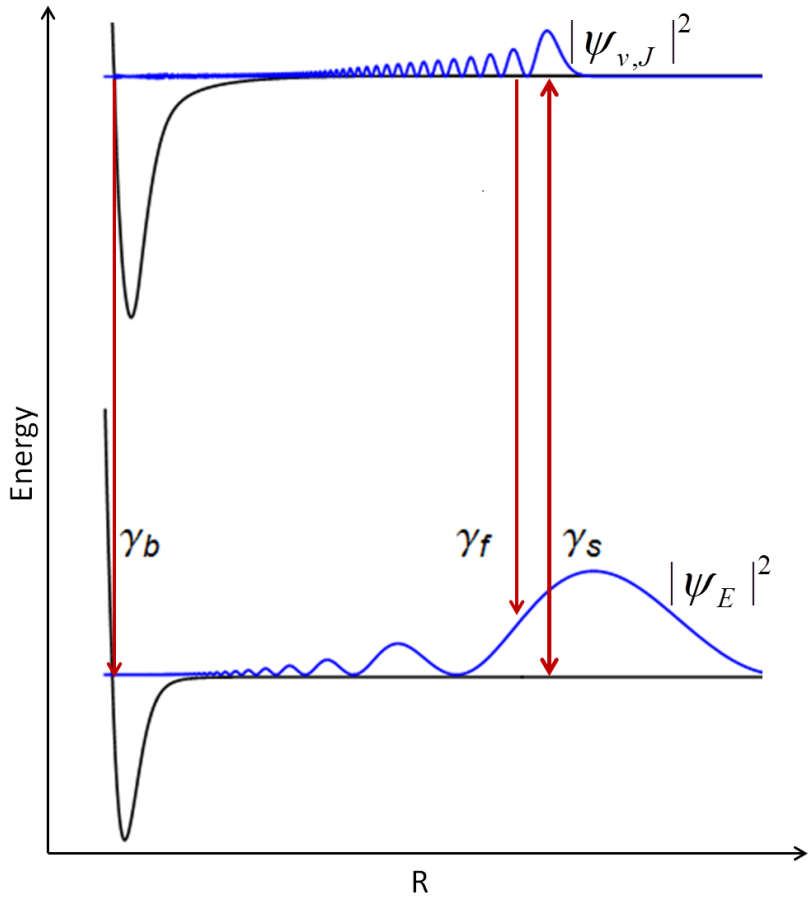

Figure 4.3: A schematic representation of the photo association process is shown in the figure. The modulus square of the excited vibrational and ground collisional wave functions is plotted. When the collision energy of the atoms plus the photon energy matches with a vibrational energy of the excited electronic state with a good overlap of the wave functions, free to bound transition occurs. The excited state molecules subsequently spontaneously de-excite to the ground electronic state either to bound vibrational levels or to two separate atoms in the continuum with rates γ_b and γ_f respectively.

uum. A fraction of excited molecules de-excite to the bound levels in ground electronic state (with spontaneous emission rate, γ_b) and the remaining de-excite to form a pair of free atoms (with spontaneous emission rate, γ_f). The entire process in represented in Fig. 4.3, where γ_s is the rate of stimulated transition. Thus, scanning a tunable PA laser results in high resolution free-bound spectra, and can provide information regarding the long range properties of electronic potential energy curves.

There are several features which makes photo association interesting. It is a very efficient method to produce long range molecules. The molecules formed by photo association are inherently translationally cold and hence easy to load into a dipole trap. Photo association spectra in cold atoms gives narrow resonances which corresponds to excited state vibrational levels. By analyzing the PA spectra, excited state C_3 coefficients for homo nuclear and C_6 coefficients for hetero nuclear molecules, ground state collisional scattering length etc. can be deduced.

4.4 The Rb_2 molecule

We adopt photo association method to produce neutral molecules in our experiments. Cold Rb_2 molecules are created at the center of the hybrid trap, using an additional PA laser as described in section 4.5.1. The energy levels relevant for photo association of Rb_2 molecule are the subject of this section.

4.4.1 Electronic levels

The PECs, with asymptotic energy corresponding to $5S_{1/2} + 5S_{1/2}$, $5S_{1/2} + 5P_{1/2}$ and $5S_{1/2} + 5P_{3/2}$ are given in Table 4.1 and plotted in Fig. 4.4. Here, the number in brackets in front of the energy level notation is the chronological order of the energy levels having the same notation. The ab initio potential energy curves and transition dipole moments for Rb_2 molecule till $R = 26$ Å is given up to the state $5S + 4D$ in A. R. Allouche et.al. [24]. The pure long range state $(2)0_g^-$ is tabulated up to $R = 82$ Å in B. Bussery et.al. [25].

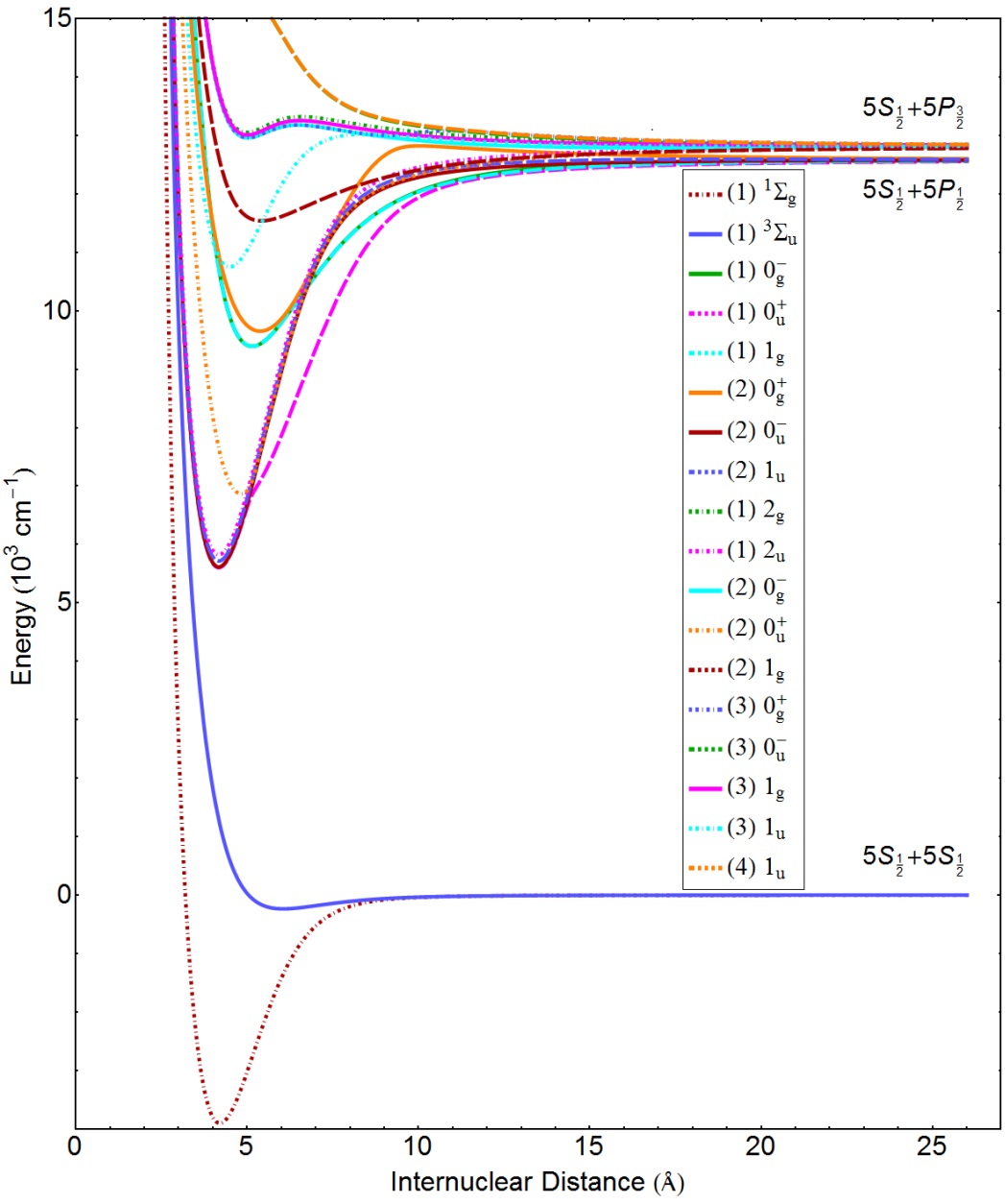

Figure 4.4: The figure shows the electronic energy levels of Rb_2 molecules with asymptote corresponding to $5S_{1/2} + 5S_{1/2}$, $5S_{1/2} + 5P_{1/2}$ and $5S_{1/2} + 5P_{3/2}$. The levels are tabulated in Table. 4.1.

Table 4.1: The electronic energy levels of Rb_2 molecule with asymptote corresponding to $5S_{1/2}+5S_{1/2}$, $5S_{1/2}+5P_{1/2}$ and $5S_{1/2}+5P_{3/2}$ are tabulated.

$5S_{1/2}+5S_{1/2}$	$5S_{1/2}+5P_{1/2}$	$5S_{1/2}+5P_{3/2}$
$(1)^1\Sigma_g^+$	$(1)0_g^-$	$(1)2_g$
$(1)^3\Sigma_u^+$	$(1)0_u^+$	$(1)2_u$
	$(1)1_g$	$(2)0_g^-$
	$(2)0_g^+$	$(2)0_u^+$
	$(2)0_u^-$	$(2)1_g$
	$(2)1_u$	$(3)0_g^+$
		$(3)0_u^-$
		$(3)1_g$
		$(3)1_u$
		$(4)1_u$

The ground state, $5S_{1/2}+5S_{1/2}$, has zero orbital angular momentum and hence there is no spin-orbit interaction. In this case, the Hund's case (a) potentials, $^1\Sigma_g^+$ and $^3\Sigma_u^+$, are considered. These potentials are generated using the data and fitting parameters obtained from C. Amiot et.al. [26] and B. Beser et.al. [99] respectively. As these PECs are derived from experimental data, they are considered to be more accurate than the ab initio potentials. The long range part of the molecular potential can be expanded in terms of multi-poles and is valid beyond the range where the short range interactions due to charge overlap is small compared to the long range interactions due to electrostatic and dispersion forces. The lower bound of the region of validity for the multi-pole expansion is called Le Roy radius (R >20 Å for Rb_2) [100]. The asymptotic part of the Rb_2 ground state potential is C_6/R^6 in nature and both the ground states have the same dispersion coefficient C_6. The experimentally derived value of $C_6 = 4550$ a.u. is obtained from Boesten et.al. [101] and is used to fit the asymptotic part of the potential.

For two atoms one in the ground and the other in the excited state which are related

by a dipole allowed transition, the interaction is due to dipole-dipole force and hence the potential is C_3/R^3 in nature at long range. The photo association of Rb_2 molecules both for the D1 and D2 transitions are studied by various groups [53, 96, 102] and the resulting spectra have been used to deduce the C_3 coefficients. For $(2)0_g^-$, the PEC in [25] is used and for the remaining levels, the PECs in [24] are used with long range regime fitted with C_3 coefficient derived from the experiment [53]. From these sources we get the values of the C_3 coefficients as $C_3[(2)0_u^+] = 14.64$ a.u. and $C_3[(2)1_g] = 14.29$ a.u.

In long range photo association on the D2 transition, given the selection rules, three electronic energy levels can be addressed and are observed in experiments [53]. These energy levels are $(2)0_g^-$, $(2)0_u^+$ and $(2)1_g$, of which $(2)0_g^-$ is a double well potential with the second well being purely long range. These three levels and the ground states are shown in Fig. 4.5. The PECs obtained from different sources differ in energy and space units with different zero reference for the energy. All the PECs are converted into cm^{-1} versus Å with asymptotic energy of the ground state referred to zero.

4.4.2 Ground state continuum wave functions

In photo association, two colliding atoms absorb a photon to form a bound molecule in the excited electronic state. The effective potential for the collision is given by $V_{eff} = V(r) + \frac{l(l+1)\hbar^2}{2\mu r^2}$, where l is the relative angular momentum of the colliding atoms. In scattering theory, $l = 0$, 1, 2, 3,.. are referred as s, p, d, f,.. partial waves. Fig. 4.6 shows the effective potential of Rb_2 ground state for $l = 0$, 1, 2, 3 and 4 and the corresponding collisional wave functions at an energy equivalent to a temperature of 1 mK above the asymptote.

The continuum wave functions are calculated using the Numerov method discussed in the section 4.2.3. For a given kinetic energy, E above the asymptote, the Schrodinger equation 4.5 is solved numerically. The calculations are performed with spatial interval $s = 0.001$ Å which gives sufficient number of wave function points between nodes. As r$\rightarrow \infty$, the wave function becomes sinusoidal. The Fig. 4.7 shows the continuum

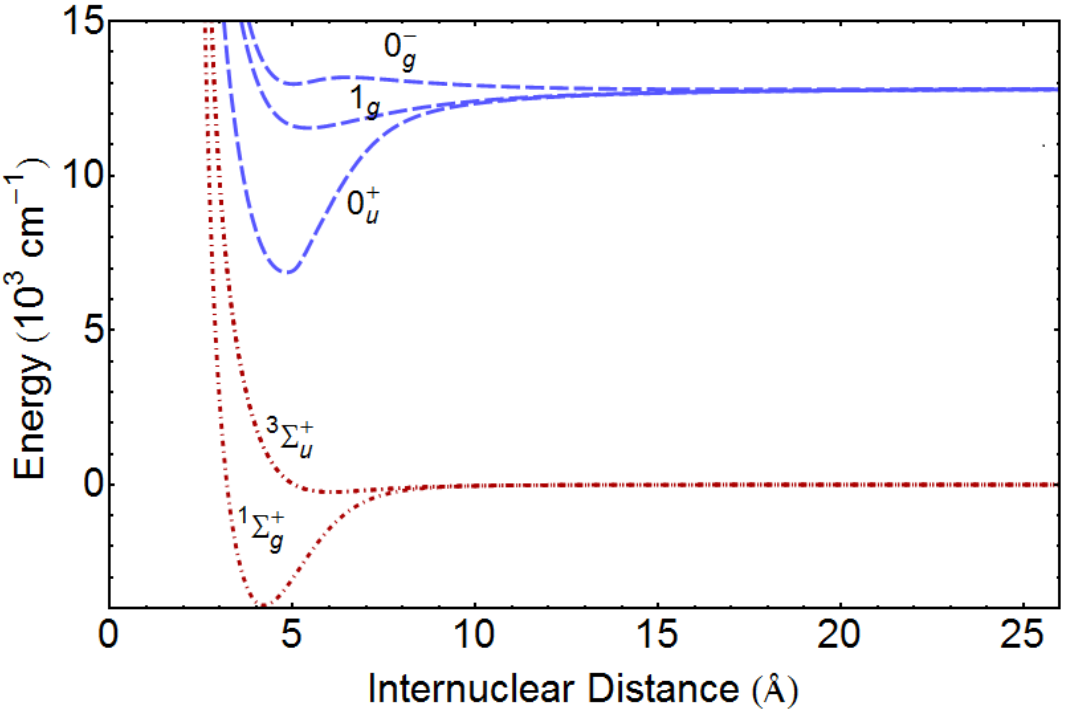

Figure 4.5: The PECs relevant for the experiment are shown in the figure. The photo association is performed in D2 transition approximately 2 cm^{-1} below the asymptote.

wave function in Rb_2 ground state at a collisional energy corresponding to $T = 100$ μK, 1000 μK, 2 mK and 10 mK above the asymptote. The inter nuclear distance beyond which the wave function behaves sinusoidally, decreases with increasing collision energy. At very low collision energies ($< \mu$K), the wave function has to be calculated up to micrometers to observe the sinusoidal behaviour. Fig.4.8 shows the wave function up to 6000 Å at a collision energy corresponding to 1 μK.

In long range photo association, (few cm^{-1} below the excited state asymptote), the associated molecules in the excited electronic state decay back to the ground state, mostly as two separate atoms. This happens over a wide range of relative kinetic energies between the two atoms. In order to obtain the total decay rate back to the free state, the spontaneous rate is calculated to each continuum levels in small intervals and then integrated over energy. This is presented in section 4.4.4, where the branching ratio of spontaneous transition rate from excited vibrational state to bound and unbound levels in ground state is explained.

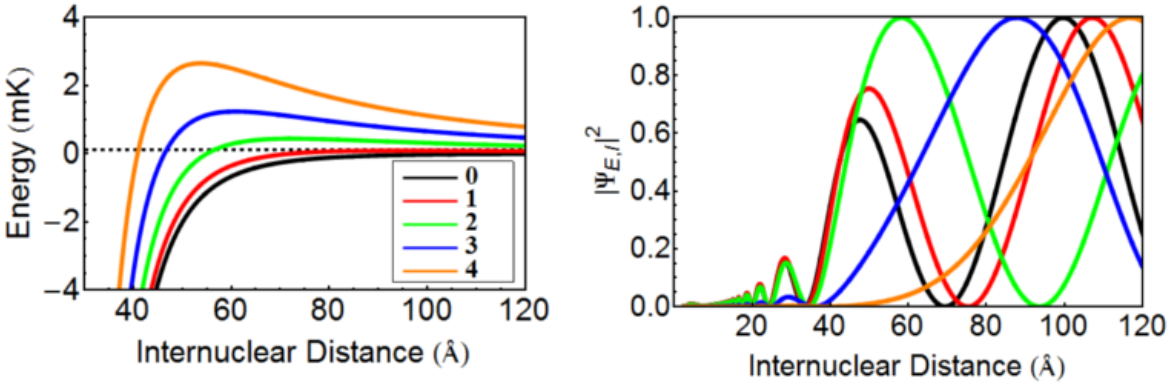

Figure 4.6: (a) shows the effective potential of Rb_2 ground state for relative angular momentum of the atoms, $l = 0, 1, 2, 3$ and 4. The value of l corresponding to the different lines is as given in the inset. The measured temperature of Rb atoms in our MOT, 107.7 μK is represented by the horizontal dashed line. (b) The modulus square of collisional wave function in each effective potential at an energy equivalent to a temperature of 1 mK above the asymptote, calculated using Numerov method is plotted.

4.4.3 Vibrational levels of Rb_2 molecule

The vibrational levels and wave functions for all the relevant states are calculated using LEVEL code. A radial mesh size of dx= 0.001 Å is used for the numerical solution to ensure at least ≈20 points between the two adjacent nodes at the highest frequency. The wave functions for the vibrational levels v =0, 50, 100 and 200 for the (2) 0_u^+ potential are illustrated in the Fig. 4.9. The calculated levels are compared with experimental data in section 4.5.

4.4.4 Branching ratio

When studying molecule light interactions, usually it is desirable to know the distribution of final states to which an excited molecule decays. The spontaneous emission rate from a vibrational level v' of excited electronic state to the bound vibrational level v of the ground electronic state, ($\gamma_{v'v}$) and free levels with energy E above the asymp-

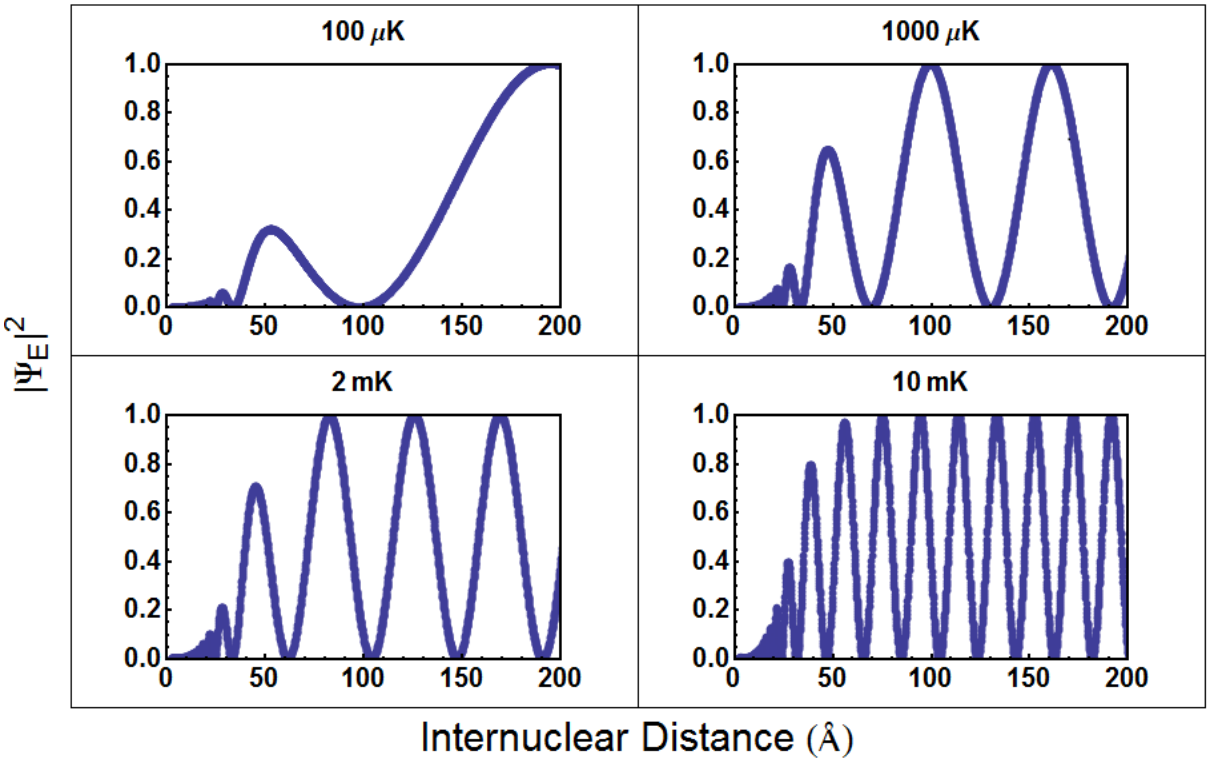

Figure 4.7: The modulus square of collisional wave function in Rb_2 ground electronic state, calculated using Numerov method at different collision energies corresponding to $T = 100$ μK, 1000 μK, 2 mK and 10 mK are shown. At higher collisional energies, the sinusoidal nature of wave function appears at a shorter inter nuclear distance.

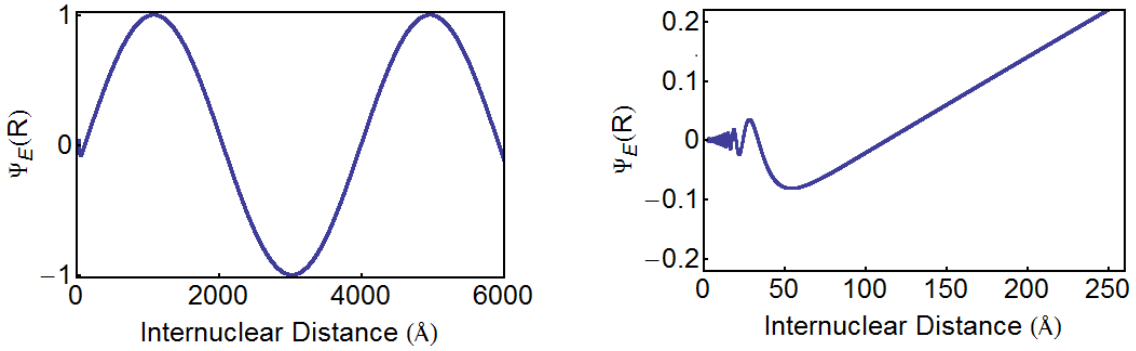

Figure 4.8: The collisional wave function in the Rb_2 ground electronic state at the relative kinetic energy between the atoms corresponding to 1 μK is shown. The wave function is calculated using Numerov method. The left panel shows the wave function up to 6000 A^0 and in the right panel the wave function in short range is plotted.

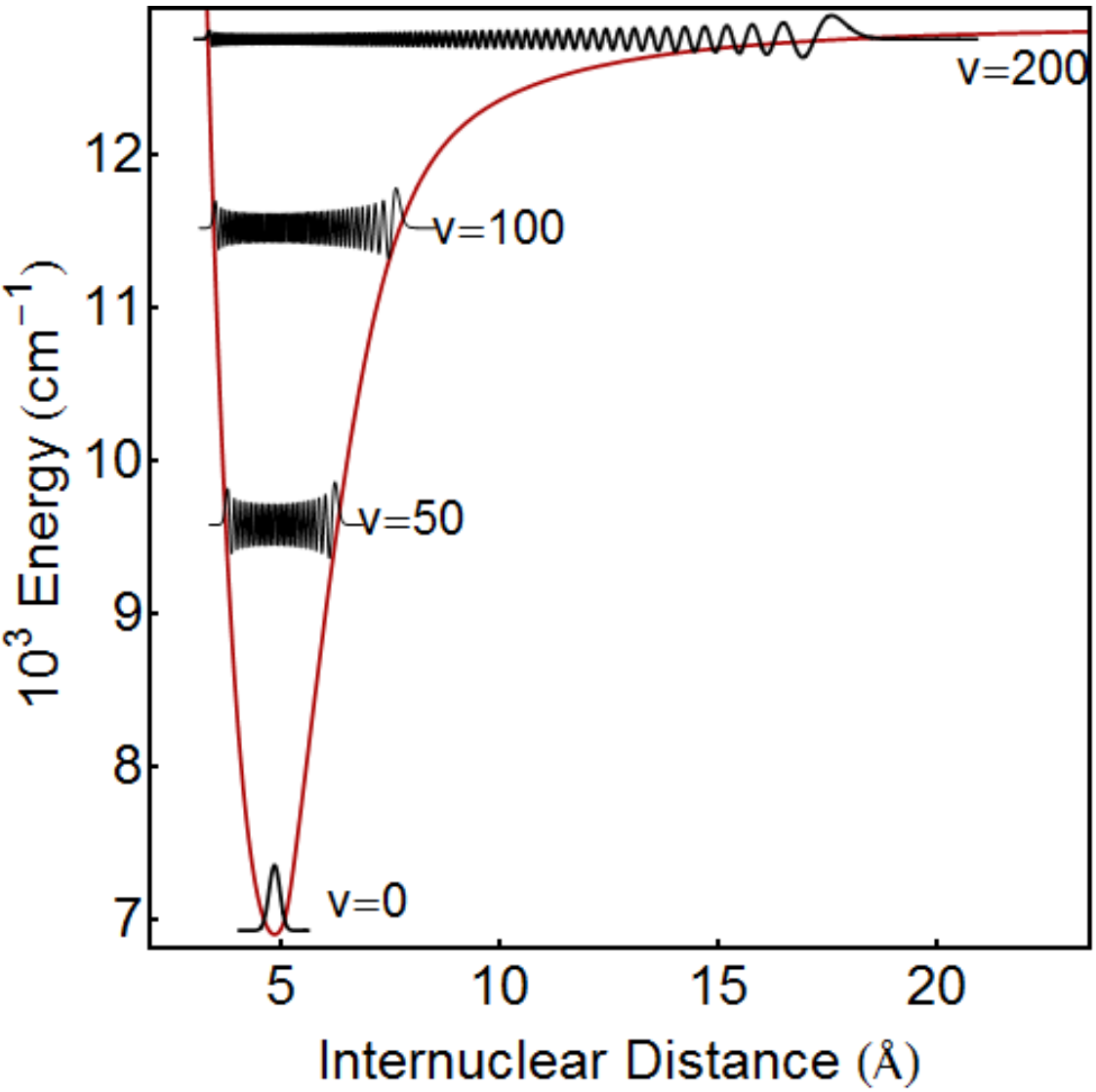

Figure 4.9: The bound state wave functions for v =0, 50, 100 and 200 levels of Rb_2 molecule in the $(2)0_u^+$ electronic state, calculated using LEVEL code.

totic energy in the ground state, ($\gamma_{v'E}$) depends on the Franck-Condon overlap of their corresponding wave functions. The expression, $f_b = \gamma_b/(\gamma_t)$ gives the percentage of molecules de-excite back to the bound state. Here,

$$\gamma_b = \sum_v \gamma_{v'v} = \sum_v \frac{1}{3\pi\epsilon_0 c^3}\omega_{ab}^3 \left|\langle\psi_v|d(R)|\psi_{v'}\rangle\right|^2$$
$$\gamma_f = \int_E \gamma_{v'E} dE = \int_E \frac{1}{3\pi\epsilon_0 c^3}\omega_{ab}^3 \left|\langle\psi_E|d(R)|\psi_{v'}\rangle\right|^2 dE$$
$$\gamma_t = \gamma_b + \gamma_f \tag{4.9}$$

Fig. 4.10 and 4.11 shows the distribution of final ground vibrational states v in $(1)^1\Sigma_g$

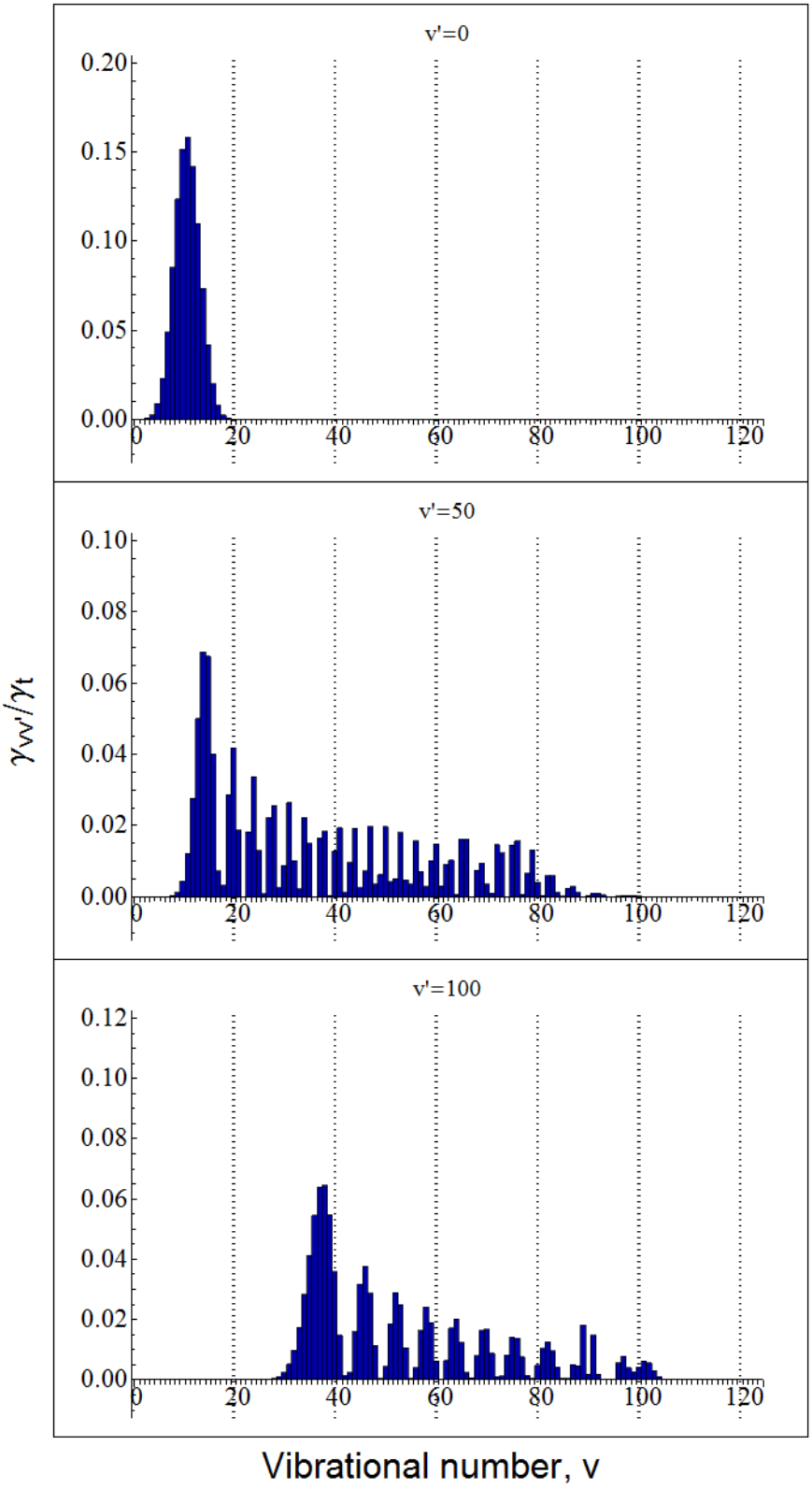

Figure 4.10: Distribution of vibrational states v in (1) $^1\Sigma_g$ electronic ground state, when de-excited from vibrational states v' from (2) 0_u is shown for $v' = 0$, 50 and 100. The spontaneous decay rate is a function of Franck-Condon overlap between the wave functions of the levels v and v'.

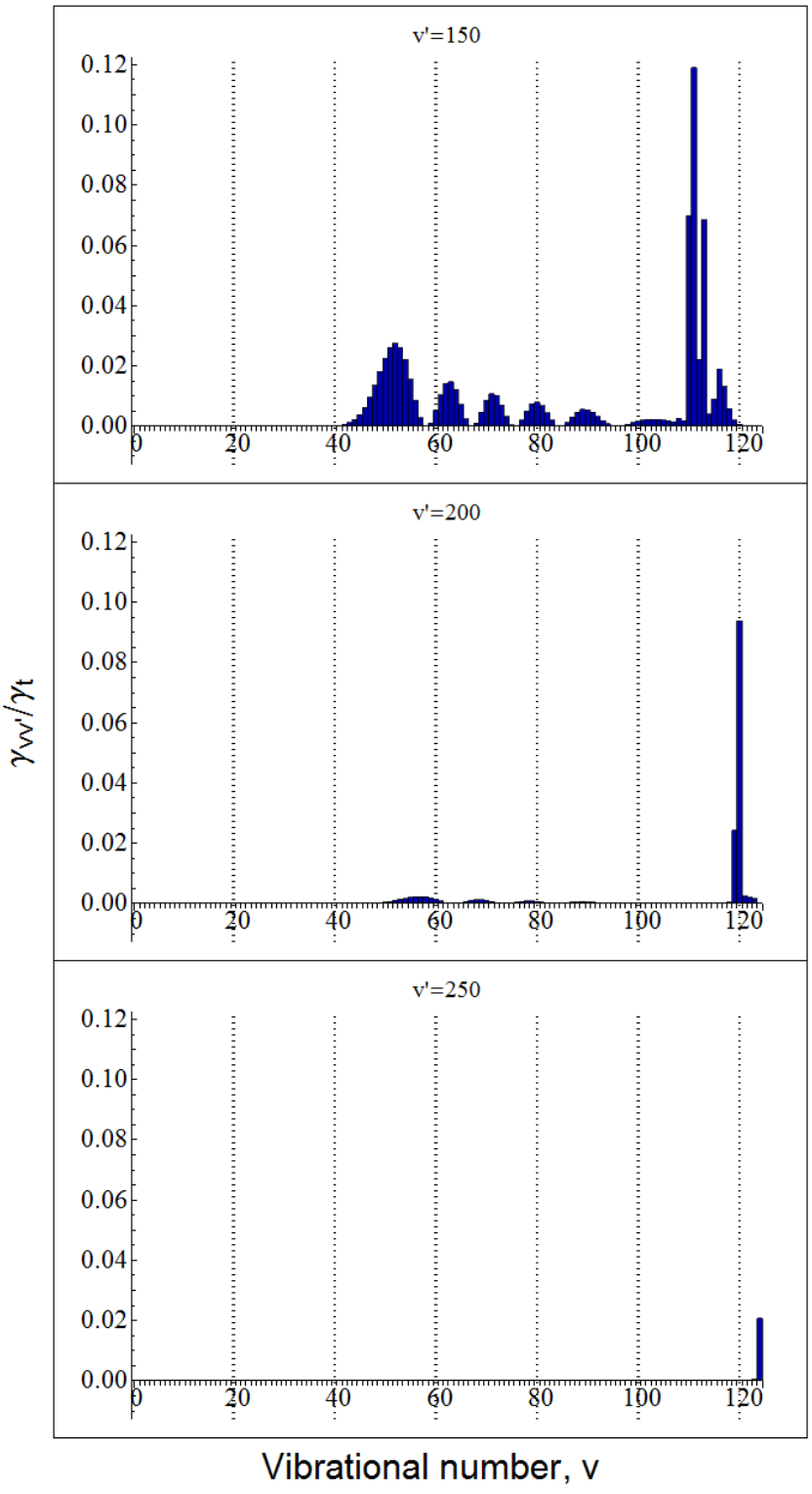

Figure 4.11: Distribution of vibrational states v in (1) $^1\Sigma_g$ electronic ground state, when de-excited from vibrational states v' from (2) 0_u is shown for $v' = 150$, 200 and 250. The excited vibrational level v'=250 is approximately 2 cm^{-1} below the atomic asymptote.

when de-excited from different excited vibrational states v' in $(2)0_u^+$. The branching ratios f_b and $1 - f_b$ are tabulated for the same transitions in Table. 5.1. This shows that for a long range excited molecule, the spontaneous emission rate is higher to the free atom state. The numerical code for the calculation of rates is added in Appendix C.

Table 4.2: The branching ratios f_b and $1 - f_b$ for transitions from few excited vibrational levels v' in $(2)0_u^+$ to the ground state $(1)^1\Sigma_g$

v'	f_b	$1 - f_b$
0	1.0	0.0
50	0.9997	0.0003
100	0.9691	0.0309
150	0.7444	0.02556
200	0.16	0.84
250	0.0221	0.9779

4.5 Molecular spectrum of Rb_2

In our experiment we produced long range Rb_2 molecules by photo association, in several vibrational levels of $(2)0_u^+$, $(2)1_g$ and $(2)0_g^-$ excited electronic states. The molecules formed can be detected using two methods. One is the MOT trap loss method, where the loss in atom fluorescence is a measure of molecule formation in the excited state due to the loss of pairs of atoms from the MOT in the formation of each molecule. As the PA laser is scanned over the vibrational resonances, dips can be observed in the MOT fluorescence signal as shown in Fig. 4.13. The second method is a direct, but destructive measurement. In this method, the molecules formed in the ground state by de-excitation of the associated molecules are detected. The Rb_2 molecules are ionized using high energy laser pulses by resonance enhanced multi photon ionization (REMPI) process, to form Rb_2^+ molecular ions in their electronic ground state. The Rb_2^+ ions are then detected using channel electron multiplier (CEM) by time of flight

method.

In this section, the photo association experimental setup, trap loss measurement and identification of vibrational levels are presented. REMPI is demonstrated and described in detail in chapter 5 and is used as a method to produce Rb_2^+ molecular ions for performing further experiments.

4.5.1 Experimental arrangement

Laser system

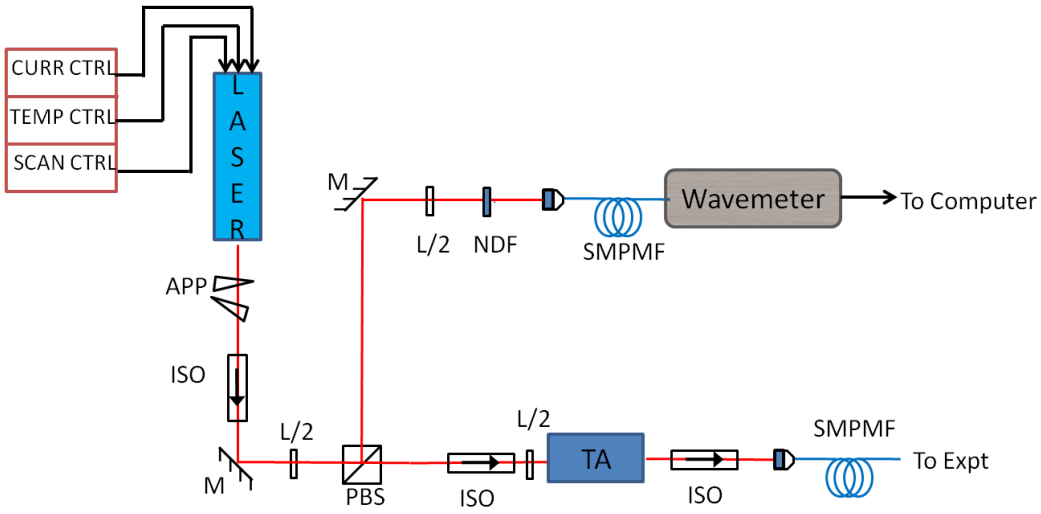

Figure 4.12: Figure shows the schematic of the laser (ECDL) setup for photo association. The laser frequency is scanned by modulating the voltage applied on the piezo electric transducer of the ECDL and monitored using a wave meter. A part of the laser beam is amplified using a tapered amplifier and fed to the experiment using a single mode fiber.

We use a home built ECDL with Thorlabs:DL7140 laser diode as the photo association laser. The laser diode current and temperature are controlled by using a Toptica Photonics DC110. The laser output is divided into two parts. A small fraction of light is fed to a wave meter (HighFinesse: WS/6) to monitor the frequency of the laser beam, which is used for experimental determination of the frequencies of the molecular resonance. The major part of the laser beam is injected to a tapered amplifier (Toptica-BOOSTA) for amplifying the power to $\sim$ 1 W. The output of BOOSTA is coupled to

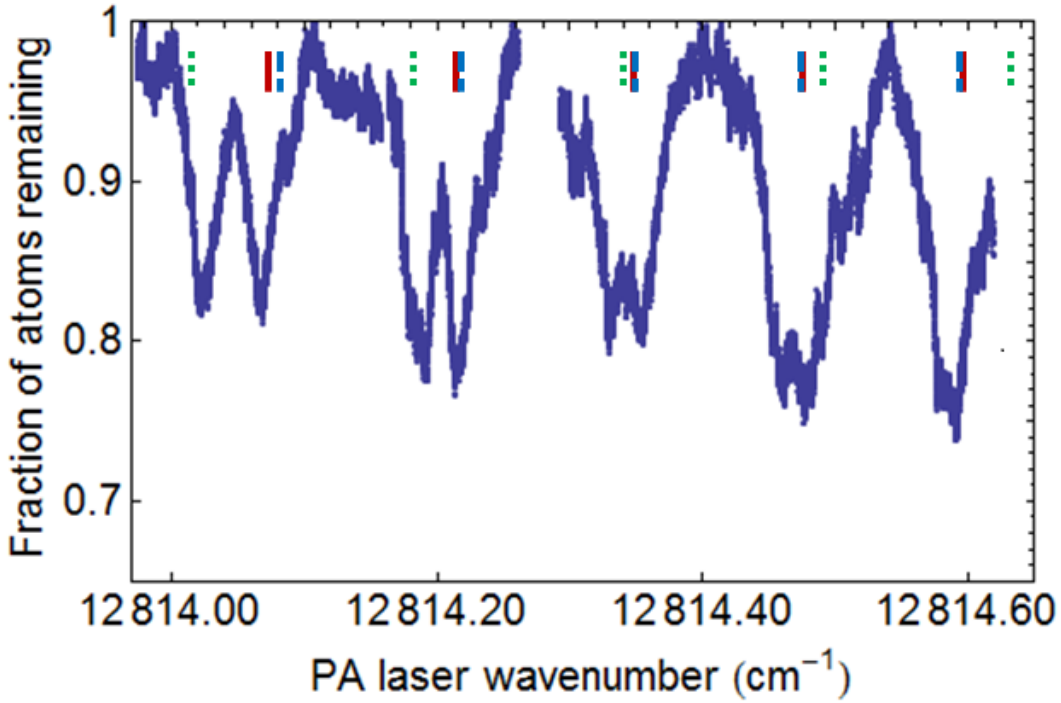

Figure 4.13: The photo association of Rb_2 molecule in D_2 transition is shown. The peaks corresponds to the formation of excited state molecules in the vibrational distribution of $(2)0_u^+$ (v= 249 to 253), $(2)0_g^-$ (v= 48 to 52) and $(2)1_g$ (v= 162 to 166) levels are indicated by dashed blue, dotted green and thick red lines respectively. The spectrum is taken 2 cm^{-1} below the asymptote.

a single mode polarization maintaining fiber (SMPMF) to transport the beam to the experimental table. The beam is then focused on the MOT using a lens of focal length 200 mm. The focusing helps in achieving high peak intensities. In addition, focusing reduces the scattering of the light from the Tungsten wire mesh for the ion trap, hence reducing the background noise in the MOT fluorescence.

The laser is red detuned approximately 2 cm^{-1} from the $5S_{1/2} + 5P_{3/2}$ atomic asymptote. A slow scan voltage is applied to the piezo electric transducer to scan the laser frequency at a rate $\sim$ 35 MHz/s. The photo association spectrum from 12814 cm^{-1} to 12814.6 cm^{-1} is shown in Fig.4.13. The molecular vibrational levels corresponding to the dips are identified and marked in the spectrum. The vibrational levels corresponding to the electronic potential $(2)0_u^+$ (v= 249 to 253), those corresponding to $(2)0_g^-$ (v= 48 to 52) and to $(2)1_g$ (v= 162 to 166) are represented by dashed blue, dotted green and

thick red lines respectively. The depth of the ab initio potentials of the excited state is adjusted slightly to match the observed spacing between levels in the experiment.
The molecules produced via photo association are inherently translationally cold, as they are directly produced from cold atoms. However, if the molecules are not trapped, they escape the MOT volume in few milli seconds. Since the molecules are cold and produced at the center of the hybrid trap, they can be easily loaded to a dipole trap formed by the cavity standing wave, using a far off resonance red detuned light. Moreover, the fact that large intensity of light can be built up in the cavity mode makes cavity mediated photo association interesting. This is a future perspective on the present experiments.

4.6 The Rb_2^+ molecule

4.6.1 Electronic levels

Table 4.3: The potential energy levels of Rb_2^+ molecule with asymptote corresponding to $5S_{1/2} + Rb^+$, $5P_{1/2} + Rb^+$ and $5P_{3/2} + Rb^+$ are tabulated.

$5S_{1/2} + Rb^+$	$5P_{1/2} + Rb^+$	$5P_{3/2} + Rb^+$
$(1)1/2_g$	$(2)1/2_g$	$(3)1/2_g$
$(1)1/2_u$	$(2)1/2_u$	$(3)1/2_u$
		$(1)3/2_g$
		$(1)3/2_u$

The Rb_2^+ molecule is a one active electron molecule and hence the total angular momentum is half integers. The multiplicity of the levels is $2S + 1 = 2$. The electronic energy levels up to $5P_{3/2} + Rb^+$ state are relevant for our experiments and are tabulated in Table 4.3 and plotted in Fig.4.14. For Rb_2^+ molecule, both the ground and excited state varies as C_4/R^4 asymptotically. The potential energy levels and transi-

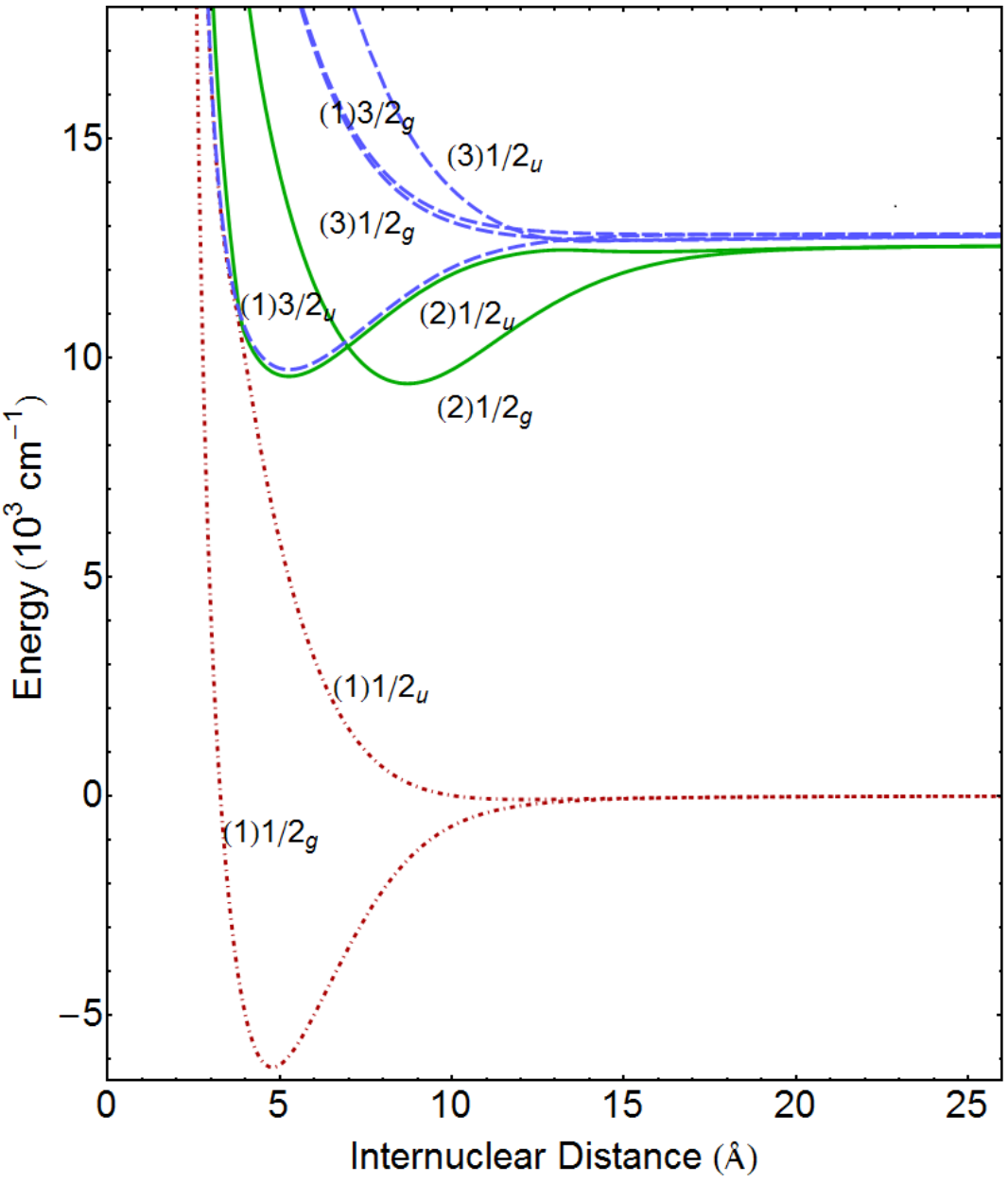

Figure 4.14: The ground and first excited electronic energy levels for Rb_2^+ molecule are shown. The red dot dashed, green line and blue dashed lines correspond to PEC with asymptote $5S_{1/2} + Rb^+$, $5P_{1/2} + Rb^+$ and $5P_{3/2} + Rb^+$ respectively. The levels are tabulated in Table. 4.3

tion dipole moments for the molecule are obtained from A. Jraij et.al. [103] up to $R =$ 42.33 Å. Unlike in case of neutral alkali dimers, experimentally derived potentials are not available for theirs cations. For calculations, we have used the potentials up to $R =$86.26 Å provided by Prof. Allouche in a private communication.

In the experiments presented in the thesis, the Rb_2^+ molecules are produced from the Rb_2 molecules, photo associated by the cooling laser light in the MOT, by two photon ionization using a pulsed dye laser. The production, optimum trapping parameters in the ion trap and the stability when held with MOT will be explained in detail in the chapter 5.

The bound and unbound wave functions are calculated for all the states of Rb_2^+ molecule and are used in chapter 5 for rate calculations to explain the possibilities for the instability of the molecular ions in presence of MOT light field.

4.7 Conclusion

The methods for numerical calculation of the energy levels, wave functions and rates are explained in detail. The cold Rb_2 molecule production via photo association is demonstrated and the observed vibrational levels are compared with the calculations. The PECs involved in the study of Rb_2^+ molecules are also presented.

CHAPTER 5

Stability of Rb_2^+ ions in the hybrid trap

5.1 Introduction

In this chapter, we first describe the Rb_2^+ production from Rb_2 molecules produced in the MOT. We then explain the optimization of trapping of Rb_2^+ ions in the ion trap. The experiments performed to study the stability of Rb_2^+ ions co-trapped with the MOT are described. We show that the Rb_2^+ ion number decays rapidly in the presence of the Rb MOT. In addition, we confirm that it is not the collision with the MOT atoms, but the trapping light field is the principle cause of the fast decay. With the help of the potential energy curves of Rb_2^+ molecule associated with the accessible transitions using the cooling light for the MOT, we have performed a comprehensive analysis of the possible molecular ion dissociation channels which are presented at the end of this chapter.

5.2 Creation of Rb_2^+ ions

The creation of Rb_2^+ ions results from a sequence of three steps as follows.

$$\begin{aligned} Rb + Rb + h\nu_{pa} &\rightarrow Rb_2^* \\ Rb_2^* &\rightarrow Rb_2 + h\nu \\ (or &\rightarrow Rb + Rb + h\nu) \\ Rb_2 + 2h\nu_i &\rightarrow Rb_2^+ + e^- \end{aligned} \tag{5.1}$$

In the first step two Rb atoms in the ground state are photo associated to an excited bound electronic state by a photon ($h\nu_{pa} = 12816.54$ cm^{-1}). These excited molecules decay spontaneously either to a bound molecule in the ground state or to two free atoms by emitting a photon. The third step is a two photon ($2h\nu_i = 33190.6$ cm^{-1})

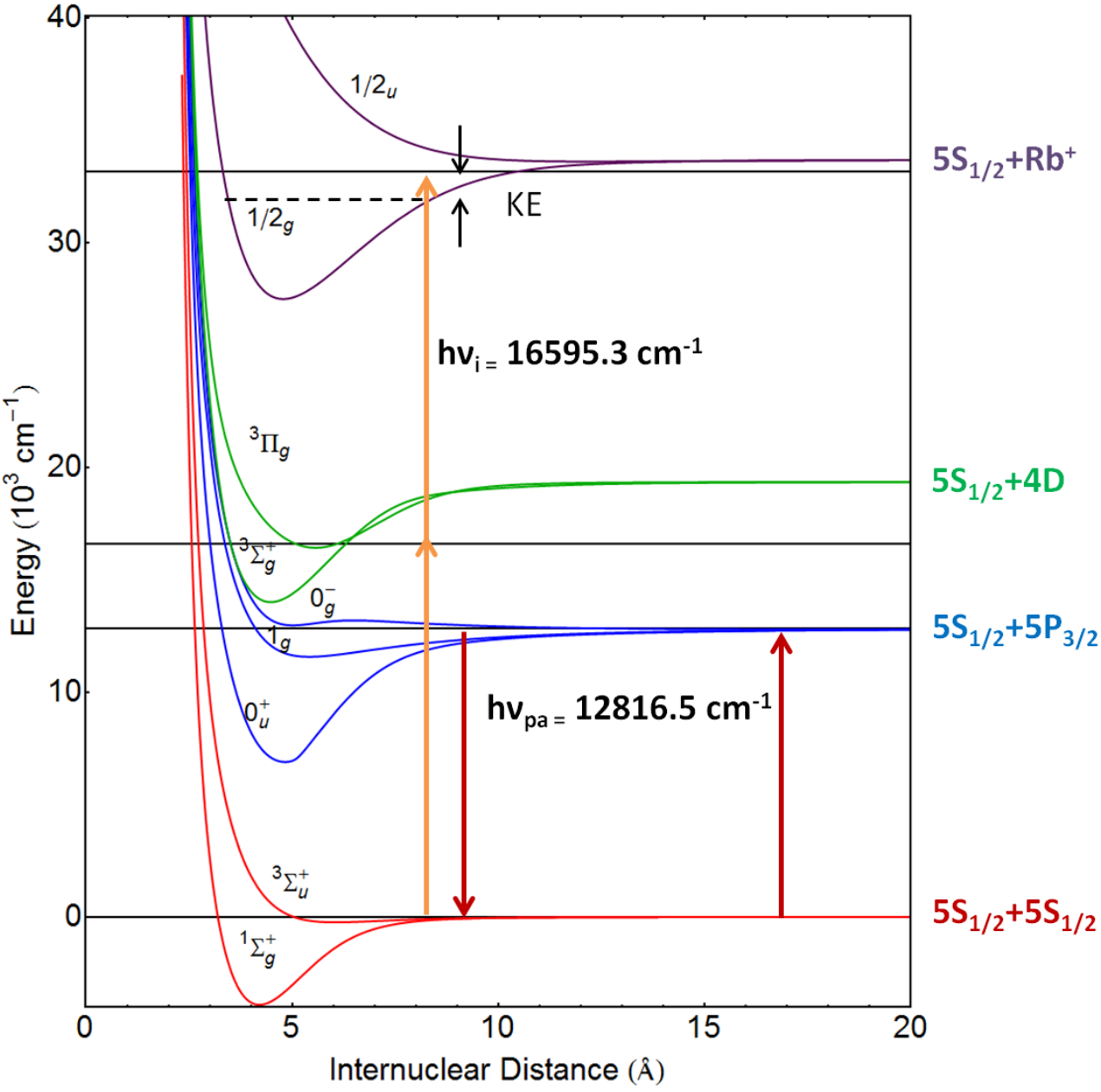

Figure 5.1: The potential energy curves of Rb_2 and Rb_2^+ molecules associated with the production of Rb_2^+ ground state molecular ions is shown in the figure. The asymptote corresponding to each PEC is marked. Rb_2 molecules are formed by absorbing the 12816.546 cm^{-1} photons followed by the spontaneous emission to a bound ground electronic state (red arrows), and the ground state molecules are ionized using two photons of 16595.3 cm^{-1} (orange arrows) to form Rb_2^+ molecules. The post ionization kinetic energy (KE) of the electron ion system decides the vibrational state the ion is created in.

ionization of the ground electronic but highly vibrationally excited molecular state of the Rb_2 molecule, resonantly enhanced by the proximity of an intermediate molecular state. The whole process is represented in the Fig. 5.1 using the relevant potential energy curves of Rb_2 and Rb_2^+ [24,103] molecules.

5.2.1 Experimental setup

In this experiment an additional photo association laser is not used, instead the cooling laser for the MOT itself photo associate a small fraction of the atoms to excited molecular electronic states [104,105], i.e., $h\nu_{pa} = h\nu_c$. These molecules are formed in highly excited vibrational states, very close to the $5S_{\frac{1}{2}} + 5P_{\frac{3}{2}}$ asymptote. The excited states involved are 0_u^+, 1_g and outer well of 0_g^- and the molecules spontaneously decay to $^1\Sigma_g^+$ or $^3\Sigma_u^+$.

The ionization laser is a pulsed dye laser (SIRAH Laser-und Plasmatechnik GmbH, Model: CSTR-LG-18), pumped by the second harmonic of an Nd:YAG laser (Spectra-Physics, Model: LAB-190, with 10 Hz repetition rate and pulse duration 1-2 nS). Rhodamine B dye is used for the ionization, which can cover a wavelength range from 588 nm to 614 nm. After optimization of the ionization frequency for the production of a maximum number of detectable counts in the ion trap, the dye laser wavelength is set to 602.6 nm which ionizes the ground Rb_2 molecules to a ro-vibrational distribution of Rb_2^+ molecular ion states in $(1)1/2_g$ by two photon transition via the intermediate states (2) $^3\Sigma_g^+$ and (2) $^3\Pi_g$ of Rb_2.

Fig.5.2 shows the dye laser setup for the Rb_2^+ creation. The current controller for the Nd:YAG laser is triggered externally to control the production time of the ions very precisely. The second harmonic (532 nm) output from the Nd:YAG pumps the dye laser. The dye laser has an oscillator and an amplifier unit, which gives a usable output energy of ~ 10 mJ/pulse. The wavelength is adjusted by changing the angle of the grating in the laser, which is controlled using a computer interfaced to the dye laser. Part of the output is fed to a wavemeter using a multimode fiber to have an independent measure of the wavelength. As the wavemeter is calibrated to a known source of

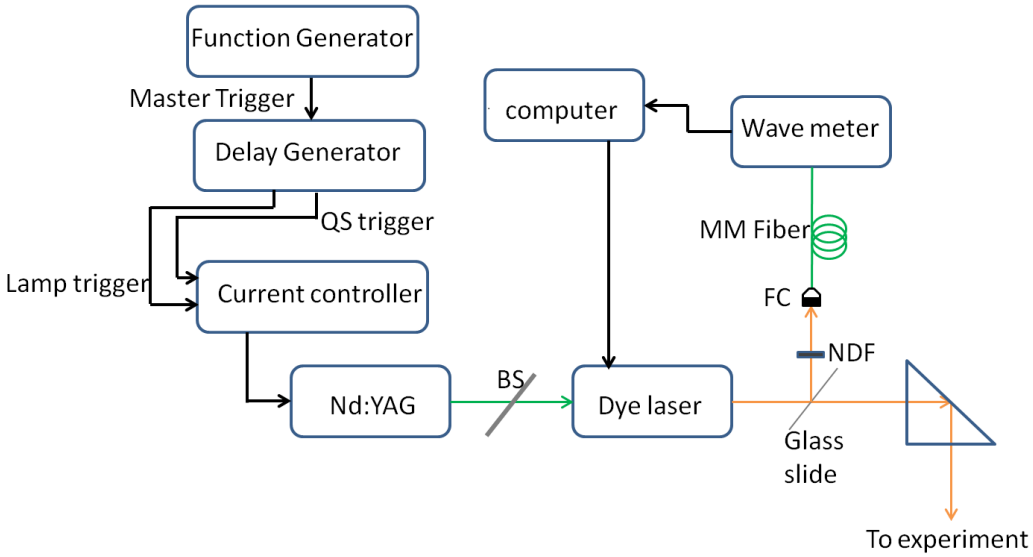

Figure 5.2: The dye laser setup for the ionization of Rb_2 molecule to produce of Rb_2^+ molecular ions is shown. The 532 nm second harmonics from the Nd:YAG laser is fed to the dye laser with Rhodamine 6B dye as the active medium. The laser is interfaced to a computer to control the grating position for wavelength tuning. The output beam wavelength is also measured using a wavemeter.

780 nm light, the actual wavelength is taken as the wavemeter reading. The ionizing pulse is then fed to the chamber from the top view port of the vacuum chamber to minimize the scattering from the tungsten wires.

Prior to the application of the laser pulse to the chamber, tests have been done for the safety of the experimental system. The strength and degradation of the thin tungsten wires used for the ion trap is tested, on a sample piece outside the experimental system, with focussed and unfocussed pulses of different wavelengths (355 nm, 532 nm, and 600 nm). It is observed that while the wires degrade and break on repeated application of focussed light pulses at high intensities are incident upon them, the energy densities of the unfocussed laser pulse is insufficient to cause any damage to the tungsten wires. Therefore we do not focus the dye laser pulse, but reduce the diameter to ~ 0.5 mm using a telescope arrangement.

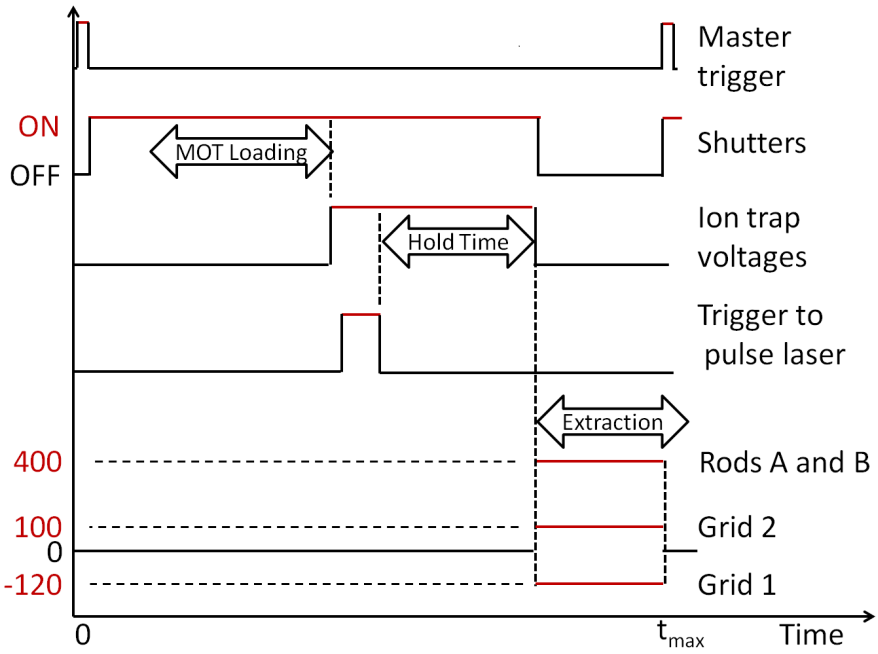

Figure 5.3: The time sequence for creating Rb_2^+ ions using a single ionization pulse, holding the ions in the ion trap and extracting is shown. The extraction voltages 400 V, 150 V and -120 V are switched using high voltage switching circuits, Behlke^{TM}(HTS-31).

5.2.2 Experimental sequence

The entire experiment is sequenced by triggering each instrument using a digital delay generator. For a particular sequence of experiment, a TTL pulse (master trigger) of repetition rate required for the experimental cycle is derived from a signal generator and triggers the digital delay generator. The *Rb* dispenser is kept on $\sim$ 30 minutes before the experiment starts, to ensure an equilibrium pressure of *Rb* vapour inside the chamber. The cooling and repumper lights for the MOT are initially blocked using an electromechanical shutter (Thorlabs: SH05). The ion trapping rf voltage is always kept *on* except while extracting the ions.

The time sequence for a single pulse ion creation, trapping and extraction is shown in Fig. 5.3. To start the experiment, the shutters are opened and the MOT is loaded to number saturation. The Nd:YAG current controller is then triggered to get a single pulse of ionization laser light, which is incident on the MOT. The ions created are then immediately extracted or held with/without the MOT and then extracted, depending

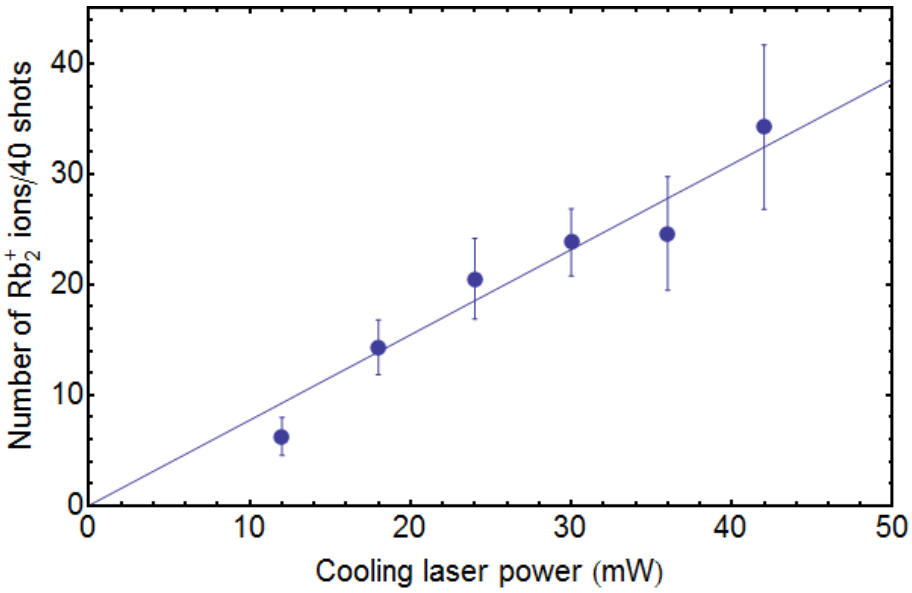

Figure 5.4: The figure shows Rb_2^+ molecular ion detection, and therefore production, with cooling light power. The Rb_2^+ molecules are produced from Rb_2 molecules formed via PA of Rb atoms in the MOT by the cooling laser field and hence is proportional to the power of the cooling laser beam. Here each data point is a sum of 40 shots and the error bar is the standard deviation of 10 such data sets. The fluctuation in the ion number is mainly due to the fluctuation in the dye laser output.

on the specific experiment. The ion signal from the CEM is recorded on the oscilloscope, which is triggered by the switching of the extraction voltage.

Figure 5.4 shows the number of Rb_2^+ ions detected versus the MOT cooling laser power. As the Rb_2 molecules are produced via the photo association process, the number of Rb_2 molecules and hence the Rb_2^+ molecular ion number are proportional to the cooling laser power [105, 106]. The data shown is taken with the ion trapping parameters $V_{rf} = 130$ V at 500 kHz. Since the number of parent Rb_2 molecules are small as additional PA laser is not used and since the pulse laser is not focussed, the number of Rb_2^+ molecular ions produced is detected to be 1 or 2 per shot. For this reason and since there is fluctuation in the dye laser output energy, we sum several shots to get reliable data. In the figure 5.4, each point is a sum of 40 shots and the error bar for each point is the standard deviation of 10 such data sets. Clearly the PA rate for the production of Rb_2 neutral molecules is proportional to the MOT light power. This implies that the

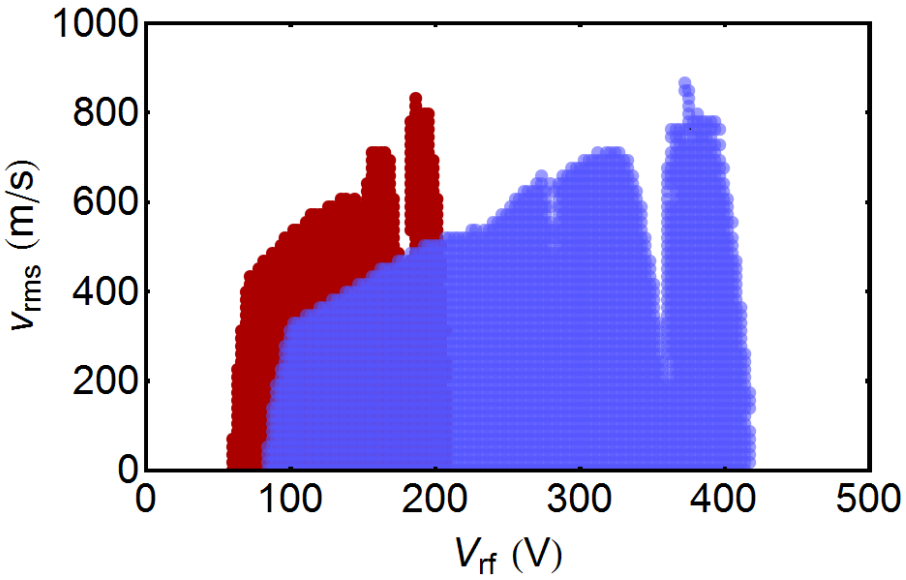

Figure 5.5: The points in the figure represents the ion's initial rms velocity vs trapping rf voltage at 500 kHz for which the ions are trapped. The maximum velocity at any V_{rf} represents the maximum velocity that an ion at the centre of the ion trap can have but still be trapped. The red and blue circles respectively represents the Rb^+ and Rb_2^+ ions.

ion production by two photon ionization of Rb_2^+, for constant pulsed laser intensity is also linear. The plot shows the number of ions detected, and establishes the overall linearity in the production of molecular ions.

Large numbers of Rb^+ ions also are produced by the dye laser pulse either by two photon ionization of Rb (5P) atoms or by three photon ionization of the Rb (5S) atoms in the MOT. While extracting the ions, the trapping rf field is switched OFF to ensure mass resolved counts of Rb^+ and Rb_2^+ ions as explained in chapter 3. In the mass spectra, Rb^+ and Rb_2^+ ions have mean ToF of 4.7 μS and 6.7 μS respectively, allowing good mass resolution.

5.3 Trapping of Rb_2^+ ions

The atom trap and the ion trap centers coincide with each other. Since both the atomic and molecular ions are created from the MOT, they are created at the centre of the ion trap. The ion trap voltages are *on* during the ionization process. As described in chap-

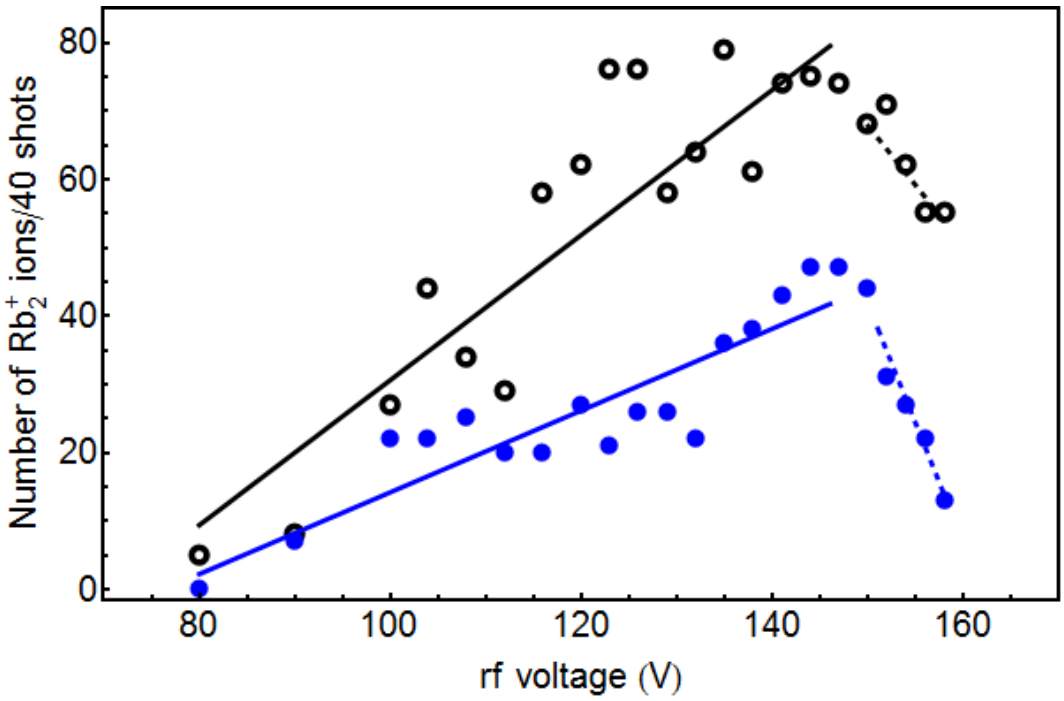

Figure 5.6: Figure shows the Rb_2^+ ion number vs trapping rf voltage at 500 kHz. The black points represents the ion number extracted immediately after creation and the blue points represents the ion number after holding for 20 seconds in the ion trap. The MOT trapping lights were turned *off* during this 20 seconds holdtime. Each data point is a sum of 40 shots. V_{rf} = 140 V to 150 V seems to be a good operating regime for the trapping. The solid line is a linear fit to the data. The ion number reduces beyond 150 V (fitted by the dashed line) because of distortions in the rf voltage.

ter 2, an rf voltage is applied to the inner pair of wires to trap the ions.

The optimal trapping voltages for Rb_2^+ ions are found using both simulation and experiments. For trapping, a suitable rf frequency of 500 kHz is chosen. In the simulation, a single ion with an initial rms velocity v_{rms} at the centre of the trap is evolved for 500 cycles of the trapping rf voltage V_{rf}, after which we check whether the ion continues to remain trapped. This is repeated for a range of initial velocities v_{rms} and rf voltages V_{rf}, and the combinations for which the ion is trapped is marked in the Fig.5.5. The simulation is done for Rb^+ and Rb_2^+ ions and are represented by red and blue circles respectively. The simulation result gives a range of voltages for which a single ion of Rb^+ and Rb_2^+ is stable in the trap.

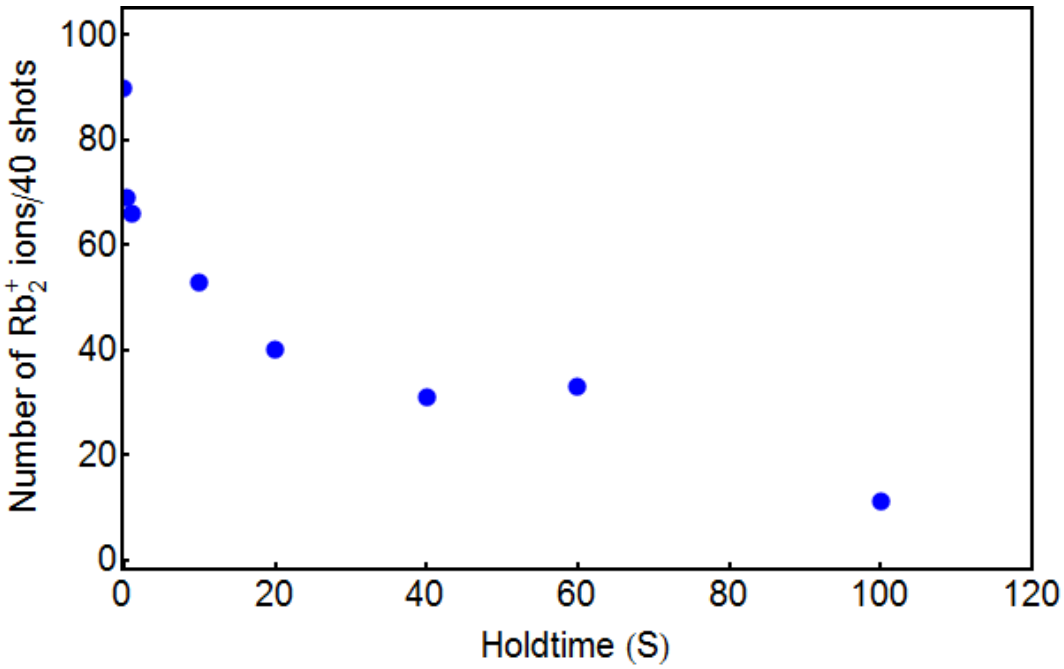

Figure 5.7: Lifetime of Rb_2^+ ions in the ion trap with V_{rf} =150 V at 500 kHz. The cooling and repumper lights are switched *off* while holding the ions in the ion trap. Each point is a sum of 40 creation-extraction cycles.

The experiments presented in the rest of this chapter are performed with the rf voltage optimized experimentally to ensure long lifetime of the Rb_2^+ ions. The ions are created in identical cycle, held in the ion trap and extracted for a range of trapping rf voltage, V_{rf}. Fig.5.6 shows the number of Rb_2^+ ions as a function of V_{rf}. The black open circles represents the number of ions extracted immediately after creation. The blue circles represents the ions extracted after a hold time of 20 seconds in the ion trap. This optimization is done with the trapping light fields for the MOT switched *off* during the hold time. It is clear from the figure that $V_{rf} = 140$ V to 150 V gives longer lifetime and a stable operating voltage and we chose to work with 150 V. As mentioned in chapter 3, the experimentally optimized V_{rf} for Rb^+ ions is 80 V and considering the mass relation, Rb_2^+ ions should be stable at 160 V. The simulated stability diagram in Fig.5.5 also shows that 160 V is a stable operating voltage for Rb_2^+ ions. The number of Rb_2^+ ions in the experimental signal reduces beyond 150 V because of the rf voltage distortion resulting from the gain-bandwidth saturation of the rf amplifier.

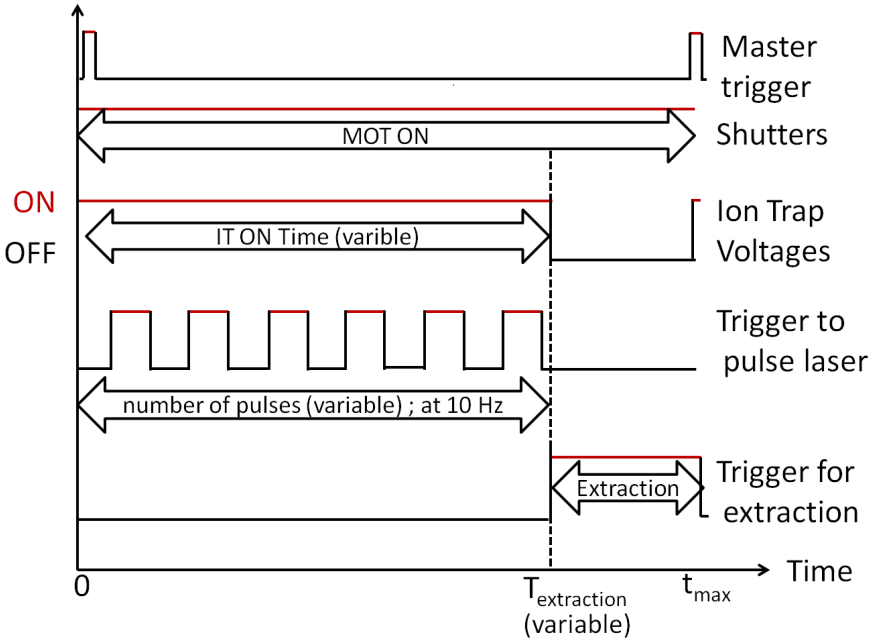

Figure 5.8: Figure shows the time sequence for the ion accumulation experiment. The ions are accumulated for N number of ionization pulses and then extracted.

The lifetime of Rb_2^+ ions in the ion trap with 150 V at 500 kHz is shown in Fig.5.7. This is a typical lifetime of the molecular ions in our ion trap. The data is taken with MOT trapping lights switched *off* after loading the ions and each point is a sum of 40 creation-extraction cycles.

5.4 Stability of Rb_2^+ ion in the hybrid trap

5.4.1 Ion accumulation

As already mentioned, the production rate of Rb_2^+ molecular ions per ionization pulse is small. Here we perform an experiment to collect the Rb_2^+ ions produced by many cycles of ionization pulses. The experimental cycle is schematically represented in Fig. 5.8.

The MOT is kept *on* throughout the experiment. The ion trapping voltages are *on* while loading the ions and switched *off* while extraction. In the experiment, a variable number (N) of ionization pulses are applied at a rate 10 Hz and the ions produced are

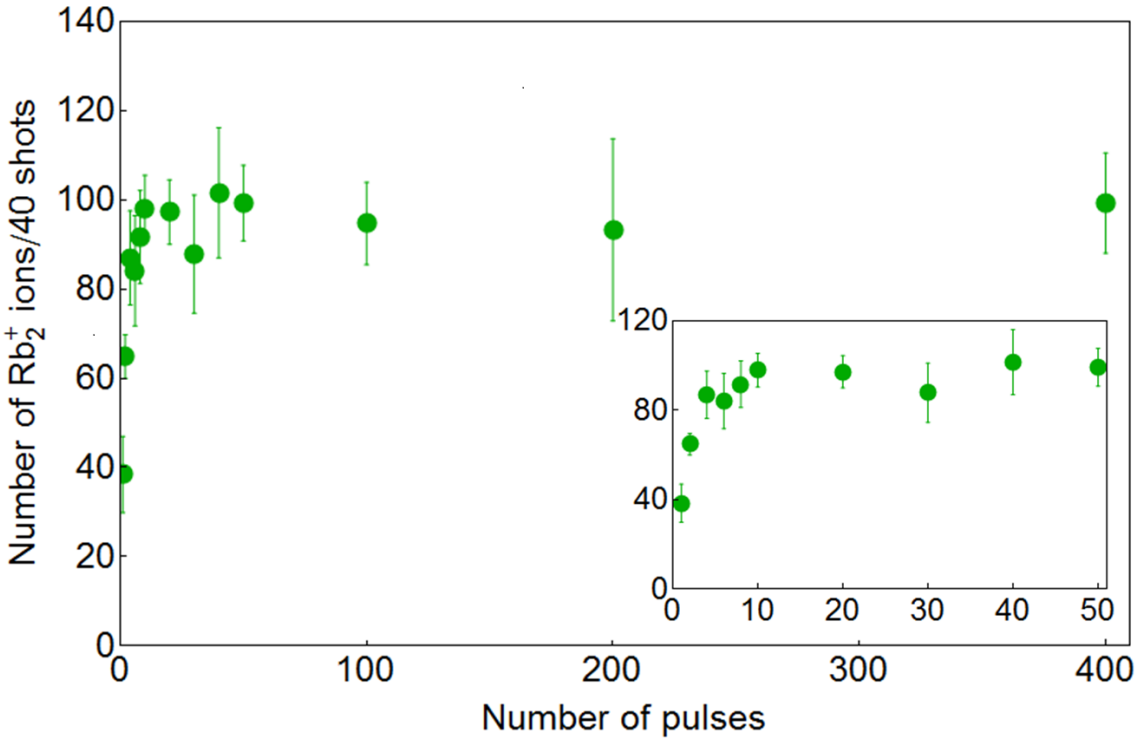

Figure 5.9: The Rb_2^+ ion number as a function of number of ionization pulses applied before extraction is shown in the figure. Each data point is a sum of 40 shots and the error bar is the standard deviation of 7 such data sets. The ion number increases with increase in the number of pulses up to 4 pulses and stabilizes to on an average of $\approx$ 2 ions detected per extraction. The inset shows a zoomed portion of the data with low number of ionization pulses. The MOT trapping lasers are kept *on* during the experiment.

immediately extracted. The data are taken for N varying from 1 to 400. One would expect a linear rise followed by saturation behaviour for the ions produced with increasing number of ionization pulses. A linear rise is expected because each ionization pulse would produce similar number of ions. The saturation occurs when a steady state is attained, when the ion creation rate and ion trap heating induced ion ejection rate become equal. The result is shown in Fig 5.9 where each point is a sum of 40 data and the error bar is the standard deviation of 7 such sets. The behaviour of the result is as expected, but the signal is saturating very fast. The data shows that the Rb_2^+ ions are accumulated only for 3 to 4 ionization pulses. This means that the ions are not stable beyond 400 mS and only the ions created in the last 3 to 4 pulses are detected.

Clearly there is an additional loss channel for the ions created. As can be seen from the Fig.5.7 which shows long ion trap lifetime for Rb_2^+, it is not the ion trap heating which is responsible for the rapid ion saturation in the trap, because the ions have a lifetime of few tens of seconds in the trap at 150 V. In order to understand the cause of rapid ion signal saturation of Rb_2^+ ions and the implied loss of molecular ions from the ion trap, we performed an ion lifetime experiment.

5.4.2 Ion Lifetime

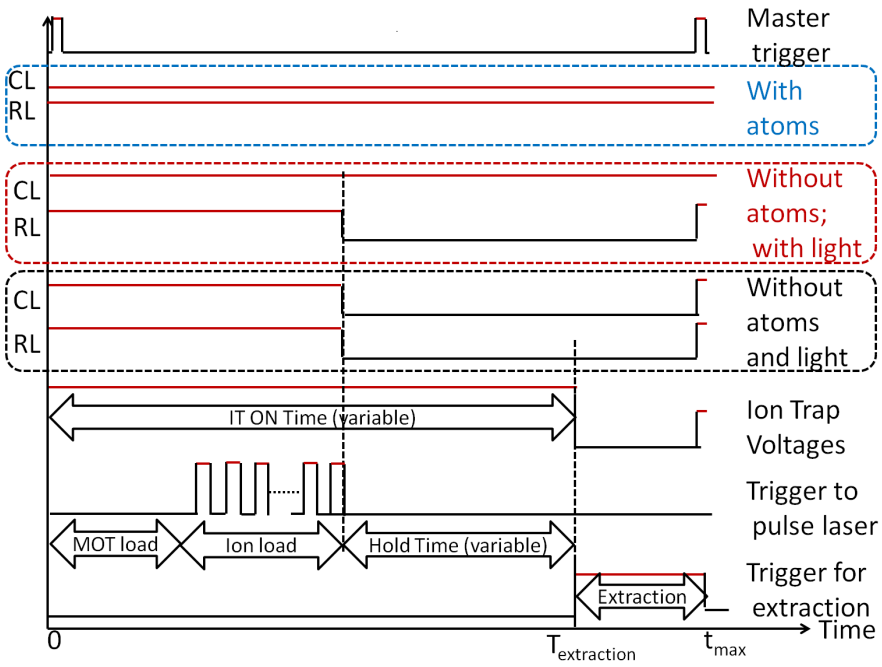

Figure 5.10: Figure shows the time sequence for the ion lifetime experiment. The three cases mentioned in the text are marked in three coloured blocks and the corresponding ion signal is shown in Fig. 5.11.

In this set of experiments, the ions are created in identical cycle, held in the ion trap in the presence and absence of the MOT for a variable hold time and then extracted. A schematic representation of the experimental cycle is shown in the Fig. 5.10. The complete picture emerges when 3 different measurements are made.

Case 1: The ions are held in the absence of atoms, cooling and repumping light beams. To do this, immediately after the creation of the ions, the MOT cooling and repumping

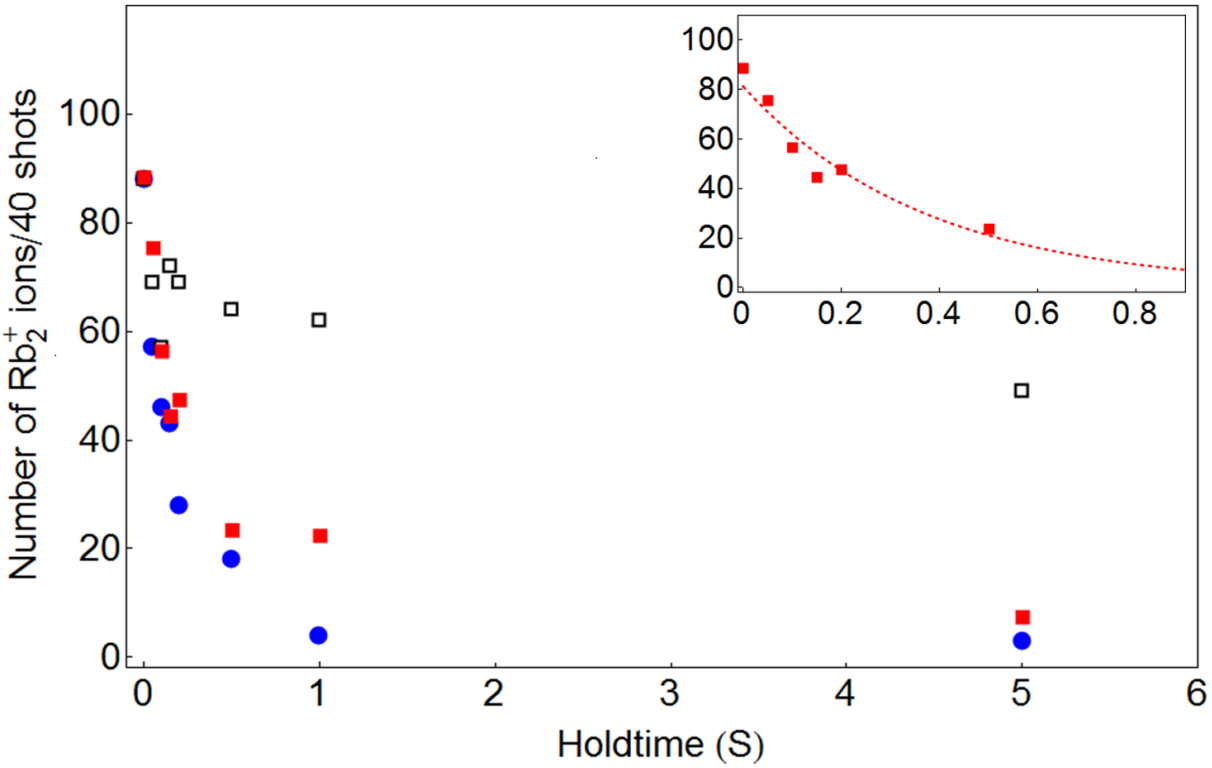

Figure 5.11: Figure shows the lifetime of Rb_2^+ ions in the ion trap with $V_{rf} = 150$ V at 500 kHz. The black open squares represents the lifetime in the absence of MOT atom and light fields. The blue circles represents the lifetime in the presence of MOT and the red squares shows the lifetime in the presence of cooling laser field without atoms. It is clear that the trapping light field is responsible for the short lifetime of Rb_2^+ ions.

laser lights are blocked using the shutter (represented within the black dotted block in Fig. 5.10). In this case, the lifetime of the Rb_2^+ ions in the ion trap is measured to be significantly in excess of 5 seconds, as shown by the black open squares in the Fig. 5.11. This establishes that the ions are not lost due to heating effects of the ion trap.

Case 2: In this case, the Rb_2^+ ions are held in the trap in the presence of atoms and cooling and repumping light beams (represented within the blue dotted block in Fig. 5.10). It is observed that the lifetime of the Rb_2^+ ions reduced to few hundreds of milliseconds as shown by the blue circles in the Fig. 5.11.

From the above two cases we conclude that the reduction in the Rb_2^+ ion lifetime is either due to the collision with the Rb atoms or due to the interaction with the trapping light field.

Case 3: In this case, the ion lifetime is measured in the presence of cooling beam, but with no atoms. This is done by blocking only the repumper light (typically 3 mW) using the shutter after the creation of the Rb_2^+ ions (represented within the red dotted block in Fig. 5.10). The result shown by the red squares in Fig. 5.11 leads to the inevitable conclusion that, just the presence of cooling light (power = 40 mW, 4 mm radius) causes the fast decay of Rb_2^+ ions.

5.5 Possible dissociation channels

In order to understand the interaction of Rb_2^+ molecular ions with the MOT cooling light ($h\nu_c$ = 12816.5 cm^{-1}), it is important to know the initial vibrational state in which Rb_2^+ ions are formed. The parent Rb_2 molecules are produced in their ground electronic state very close to the asymptote. The vibrational levels are very close in this regime, with a spacing less than 0.5 cm^{-1}. The two photons of dye pulse ($h\nu_i$ = 16595.3 cm^{-1}) ionize the Rb_2 molecules to Rb_2^+ ground electronic state with binding energy $\geq$ 500.2 cm^{-1} below the $5S_{1/2} + Rb^+$ asymptote. The vibrational level spacing in this regime is greater than 16 cm^{-1} and hence the assignment of Rb_2^+ initial vibrational state is not affected by the exact assignment of vibrational level of the initial Rb_2 molecule from which the Rb_2^+ molecular ions are created. Based on the calculation of vibrational energies for Rb_2^+ using the ab initio potentials, the vibrational level with binding energy close to 500.2 cm^{-1} is v =174 of $(1)1/2_g$ electronic state, which essentially implies that the ionization process can create Rb_2^+ in levels $v \leq$174.

Given the selection rules for dipole allowed transition between the electronic levels, there are two different channels for the excitation of the ground state Rb_2^+ molecule induced by the MOT cooling light. These excitation channels are shown in Fig. 5.12 and are:

(i) bound-bound excitation (indicated by "a" in Fig. 5.12) and spontaneous decay to ion-atom pair.

$Rb_2^+ + h\nu_c \rightarrow (Rb_2^+)^* \rightarrow Rb + Rb^+ + h\nu$

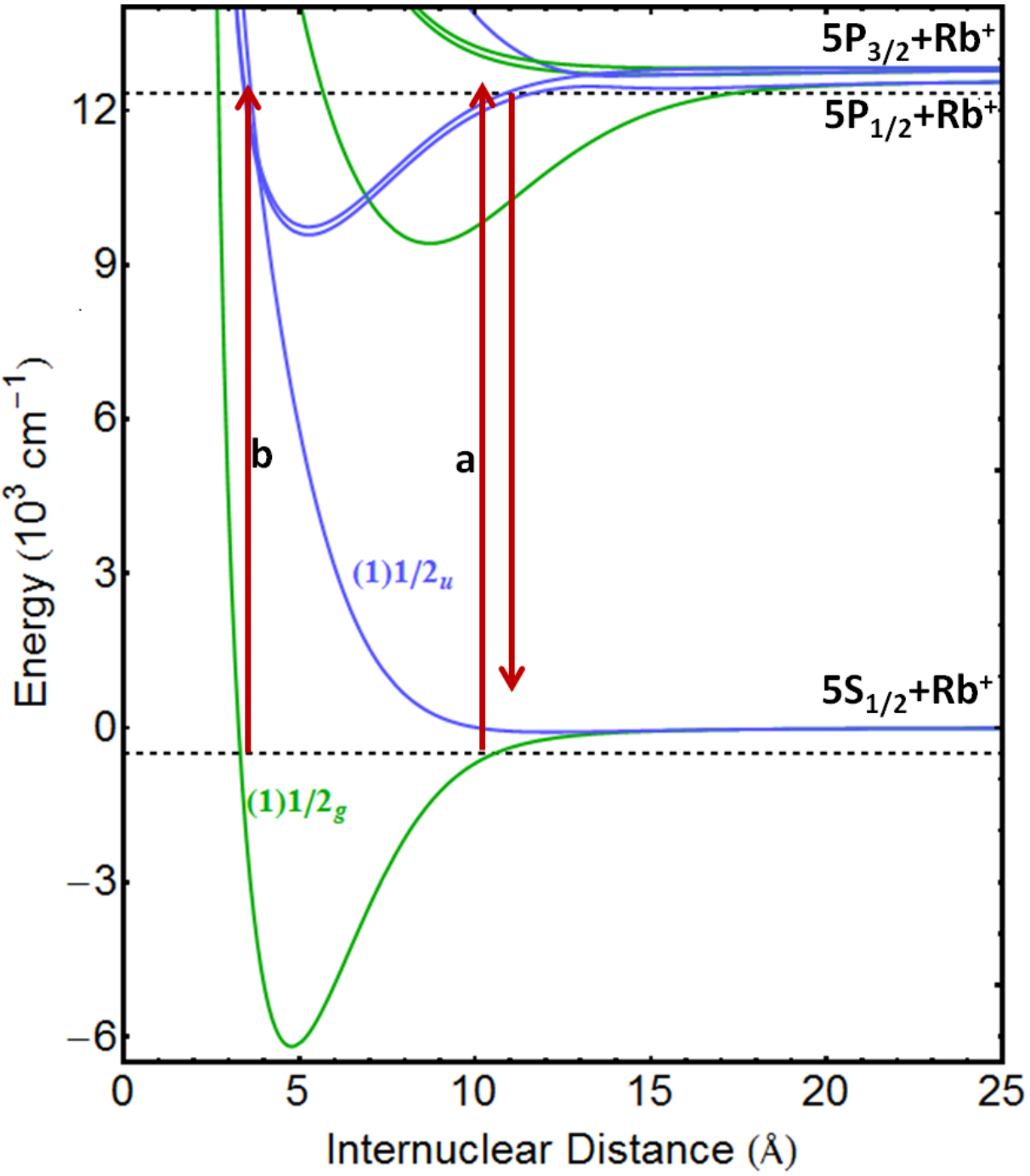

Figure 5.12: The ground and excited PECs of Rb_2^+ molecules is shown in the figure. The dissociation channels for the Rb_2^+ molecules by the MOT cooling laser light is marked. Channel "a" represents a bound to bound absorption followed by a spontaneous decay to ion atom pair in the dissociation continuum. In channel "b", the Rb_2^+ molecules are directly dissociated from $(1)1/2_g$ to $(1)1/2_u$ by the absorption of the MOT cooling light.

(ii) direct photo dissociation from $(1)1/2_g$ to $(1)1/2_u$ (indicated by "b" in Fig. 5.12).

$Rb_2^+ + h\nu_c \rightarrow Rb + Rb^+$

This transition is allowed since the states involved have the same multiplicity. This is in contrast to the case for the neutral Rb_2 molecule, where the molecular states dissociating to $5S_{1/2} + 5S_{1/2}$ have different multiplicities. This is why neutral molecule is unaffected by the cooling photon via this process, because it would be a singlet to triplet transition which is forbidden.

The possibilities for the dissociation of Rb_2^+ ions through these excitation channels are investigated by calculating the transition rates. This constitutes the subject of this section and the most relevant channel, direct photo dissociation of the molecular ion, is described in detail.

5.5.1 Case (i): Bound to bound absorption

The case is illustrated in more detail in Fig. 5.13 for the highest possible state $v = 174$. The energy of the cooling light $h\nu_c$ is insufficient to excite the molecule to the continuum of the first excited level (dissociating to $5P_{1/2} + Rb^+$). However, one can consider a resonant bound to bound transition and subsequent de-excitation to the ground state. If the de-excitation to the ground continuum dominates over de-excitation to the bound levels, this process can be considered as a dissociation channel. Given the selection rules, $\Delta\Omega = 0, \ \pm 1$ and $g \leftrightarrow u$, the dipole allowed transitions from $(1)1/2_g$ state are to the states $(2)1/2_u$, $(3)1/2_u$ and $(1)3/2_u$ represented by the blue PECs in Fig. 5.13. Of these states, $(3)1/2_u$ is energetically not accessible. The transition dipole moment (TDM) from the state $(1)1/2_g$ to the states $(2)1/2_u$, $(3)1/2_u$ and $(1)3/2_u$ are calculated by Allouche [107]. The TDMs are shown in Fig. 5.14. For the transition between $(1)1/2_g$ and $(2)1/2_u$, the TDM is almost zero in the regime of overlap between the bound wave functions, resulting in negligible overlap. Hence we consider only the $(1)1/2_g$ to $(1)3/2_u$ transition.

Matching a resonance condition for bound to bound transition is impractical based on ab initio PECs since the uncertainty in the potential well depth is of the order of 100

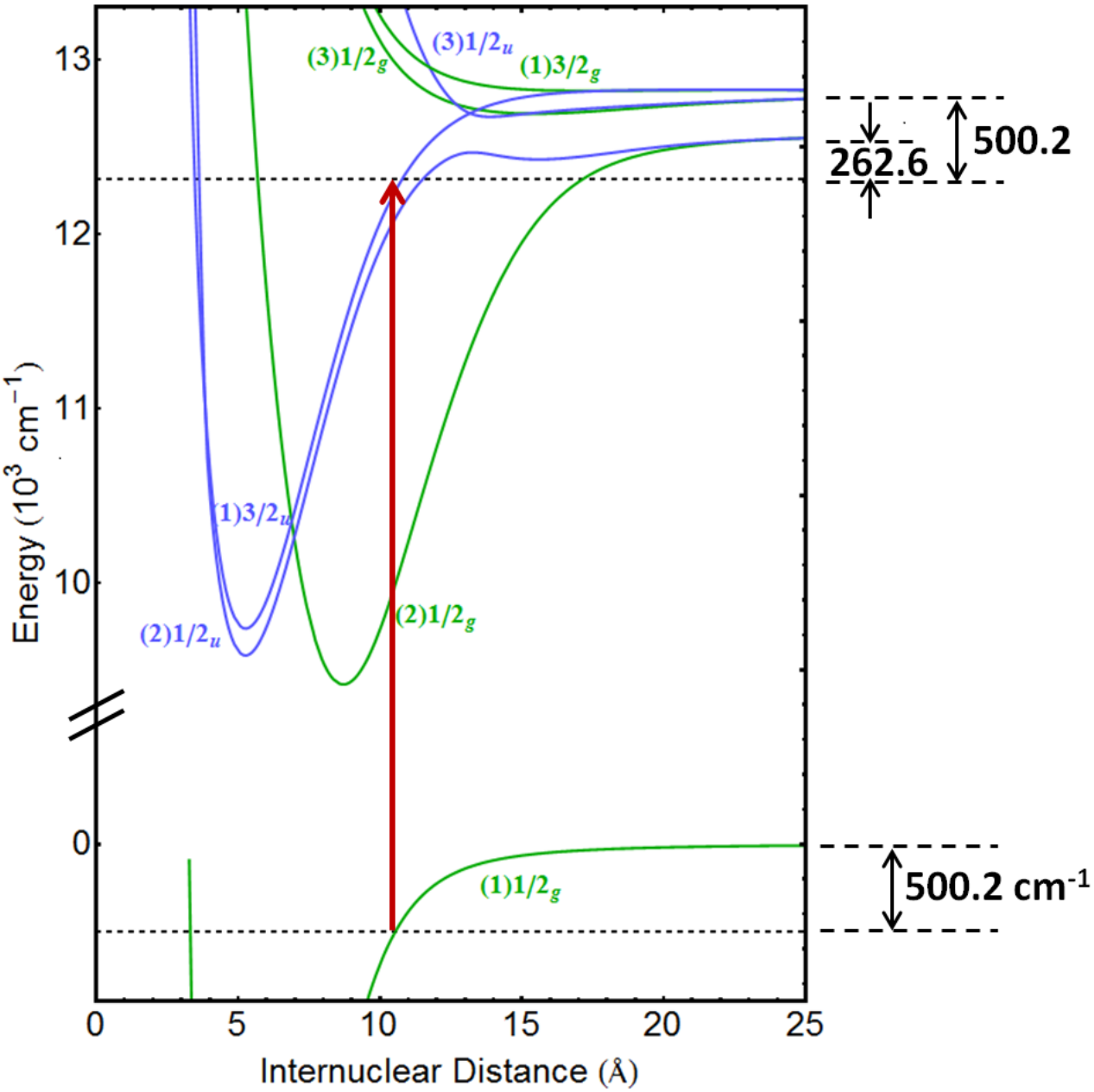

Figure 5.13: The dipole allowed transitions from $(1)1/2_g$ ground state are to the states $(2)1/2_u$, $(3)1/2_u$ and $(1)3/2_u$ represented by the blue PECs in the excited state. The photon energy $h\nu_c$ is insufficient to excite the molecule to the continuum of the first excited level. A bound to bound absorption can excite the molecule to $(2)1/2_u$ state with binding energy 262.6 cm^{-1} or $(1)3/2_u$ state with binding energy 500.2 cm^{-1}. The state $(3)1/2_u$ is energetically not accessible.

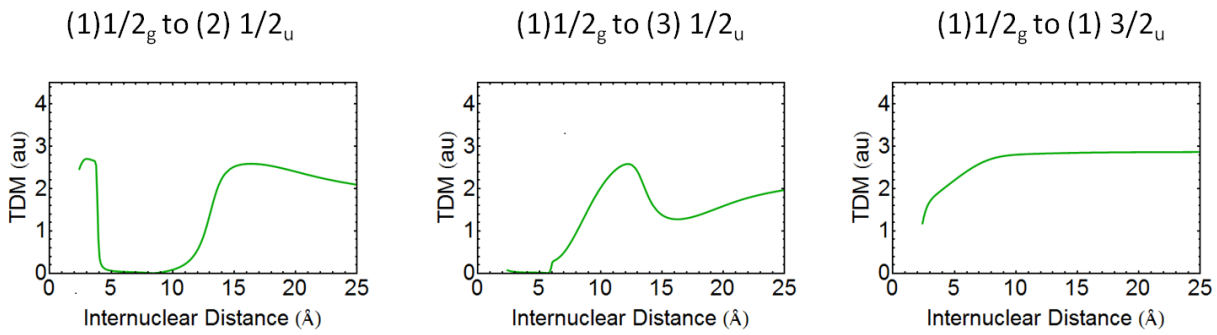

Figure 5.14: Figure shows the transition dipole moments for the relevant transitions between the ground and first excited states of Rb_2^+ molecular ion [107].

cm^{-1}. So within the accuracy and precision levels of the calculations, it is reasonable to consider a resonant transition to the closest vibrational level (v' =130) in $(1)3/2_u$ electronic state. We represent this transition by $v(174) \rightarrow v'(130)$. The spontaneous emission rate from $v'(130)$ to the bound and free states of $(1)1/2_g$ are calculated using the technology developed in the previous chapter. It is found that the population in the ground molecular ion state spreads and the decay predominantly populates $v(178)$, significantly higher than the initial $v(174)$ level. This is because the wave function for $v'(130)$ level has higher Franck-Condon overlap with the wave function for $v(178)$ level than for the $v(174)$ level. The bound to continuum spontaneous emission rate is negligibly small, eliminating the possibility of dissociation in a single step. Thus one cycle of absorption and spontaneous emission of photon shifts the initial population to a slightly higher vibrational level. The process may however continue leading to the population of higher and higher vibrational levels. For example, the molecules from $v(178)$ in $(1)1/2_g$ state are excited, based on energy considerations, to $v'(134)$ in $(1)3/2_u$ and the spontaneous decay predominantly populates $v(182)$ in $(1)1/2_g$. Fig. 5.15 and 5.16 shows the spontaneous emission rate from $(1)3/2_u$ ($v^{'}$= 130, 135, 140, 144, 149, 153, 157 and 161) states to the vibrational levels v of the ground state. The fraction of molecules spontaneously decayed to the bound and free states from the above mentioned excited levels is presented in Table 5.1.

The spontaneous emission to higher vibrational levels is seen until the state $v(206)$ is reached, from where the closest resonance is to $v'(165)$ having maximum Franck-

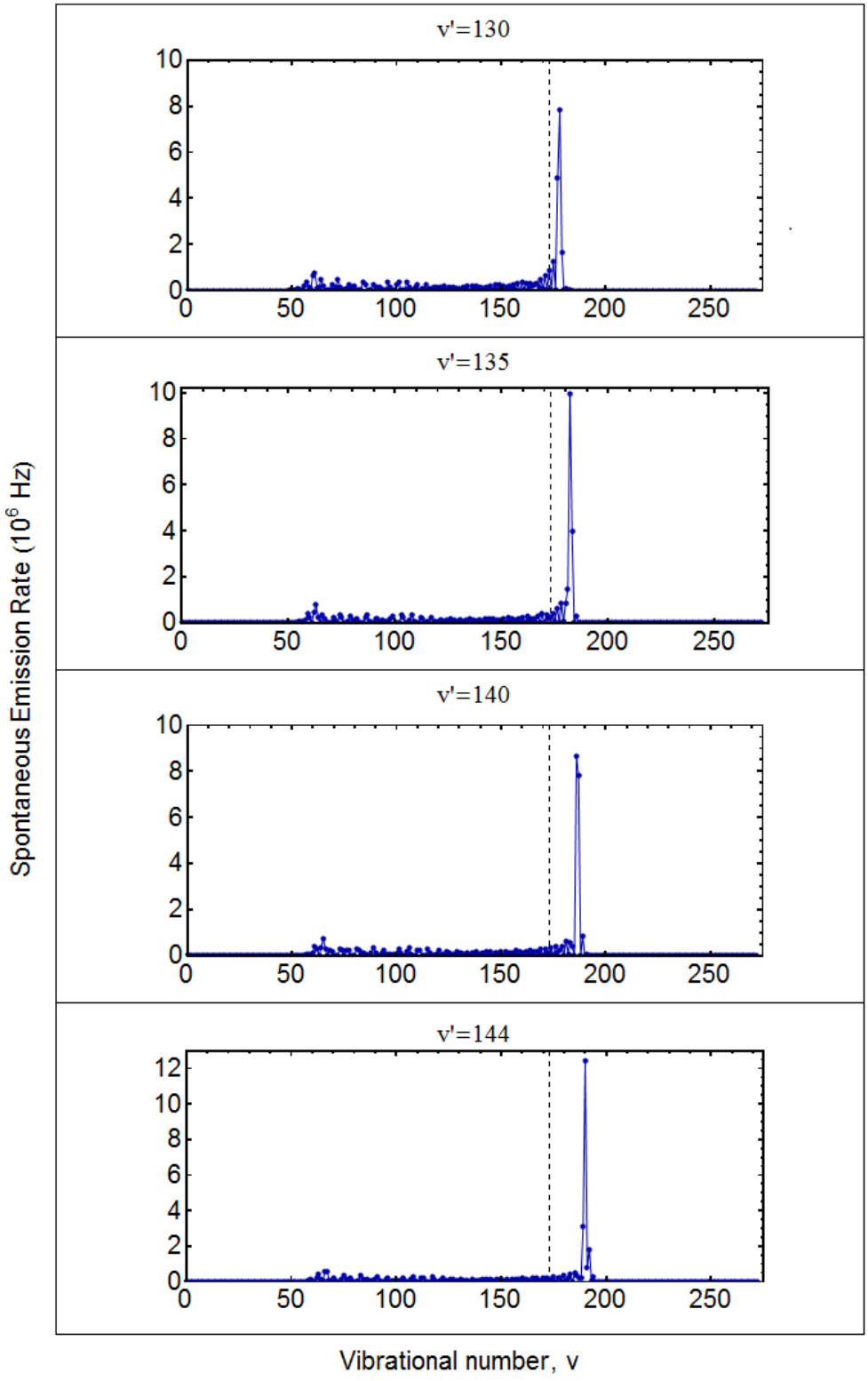

Figure 5.15: (a) The spontaneous emission rate from (v'=130, 135, 140, 144) vibrational levels of $(1)3/2_u$ to all the vibrational levels of the $(1)1/2_g$ ground state. The vertical line represents the initial ground vibrational state (v=174) in which the Rb_2^+ ions are created.

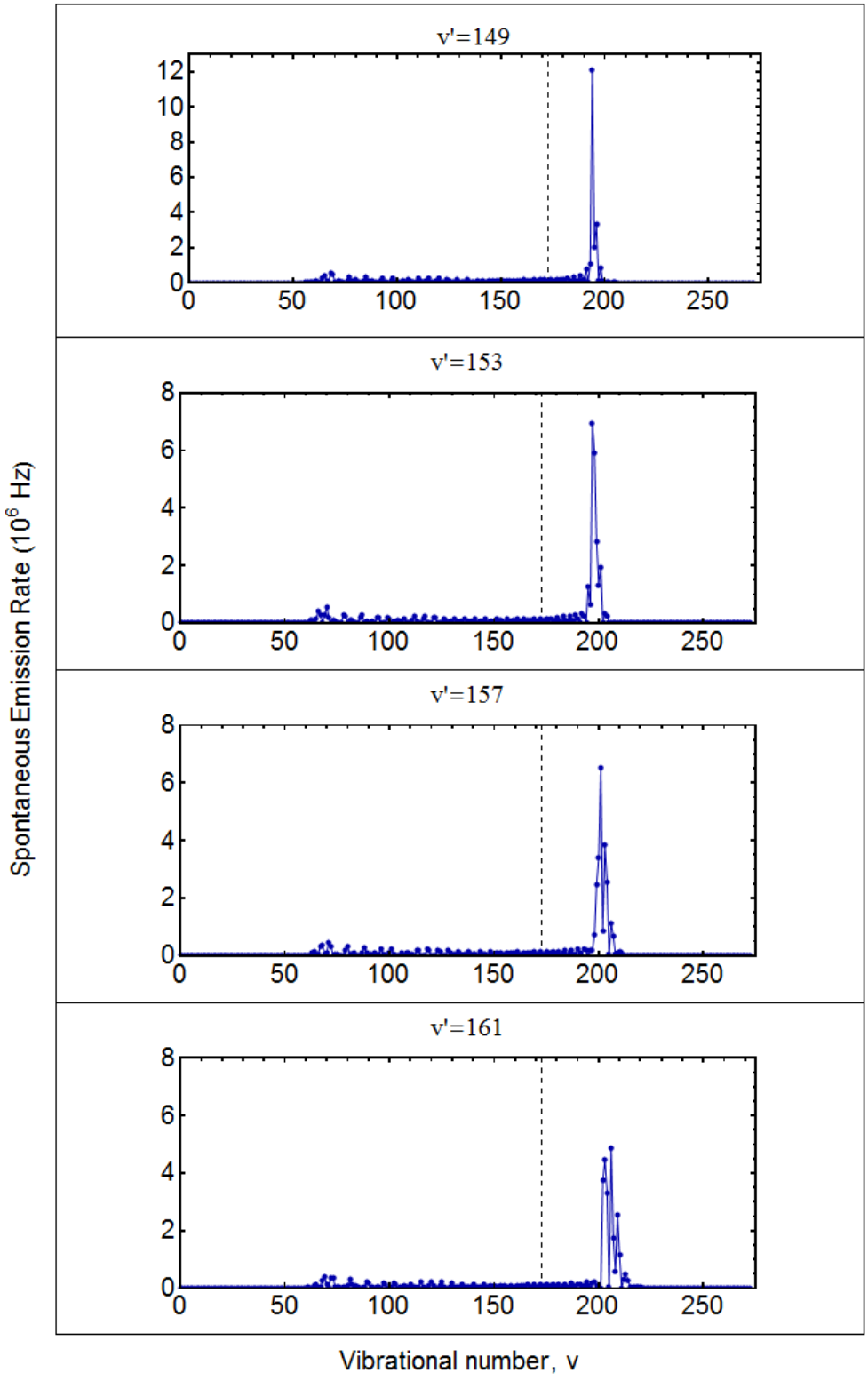

Figure 5.16: (a) The spontaneous emission rate from (v'=149, 153, 157, 161) vibrational levels of $(1)3/2_u$ to all the vibrational levels of the $(1)1/2_g$ ground state. The vertical line represents the initial ground vibrational state (v=174) in which the Rb_2^+ ions are created.

Condon overlap with $v(206)$. Hence the spontaneous emission is mostly back to the initial state, $v(206)$. The molecular transitions therefore attain a limit cycle. In each case, the resonance condition is not satisfied, but only the nearest excited vibrational level from a given initial ground level plus a cooling photon is considered. The possibility for a resonance condition to be met can be slightly increased, when one considers the Doppler broadening due to the molecular ion velocity in the ion trap. The maximum shift is approximately $\pm$ 10 GHz. Since the spontaneous emission rate to the continuum is very small (Table 5.1), the successive excitation-de-excitation of the molecular ion is not a viable process to explain the disappearance of the molecular ions from the trap. In addition, it is worth noting that one is always considering the closest transition to the cooling light frequency and therefore the resonance condition for multiple up-down transition is most likely interrupted very early on. The bound to free de-excitation rate is calculated for all possible excitations (from v <174) and found to be negligibly small.

Table 5.1: The initial ground vibrational level (v_i), the closest resonant vibrational level in the excited state (v'), the highest populated ground vibrational level in spontaneous emission from v' (v_n) and the branching ratios γ_b/γ_t and γ_f/γ_t for few transitions are tabulated.

v_i	v'	v_n	γ_b/γ_t	γ_f/γ_t
174	130	178	1	0
178	135	182	1	0
182	140	186	1	0
186	144	190	1	0
190	149	194	1	0
194	153	197	1	0
197	157	201	0.99999961	3.9×10^{-7}
201	161	206	0.99999392	6.08×10^{-6}
206	165	206	0.99980917	0.00019083

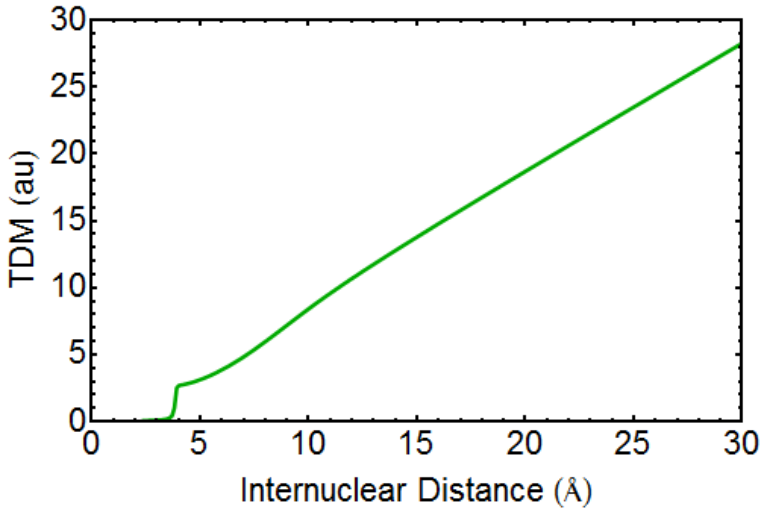

Figure 5.17: Figure shows the transition dipole moment $d(R)$ for the transition between $(1)1/2_g$ and $(1)1/2_u$ states of Rb_2^+ molecular ion [107].

5.5.2 Case (ii): Direct Photo dissociation

In the direct photo dissociation (PD) process considered here, a bound Rb_2^+ molecule in $(1)1/2_g$ absorbs a photon $h\nu_c$ leading to the dissociation into the continuum of $(1)1/2_u$ into Rb and Rb^+. The process is schematically shown in Fig. 5.18 in the left panels. The photo dissociation cross section depends on the photon energy and the Franck-Condon overlap between the levels involved, and is given by [108, 109]

$$\sigma_{pd} = 2.69 \times 10^{-18} \Delta E \, |\langle \psi_E(R)|d(R)|\psi_v(R)\rangle|^2 \tag{5.2}$$

where ΔE is the energy of the photon and $d(R)$ is the transition dipole moment between $(1)1/2_g$ and $(1)1/2_u$ states [107] and is shown in Fig. 5.17. Here σ_{pd} is given in cm^2. The rate of photo dissociation can be found by multiplying the cross section with the light flux.

$$R_{pd} = \sigma_{pd} \times Flux \tag{5.3}$$

$$Flux = \frac{I}{h\nu_c} \tag{5.4}$$

where I is the intensity of the light.

As the molecule is excited to a continuum, from a given bound level v, the cross

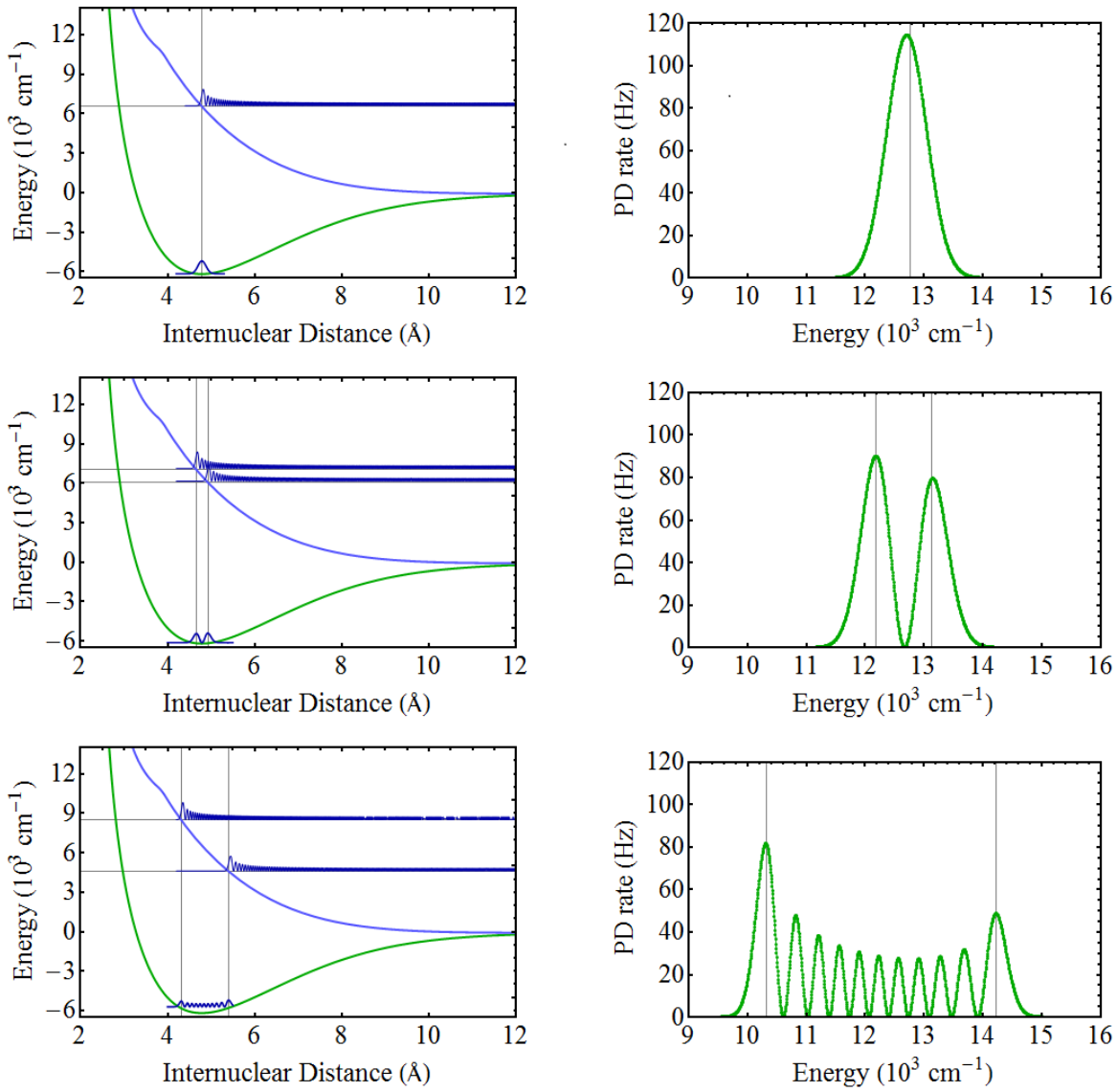

Figure 5.18: The figure illustrates the direct photo dissociation in Rb_2^+ molecular ion from bound levels 0, 1 and 10 of $(1)1/2_g$ potential. The left panel shows the $(1)1/2_g$ and $(1)1/2_u$ PECs, the initial bound vibrational level wave function and the final unbound wave functions. In the right panels, the corresponding photo dissociation rates as a function of dissociating light energy with 40 mW is shown.

section is a continuous function of excitation photon energy and peaks at vertical excitation energies corresponding to the bound wave function anti nodes. Thus, the peaks in the cross section as a function of photon energy reflect the anti nodes of the initial ground state vibrational wave function. As an example, the photo dissociation rate from $v = 0, 1, 10$ levels of $(1)1/2_g$ of Rb_2^+ molecule are shown in the right panels in the Fig. 5.18. The width of the peaks depends on the slope of the dissociating curve. The cross section peaks broaden for a steeper potential.

The photo dissociation from the initial vibrational level v= 174 is shown in detail in Fig. 5.19 and 5.20. With photon energy $h\nu_c$ = 12816.54 cm^{-1}, the calculated rate is 0.7 Hz. As already mentioned, the vibrational levels and wave functions are calculated based on ab initio potential. It is difficult to accurately know the uncertainty in the depth of the ab initio potentials. In the work done by M A Bellos et al [110], to find the upper bound to the Rb_2 ionization energy, an average error of 1.9% ($\approx$ 120 cm^{-1}) error in the dissociation energy of Rb_2^+ ground state is estimated. In this work, the experimentally determined dissociation energy is $\sim$ 120 cm^{-1} higher than the ab initio value. This leads to an uncertainty in determining the initial vibrational level in which Rb_2^+ ions are formed. We have calculated the photo dissociation rate from all the initial vibrational states within 120 cm^{-1} and the average rate obtained is 1.4 Hz. As can be seen from the Fig. 5.18 and Fig. 5.20, molecular ions in different vibrational levels dissociate at different rates in presence of the MOT cooling light with the lower vibrational levels dissociating at faster rates. For e.g., v=0, 30, 174 dissociate with peak rates 120 s^{-1}, 20 s^{-1}, 3 s^{-1} respectively, with corresponding lifetimes 8.3 ms, 50 ms, 333 ms). The experimentally observed lifetime of 390 ms implies that low vibrational levels (below v =30, lifetime few 10 ms) are either not created during the ionization process or, if created, dissociate much faster (within few 10 ms) than the duty cycle ($\sim$50 ms) of our experiment. These naturally lead to the observed ions in the experiment being associated with the higher vibrational states of the Rb_2^+ ions.

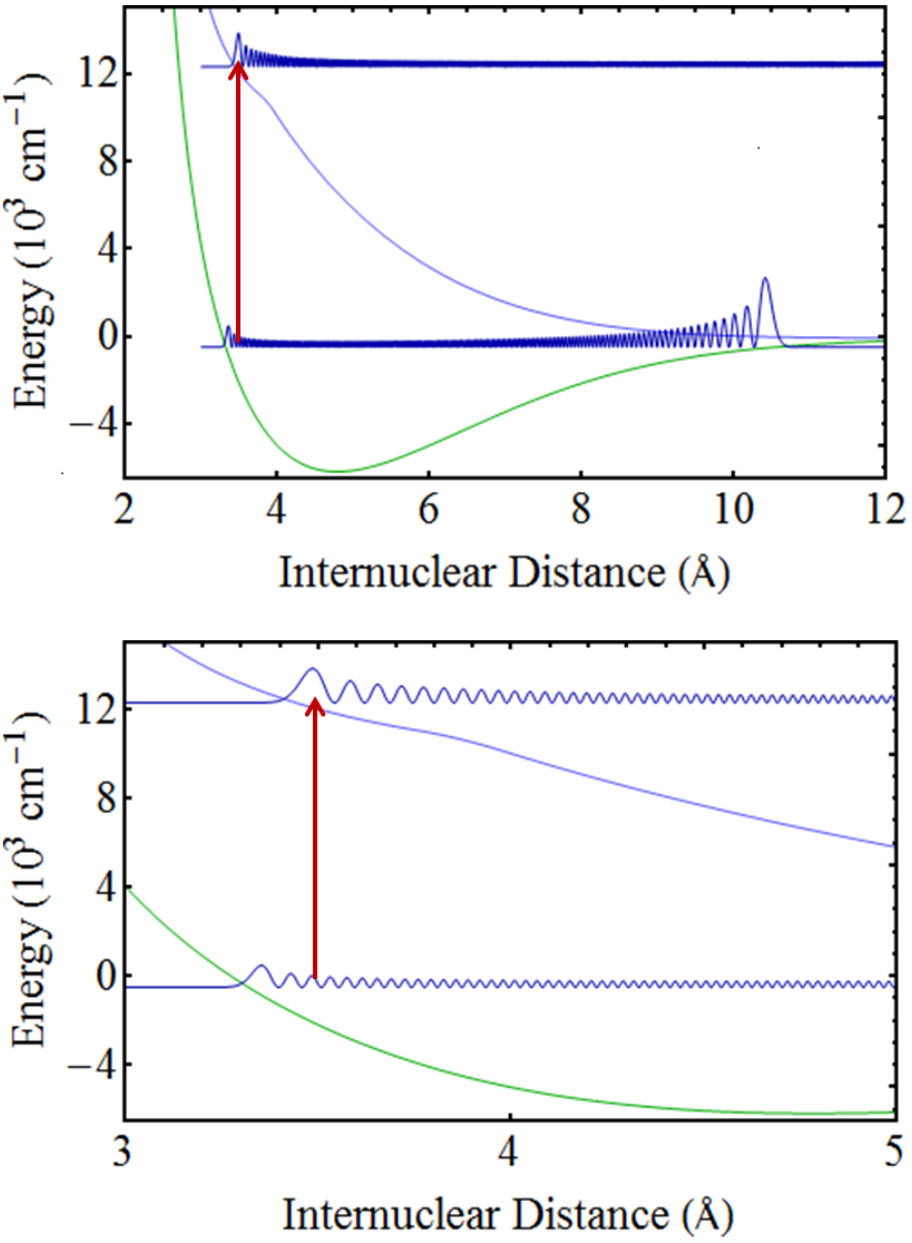

Figure 5.19: The figure illustrates the direct photo dissociation in Rb_2^+ molecular ion from the bound level 174 of $(1)1/2_g$ potential. The top panel shows the $(1)1/2_g$ and $(1)1/2_u$ PECs, the initial bound vibrational level wave function and the final unbound wave function at energy corresponding to the cooling light photon energy. The bottom panel shows a zoom at lower values of internuclear distance.

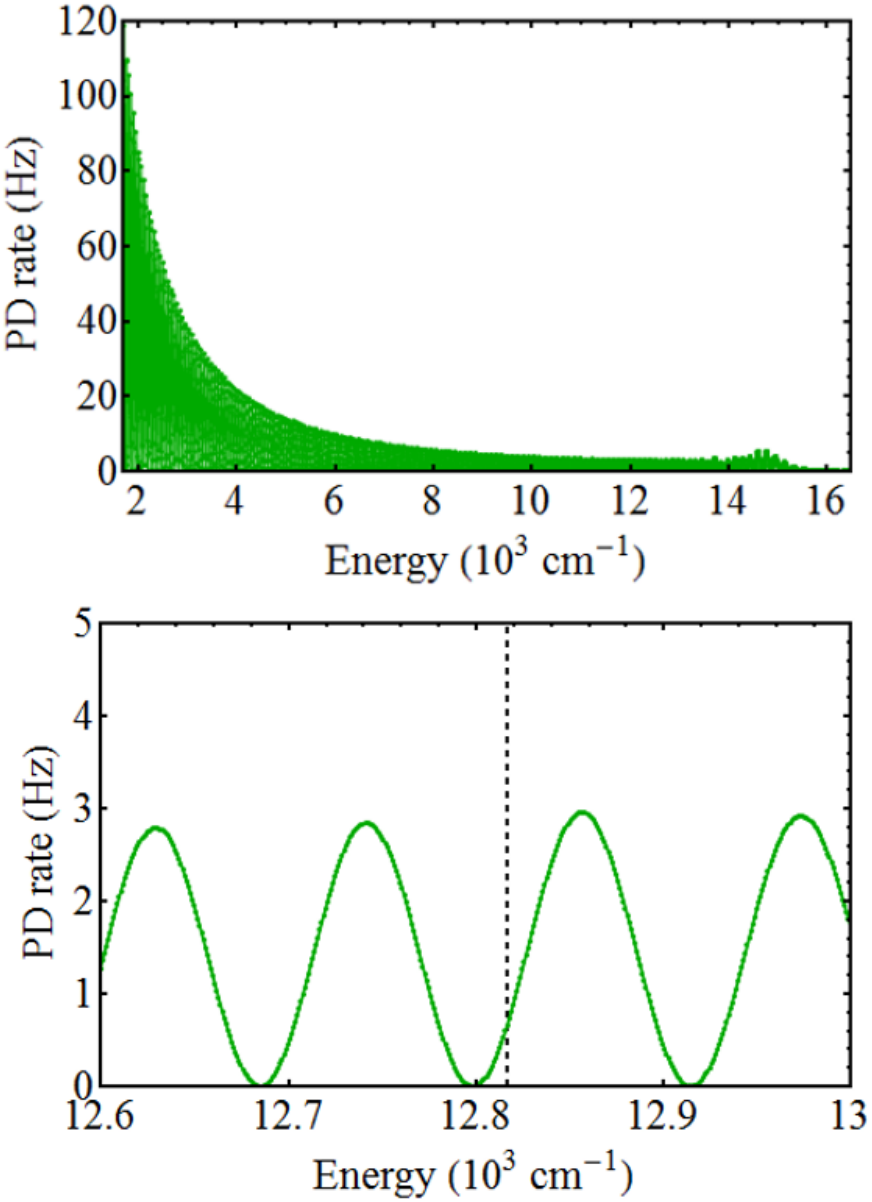

Figure 5.20: The figure shows the photo dissociation rate as a function of dissociating light energy in Rb_2^+ molecular ion from the bound level 174 of $(1)1/2_g$ potential. The bottom panel shows a zoom at energies close to the cooling photon energy, $h\nu_c$ =12816.54 cm^{-1} indicated by the dashed line.

5.6 Discussion

The single photon photo dissociation is the simplest model which can be constructed for the decay of Rb_2^+ molecules and the calculated rate is reasonably close to the experimentally measured value. We therefore conclude that this is the process responsible for the rapid loss of the trapped molecular ions that is observed. This conclusion allows us to infer that the destruction would also be the likely fate of an ion-atom PA from a MOT as the molecular ion would be created in the highly excited vibrational levels of the ground electronic state. Since we have figured out a major dissociation mechanism for Rb_2^+ molecular ions in our hybrid trap with infra-red light, the next step is to find a vibrational level to produce Rb_2^+ molecules, from where they do not photo dissociate. As can be seen from Fig. 5.18, the photo dissociation rate from the lower vibrational level is also quite large with $h\nu_c$ and hence the creation of Rb_2^+ molecules in lower vibrational levels will not help in avoiding the process. It is not trivial to find a vibrational level in $(1)1/2_g$ state with a low photo dissociation rate because of the uncertainty in the dissociation energy. However one can produce Rb_2^+ ions in the vibrational levels of $(1)1/2_u$ electronic state. This cannot be done with the present dye in the laser and the execution of which is a future project. If this works, since then the Rb_2^+ molecule is stable in the presence of the MOT, we can investigate the elastic and charge exchange collisions of Rb_2^+ with cold Rb atoms in the MOT to sympathetically cool the Rb_2^+ molecular ions.

Further, in our hybrid trap there is a possibility to create various homo-nuclear as well as hetero-nuclear molecular ions (K_2^+, Cs_2^+, Ca_2^+, RbK^+, KRb^+, etc). In the near future, we intend to investigate the molecular potential levels to find regimes for the creation of stable, trapped, molecular ions.

5.7 Conclusion

In this chapter, we have discussed the production, trapping and stability of Rb_2^+ molecular ions in our hybrid trap. The experimental results shows that the Rb_2^+ molecular ion signal decays faster in presence of Rb MOT, and further investigation revealed that the MOT cooling light causes this fast decay. Two channels for the dissociation of Rb_2^+ molecular ions are proposed and the rates for the processes are calculated. The process of absorption of $h\nu_c$ photons to populate the excited electronic level bound states and the subsequent de-excitation to free ion-atom state is neglected since the dissociation rate is negligible. The direct photo dissociation rate from bound levels of $(1)1/2_g$ state to free states of $(1)1/2_u$ are calculated. The calculated rate is found to be reasonably close to that observed in the experiment. A proposal is made to create the Rb_2^+ molecules in $(1)1/2_u$ electronic state, from which the molecule should not photo dissociate.

CHAPTER 6

Summary

6.1 Summary of the results

The work presented in this thesis deals with atoms, ions and molecules in cold temperature regime trapped in the same spatial volume in a hybrid trap. The various aspects of the experimental system, with the MOT for atoms and Paul trap for ions, both sharing the same spatial volume in the mode of a Fabry-Perot cavity, are characterized in detail. The number of atoms in the MOT and the atom density are determined by optical imaging techniques and the atom temperature is estimated by a time of flight method utilizing the collective strong coupling of the atoms into the cavity mode.

Extensive numerical simulations are performed to characterize the spherical and linear Paul traps for the ions. The optimal trapping regime, trap depth, trap extent and secular frequencies for the ions in both the traps are computed using Rb^+ ions. The experimental observations matches well with the numerical results. In addition, the electrodes for the ion trap can be biased to form a neutral polar molecule trap. The trap depths for various molecules which can be produced in the present system is estimated.

The conventional ion-extraction scheme along the trap axis is not practical for the present experiment since the cavity axis shares the symmetry axis of the ion trap. Hence a transverse extraction method is devised and implemented. It is demonstrated experimentally as well as by numerical simulations that the ToF distribution of the ions depends critically on the rf phase at which the extraction potentials are switched *on*. In case of a single ion species, the ion pile up problem in the detector is solved by temporally dispersing the ToF distribution by precisely timing the extraction electric field with respect to the phase of the rf trapping field. Using Rb^+ and Rb_2^+ ions we have demonstrated that the extraction should be performed with trapping rf voltage

switched *off* for a reliable mass spectroscopy of multiple ion species.

The thesis then describes the production and experiments with molecules and molecular ions. As the molecules possess rich internal structure, for state selective preparation and to model molecule light interactions, numerical codes are developed. The energy level structure for Rb_2 and Rb_2^+ molecules are then presented. The photo association of cold Rb atoms in the MOT to various vibrational levels in the excited electronic states is experimentally demonstrated. From the ground state Rb_2 molecules, Rb_2^+ molecular ions are created by resonant enhanced multi photon ionization. The ion trap is characterized to optimally trap the Rb_2^+ ions and their stability in the hybrid trap is studied in detail. The observed fast decay of Rb_2^+ ions is modeled using the codes developed to calculate molecular transition rates. The photo dissociation of Rb_2^+ ions is analyzed in detail.

6.2 The outcome of this work

Once we have a hybrid trap for atoms and atomic ions, it is natural to see how far the technology and the physics with the experiment can be pushed. With this in mind we have added to the possibilities by creating cold molecules and molecular ions. If the molecular ions can be trapped for a long time, then these can be used as the species for the study of molecular ion interactions. This is also very important as there is a significant connection between Rb_2^+ studied here and H_2^+, which is the simplest molecular system and therefore is at the heart of molecular physics. Further, H_2^+ is highly reactive and does not exist in detectable abundance in the universe. Ironically the Rb_2^+ ions share the same fate, and are hard to trap for long, in the presence of the MOT. While there might be a suggestion in the data that the collisions with the atoms also contribute to the trap loss of Rb_2^+, this has to be established by further experiments. In our work, we have determined that the cooling light of the MOT plays the dominant role in Rb_2^+ dissociation.

6.3 Future prospects

The simulations shows that the Rb_2^+ ions are not stable with Rb MOT cooling light even in the lower vibrational levels of $(1)1/2_g$ state. However, Rb_2^+ ions can be created in the vibrational levels of $(1)1/2_u$ state. Since the Franck-Condon overlap between the vibrational wave function of $(1)1/2_u$ state and the continuum wave function of $(1)1/2_g$ state is very small, one can expect that Rb_2^+ ions do not dissociate in presence of the MOT. Further, the collision between Rb_2^+ ions and cold Rb atoms in the MOT can be investigated for a possible sympathetic cooling of the non laser coolable Rb_2^+ ions. Alternatively, this might also lead to collisional destruction of Rb_2^+ ions. The numerical codes developed can be used for any diatomic molecule. Our experiment supports many atomic species (Potassium, Cesium and Calcium) which allows the production and manipulation of homo nuclear as well as hetero nuclear molecules. The cavity can be utilized to define standing wave dipole traps for the neutral cold atoms and molecules, which can be overlapped with the trapped ions.

There are two overlapping ion traps in this configuration (linear and modified spherical Paul trap) which can be used flexibly to many purposes. Laser coolable ions of Ca^+ can be used so that the optical detection of ions can be used for specific experiments. A large electric field can be generated at the center of the apparatus by appropriate biasing of the thin wires, which can be a used to define a quantization axis for aligning dipolar molecules. The neutral polar molecule electrostatic trap discussed in chapter 2 can be implemented using the tungsten wires. So the future is very fertile with this experiment.

APPENDIX **A**

SIMION geometry file for the ion trap

We provide the code to generate the electrode geometry of the ion trap (Fig.2.9 in chapter 2) using the software package SIMION 8.0. The labeling convention in this file for each electrode is retained in the thesis text.

The geometry file

;scaling: 4 grid units == 1 mm.

PA_Define(625,141,557,planar,non-mirrored)

Locate(276,70,278,1,0,0,0)

{

;————————————-Quadrupole electrodes

electrode(0) { fill { within{cylinder(-34,-34,154,6,6,308)} } }

electrode(0) { fill { within{cylinder(-34,34,154,6,6,308)} } }

electrode(0) { fill { within{cylinder(34,-34,154,6,6,308)} } }

electrode(0) { fill { within{cylinder(34,34,154,6,6,308)} } }

;————————————-Outer wire 1

electrode(0) {Fill{

within{box3D(-22,-22,-11.85,22,22,-12.15)} notin{box3D(-21.4,-21.4,-11.85,21.4,21.4,-12.15)}

within{cylinder(-34,-34,-11.85,12,12,0.3)} notin{cylinder(-34,-34,-11.85,11.4,11.4,0.3)}

within{box3D(-34,-34,-11.85,-22,-22,-12.15)} notin{box3D(-34,-34,-11.85,-22.6,-22.6,-12.15)}

within{cylinder(-34,34,-11.85,12,12,0.3)} notin{cylinder(-34,34,-11.85,11.4,11.4,0.3)}

within{box3D(-34,34,-11.85,-22,22,-12.15)} notin{box3D(-34,34,-11.85,-22.6,22.6,-12.15)}

within{cylinder(34,-34,-11.85,12,12,0.3)} notin{cylinder(34,-34,-11.85,11.4,11.4,0.3)}

within{box3D(34,-34,-11.85,22,-22,-12.15)} notin{box3D(34,-34,-11.85,22.6,-22.6,-12.15)}

within{cylinder(34,34,-11.85,12,12,0.3)} notin{cylinder(34,34,-11.85,11.4,11.4,0.3)}

within{box3D(34,34,-11.85,22,22,-12.15)} notin{box3D(34,34,-11.85,22.6,22.6,-12.15)} }}

;————————————-Outer wire 2

electrode(0) {Fill{

within{box3D(-22,-22,11.85,22,22,12.15)} notin{box3D(-21.4,-21.4,11.85,21.4,21.4,12.15)}

within{cylinder(-34,-34,12.15,12,12,0.3)} notin{cylinder(-34,-34,12.15,11.4,11.4,0.3)}

within{box3D(-34,-34,11.85,-22,-22,12.15)} notin{box3D(-34,-34,11.85,-22.6,-22.6,12.15)}

within{cylinder(-34,34,12.15,12,12,0.3)} notin{cylinder(-34,34,12.15,11.4,11.4,0.3)}

within{box3D(-34,34,11.85,-22,22,12.15)} notin{box3D(-34,34,11.85,-22.6,22.6,12.15)}

within{cylinder(34,-34,12.15,12,12,0.3)} notin{cylinder(34,-34,12.15,11.4,11.4,0.3)}

within{box3D(34,-34,11.85,22,-22,12.15)} notin{box3D(34,-34,11.85,22.6,-22.6,12.15)}

within{cylinder(34,34,12.15,12,12,0.3)} notin{cylinder(34,34,12.15,11.4,11.4,0.3)}

within{box3D(34,34,11.85,22,22,12.15)} notin{box3D(34,34,11.85,22.6,22.6,12.15)} }}

;————————————-Inner wire 1

electrode(1) {Fill{

within{box3D(-22,-22,-5.85,22,22,-6.15)} notin{box3D(-21.4,-21.4,-5.85,21.4,21.4,-6.15)}

within{cylinder(-34,-34,-5.85,12,12,0.3)} notin{cylinder(-34,-34,-5.85,11.4,11.4,0.3)}

within{box3D(-34,-34,-5.85,-22,-22,-6.15)} notin{box3D(-34,-34,-5.85,-22.6,-22.6,-6.15)}

within{cylinder(-34,34,-5.85,12,12,0.3)} notin{cylinder(-34,34,-5.85,11.4,11.4,0.3)}

within{box3D(-34,34,-5.85,-22,22,-6.15)} notin{box3D(-34,34,-5.85,-22.6,22.6,-6.15)}

within{cylinder(34,-34,-5.85,12,12,0.3)} notin{cylinder(34,-34,-5.85,11.4,11.4,0.3)}

within{box3D(34,-34,-5.85,22,-22,-6.15)} notin{box3D(34,-34,-5.85,22.6,-22.6,-6.15)}

within{cylinder(34,34,-5.85,12,12,0.3)} notin{cylinder(34,34,-5.85,11.4,11.4,0.3)}

within{box3D(34,34,-5.85,22,22,-6.15)} notin{box3D(34,34,-5.85,22.6,22.6,-6.15)} }}

;————————————-Inner wire 2

electrode(1) {Fill{

within{box3D(-22,-22,5.85,22,22,6.15)} notin{box3D(-21.4,-21.4,5.85,21.4,21.4,6.15)}

within{cylinder(-34,-34,6.15,12,12,0.3)} notin{cylinder(-34,-34,6.15,11.4,11.4,0.3)}

within{box3D(-34,-34,5.85,-22,-22,6.15)} notin{box3D(-34,-34,5.85,-22.6,-22.6,6.15)}

within{cylinder(-34,34,6.15,12,12,0.3)} notin{cylinder(-34,34,6.15,11.4,11.4,0.3)}

within{box3D(-34,34,5.85,-22,22,6.15)} notin{box3D(-34,34,5.85,-22.6,22.6,6.15)}

```
within{cylinder(34,-34,6.15,12,12,0.3)} notin{cylinder(34,-34,6.15,11.4,11.4,0.3)}
within{box3D(34,-34,5.85,22,-22,6.15)} notin{box3D(34,-34,5.85,22.6,-22.6,6.15)}
within{cylinder(34,34,6.15,12,12,0.3)} notin{cylinder(34,34,6.15,11.4,11.4,0.3)}
within{box3D(34,34,5.85,22,22,6.15)} notin{box3D(34,34,5.85,22.6,22.6,6.15)} }}
;————————————— Cavity piezo-electric transducer
electrode(0) {fill{
within{cylinder(0,0,126,34,34,1)} notin{cylinder(0,0,126,16,16,1)} }}
electrode(0) {fill{
within{cylinder(0,0,115,34,34,1)} notin{cylinder(0,0,115,16,16,1)} }}
;————————————— Grid 2
electrode(0) {Fill{
within{box3D(-22,-22,81.85,22,22,82.15)} notin{box3D(-21.4,-21.4,81.85,21.4,21.4,82.15)}
within{cylinder(-34,-34,82.15,12,12,0.3)} notin{cylinder(-34,-34,82.15,11.4,11.4,0.3)}
within{box3D(-34,-34,81.85,-22,-22,82.15)} notin{box3D(-34,-34,81.85,-22.6,-22.6,82.15)}
within{cylinder(-34,34,82.15,12,12,0.3)} notin{cylinder(-34,34,82.15,11.4,11.4,0.3)}
within{box3D(-34,34,81.85,-22,22,82.15)} notin{box3D(-34,34,81.85,-22.6,22.6,82.15)}
within{cylinder(34,-34,82.15,12,12,0.3)} notin{cylinder(34,-34,82.15,11.4,11.4,0.3)}
within{box3D(34,-34,81.85,22,-22,82.15)} notin{box3D(34,-34,81.85,22.6,-22.6,82.15)}
within{cylinder(34,34,82.15,12,12,0.3)} notin{cylinder(34,34,82.15,11.4,11.4,0.3)}
within{box3D(34,34,81.85,22,22,82.15)} notin{box3D(34,34,81.85,22.6,22.6,82.15)} }}
electrode(0) {Fill{
within{cylinder(-34,-34,76.15,12,12,0.3)} notin{cylinder(-34,-34,76.15,11.4,11.4,0.3)}
within{cylinder(-34,34,76.15,12,12,0.3)} notin{cylinder(-34,34,76.15,11.4,11.4,0.3)}
within{cylinder(34,-34,76.15,12,12,0.3)} notin{cylinder(34,-34,76.15,11.4,11.4,0.3)}
within{cylinder(34,34,76.15,12,12,0.3)} notin{cylinder(34,34,76.15,11.4,11.4,0.3)} }
locate(0,0,0,1,0,45,0) {Fill{
within{box3D(-60,-12,75.85,60,12,76.15)} notin{box3D(-59.4,-11.4,75.85,59.4,11.4,76.15)}
}}
locate(0,0,0,1,0,135,0) {Fill{
```

within{box3D(-60,-12,75.85,60,12,76.15)} notin{box3D(-59.4,-11.4,75.85,59.4,11.4,76.15)}
}}}
;————————————- CEM cone
electrode(0) { rotate_fill(360) {
within{box(178,-22,184.4,22)} within{polyline(184.4,-22,184.4,22,210,10,210,-10)}
within{box(210,-10,220,10)} notin{polyline(178,-20,178,20,220,0.8,220,-0.8)} }}
electrode(0) {Fill{ within{box3d(174,-32,-34,226,32,34)}
notin{box3d(174,-28,-30,226,28,30)} within{box3d(182,32,-30,202,66,30)} }}
;————————————- Grid 1
electrode(0) {fill{
within{box3d(160,-32,-34,168,32,34)} notin{box3d(160,-26,-28,168,26,28)} }
fill{
within{cylinder(159.9,0,28,0.1,0.1,56)} within{cylinder(159.9,4,28,0.1,0.1,56)}
within{cylinder(159.9,8,28,0.1,0.1,56)} within{cylinder(159.9,12,28,0.1,0.1,56)}
within{cylinder(159.9,16,28,0.1,0.1,56)} within{cylinder(159.9,20,28,0.1,0.1,56)}
within{cylinder(159.9,24,28,0.1,0.1,56)} within{cylinder(159.9,-4,28,0.1,0.1,56)}
within{cylinder(159.9,-8,28,0.1,0.1,56)} within{cylinder(159.9,-12,28,0.1,0.1,56)}
within{cylinder(159.9,-16,28,0.1,0.1,56)} within{cylinder(159.9,-20,28,0.1,0.1,56)}
within{cylinder(159.9,-24,28,0.1,0.1,56)} }
locate(0,0,0,1,0,0,-90) {fill{
within{cylinder(168.1,0,27,0.1,0.1,54)} within{cylinder(168.1,4,27,0.1,0.1,54)}
within{cylinder(168.1,8,27,0.1,0.1,54)} within{cylinder(168.1,12,27,0.1,0.1,54)}
within{cylinder(168.1,16,27,0.1,0.1,54)} within{cylinder(168.1,20,27,0.1,0.1,54)}
within{cylinder(168.1,24,27,0.1,0.1,54)} within{cylinder(168.1,-4,27,0.1,0.1,54)}
within{cylinder(168.1,-8,27,0.1,0.1,54)} within{cylinder(168.1,-12,27,0.1,0.1,54)}
within{cylinder(168.1,-16,27,0.1,0.1,54)} within{cylinder(168.1,-20,27,0.1,0.1,54)}
within{cylinder(168.1,-24,27,0.1,0.1,54)} }}}
;————————————- CEM anode
Locate(0,0,0,1,90,0,0) { electrode(0) {Fill{ within{cylinder(0,0,350,2.8,2.8,36)}}}}

```
;————————————————Chamber
electrode(0) {Fill{ Locate(0,0,0,1,90,0,90) {
Within{Cylinder(0,0,70,345,345,140)} Notin{Cylinder(0,0,32,232,232,64)}
Notin{Cylinder(0,0,70,218,218,38)} Notin{Cylinder(0,0,-32,218,218,38)} }
Notin{Cylinder(0,0,345,32,32,114)} ;—-port1
Notin{Cylinder(0,0,-231,32,32,114)} ;—-port2
Locate(0,0,0,1,90,0,0) { Notin{Cylinder(0,0,345,32,32,114)} ;—-port3 }
Locate(0,0,0,1,-90,0,0) {Notin{Cylinder(0,0,345,32,32,114)} ;—-port4 }
Locate(0,0,0,1,45,0,0) { Notin{Cylinder(0,0,345,32,32,114)} ;—-port5 }
Locate(0,0,0,1,-45,0,0) { Notin{Cylinder(0,0,345,32,32,114)} ;—-port6 }
Locate(0,0,0,1,135,0,0) { Notin{Cylinder(0,0,345,32,32,114)} ;—-port7 }
Locate(0,0,0,1,-135,0,0) { Notin{Cylinder(0,0,345,32,32,114)} ;—-port8 }
Locate(0,0,0,1,22.5,0,0) { Notin{Cylinder(0,0,345,32,32,114)} ;—-port9 }
Locate(0,0,0,1,-22.5,0,0) { Notin{Cylinder(0,0,345,32,32,114)} ;—-port10 }
Locate(0,0,0,1,67.5,0,0) { Notin{Cylinder(0,0,345,32,32,114)} ;—-port11 }
Locate(0,0,0,1,-67.5,0,0) { Notin{Cylinder(0,0,345,32,32,114)} ;—-port12 }
Locate(0,0,0,1,112.5,0,0) { Notin{Cylinder(0,0,345,32,32,114)} ;—-port13 }
Locate(0,0,0,1,-112.5,0,0) { Notin{Cylinder(0,0,345,32,32,114)} ;—-port14 }
Locate(0,0,0,1,157.5,0,0) { Notin{Cylinder(0,0,345,32,32,114)} ;—-port15 }
Locate(0,0,0,1,-157.5,0,0) { Notin{Cylinder(0,0,345,32,32,114)} ;—-port16 } }
;————————————————ss spacers
Fill{ within{cylinder(-15.24,-50.8,162,10,10,24)}
notin{cylinder(-15.24,-50.8,162,6,6,24)}
within{cylinder(15.24,-50.8,162,10,10,24)} notin{cylinder(15.24,-50.8,162,6,6,24)}
within{cylinder(-15.24,50.8,162,10,10,24)} notin{cylinder(-15.24,50.8,162,6,6,24)}
within{cylinder(15.24,50.8,162,10,10,24)} notin{cylinder(15.24,50.8,162,6,6,24)}
within{cylinder(-15.24,-50.8,-138,10,10,24)} notin{cylinder(-15.24,-50.8,-138,6,6,24)}
within{cylinder(15.24,-50.8,-138,10,10,24)} notin{cylinder(15.24,-50.8,-138,6,6,24)}
within{cylinder(-15.24,50.8,-138,10,10,24)} notin{cylinder(-15.24,50.8,-138,6,6,24)}
```

within{cylinder(15.24,50.8,-138,10,10,24)} notin{cylinder(15.24,50.8,-138,6,6,24)}

;————————————Groove grabber

within{box3d(-92,40.8,162,92,60.8,182)} within{box3d(-92,40.8,182,-72,60.8,210)}

within{box3d(72,40.8,182,92,60.8,210)} within{box3d(-92,-40.8,162,92,-60.8,182)}

within{box3d(-92,-40.8,182,-72,-60.8,210)} within{box3d(72,-40.8,182,92,-60.8,210)}

within{box3d(-92,40.8,-162,92,60.8,-182)} within{box3d(-92,40.8,-182,-72,60.8,-210)}

within{box3d(72,40.8,-182,92,60.8,-210)} within{box3d(-92,-40.8,-162,92,-60.8,-182)}

within{box3d(-92,-40.8,-182,-72,-60.8,-210)} within{box3d(72,-40.8,-182,92,-60.8,-210)}

Locate(0,0,0,1,90,0,0) {

within{box3d(-92,40.8,162,92,60.8,182)} within{box3d(-92,40.8,182,-72,60.8,210)}

within{box3d(72,40.8,182,92,60.8,210)} } } } }

APPENDIX **B**

Numerical codes: atom, ion and dipole molecule trap

We provide the numerical codes in Mathematica to calculate the MOT atom number from detected fluorescence, the ion trap a-q stability diagram, resonant frequencies, trap depth, spatial extent and the dipolar molecule trap depth in the electrostatic trap.

MOT number calculation

$h = 6.626068 * 10^{-34}$; (*Js*)

$\nu = 3.84230406373 * 10^{14}$; (*Hz*)

beamdia $= 8 * 10^{-3}$; (*Diameter of the cooling beam*)

power $= 40 * 10^{-3}$; (*W*)

viewportfact $= 0.96^2$;

Int $= \frac{1}{\left(\pi \frac{\text{beamdia}^2}{4}\right)}$(viewportfact $*$ power); (*Intensity of cooling beam*)

$\text{Int}_{\text{sat}} = (3.895) * \frac{10^{-3}}{10^{-4}}$; (*Rb saturation intensity *)

$\delta = 2\pi * 12 * 10^6$; (*laser detuning*)

$\Gamma = 2\pi * 6.0666 * 10^6$; (*Rb Natural linewidth *)

$R = \left(\frac{\Gamma}{2}\right) \frac{\left(\frac{\text{Int}}{\text{Int}_{\text{sat}}}\right)}{1+\left(\frac{\text{Int}}{\text{Int}_{\text{sat}}}\right)+4\frac{\delta^2}{\Gamma^2}}$; (*$s^{-1}$*)(* Rate of emission of photons per atom *)

chamberrad $= 0.085$; viewportrad $= 0.008$; (* viewport is the limiting diameter *)

focallength $= 60 * 10^{-3}$; (*Focal length of the lens L1 *)

dist $= 2 *$ focallength; (*distance of cloud from lens *)(*m*)

lensactiverad $= \frac{\text{viewportrad}}{\text{chamberrad}} *$ dist;

solidangle $= \frac{\pi * \text{lensactiverad}^2}{4 * \pi * \text{dist}^2}$;

PMT1200Vcalib $= \frac{492.337 * 10^{-3}}{10^{-9}}$; (*$\frac{V}{W}$*)

L1fact = 0.98559; L2fact = 0.98547;

MOTCBSfact = 0.529903; NDFfact = 0.531084;

powcalib = $\frac{1}{\text{PMT1200Vcalib}} * \frac{1}{\text{L1fact}} * \frac{1}{\text{L2fact}} * \frac{1}{\text{viewportfact}} * \frac{1}{\text{MOTCBSfact}} * \frac{1}{\text{NDFfact}}$;

(* Observed power of MOT flouresence by the PMT *)

MOTfactor = $\frac{\text{powcalib}}{R(\text{solidangle})h\nu}$;

PMTsignalAvg = 0.815;

MOTatomNumber = PMTsignalAvg * MOTfactor

Physical constants and ion trap potential

Here we provide the physical constants, conversion factors and the ion trap potential which is common for the next programs.

Constants and conversion factors:

$e = 1.60219 * 10^{-19}$; (*C*)

mRb85 = $1.409993199 \times 10^{-25}$; (*kg*)

$c = 2.99792 * 10^{8}$; (* m/s *)

kB = $1.38066 * 10^{-23}$; (* J/K *)

DebyeToCm = $3.33563 * 10^{-30}$; (*Dybye to Cm conversion*)

cmInvToJ = $1.98630 * 10^{-23}$; (*cm^{-1}toJouleconversion*)

Importing and interpolating the ion trap potential

r1 = $-10 * 10^{-3}$; r2 = $10 * 10^{-3}$; (*extent of the imported potential*)

filepath = F:\\Work\\IonTrap\";

file = OpenRead[filepath <> V_innerwires.txt]; V1 = Read[file, Expression];

Uinnerwires = ListInterpolation[V1, {{r1, r2}, {r1, r2}, {r1, r2}}];

file = OpenRead[filepath <> V_outerwires.txt]; V2 = Read[file, Expression];

Uouterwires = ListInterpolation[V2, {{r1, r2}, {r1, r2}, {r1, r2}}];

Program to generate a-q stability diagram

The program solves the ion equation of motion in the ion trap potential for a range of Vrf and Udc voltages to generate the a-q stability diagram in Fig. 2.11.

Parameters

$f = 500 * 10^3$; nCy $= 100$; (*number of cycles*)

Udc $=$ Table$[i, \{i, 0, 150, 300\}]$; (*range of dc voltage*)

Vrf $=$ Table$[i, \{i, 50, 400, 500\}]$; (*range of rf voltage*)

pos $= 0.00001$; (*m*) vel $= 10$; (*m/s*)

Solving differential equation

result $= \{\}$; tmax $=$ nCy$/f$;

For$[i = 1, i \leq$ Length[Udc]$, i$++, (For$[j = 1, j \leq$ Length[Vrf]$, j$++, (

sol $= \{\}$; xt $= \{\}$; yt $= \{\}$; zt $= \{\}$;

AppendTo[sol, NDSolve[{

$x''[t] ==$

$-e/\text{mRb85}\left(\partial_{x[t]}((\text{Udc}[[i]] + \text{Vrf}[[j]] * \text{Cos}[2\pi f t]) * \text{Uinnerwires}[x[t], y[t], z[t]]\right.$

$-5 * \text{Uouterwires}[x[t], y[t], z[t]]))$,

$y''[t] ==$

$-e/\text{mRb85}\left(\partial_{y[t]}((\text{Udc}[[i]] + \text{Vrf}[[j]] * \text{Cos}[2\pi f t]) * \text{Uinnerwires}[x[t], y[t], z[t]]\right.$

$-5 * \text{Uouterwires}[x[t], y[t], z[t]]))$,

$z''[t] ==$

$-e/\text{mRb85}\left(\partial_{z[t]}((\text{Udc}[[i]] + \text{Vrf}[[j]] * \text{Cos}[2\pi f t]) * \text{Uinnerwires}[x[t], y[t], z[t]]\right.$

$-5 * \text{Uouterwires}[x[t], y[t], z[t]]))$, $x'[0] ==$ vel, $y'[0] ==$ vel, $z'[0] ==$ vel,

$x[0] ==$ pos, $y[0] ==$ pos, $z[0] ==$ pos$\}$, $\{x, y, z\}$, $\{t, 0,$ tmax$\}$, MaxSteps $\rightarrow 10000000]]$;

AppendTo[xt, x/.sol[[1]]]; AppendTo[yt, y/.sol[[1]]]; AppendTo[zt, z/.sol[[1]]];

xl $=$ Max[Table[Evaluate[Abs[$x[t]$]/.sol[[1]]], $\{t, 0,$ tmax, tmax$/1000\}$]];

yl $=$ Max[Table[Evaluate[Abs[$y[t]$]/.sol[[1]]], $\{t, 0,$ tmax, tmax$/1000\}$]];

$$\text{zl} = \text{Max}[\text{Table}[\text{Evaluate}[\text{Abs}[z[t]]/.\text{sol}[[1]]], \{t, 0, \text{tmax}, \text{tmax}/1000\}]];$$

$$\text{If}[(\text{xl} < 0.004 \&\& \text{yl} < 0.004) \&\& \text{zl} < 0.004,$$

$$\{\text{AppendTo}[\text{result}, \{\text{Vrf}[[j]], \text{Udc}[[i]]\}]\};];)])];$$

$$d = 0.0104;$$

$$\text{aq} =$$

$$\text{Table}\left[\left\{\frac{4*e*\text{result}[[i,1]]}{\text{mRb85}*(2\pi f)^2*d^2}, \frac{-8*e*\text{result}[[i,2]]}{\text{mRb85}*(2\pi f)^2*d^2}\right\}, \{i, 1, \text{Dimensions}[\text{result}][[1]]\}\right];$$

Program to find ion trap resonant frequencies

The program solves the ion equation of motion in the potential created by applying a voltage Vrf Cos(2πft)+Vexc Cos(2πf1t) to the inner pair of wires for a range of excitation frequencies f1 to generate the Fig. 2.14

Parameters

$f = 500 * 10^3$; (*rf frequency*)

$\text{Vrf} = 80;$ (*rf voltage*)

$\text{nCy} = 5000;\ \text{tmax} = \text{nCy}/f;$

$\text{f1} = \text{Table}[i, \{i, 100, 150000, 100\}]$; (*excitation frequency*)

$\text{Vex} = 1$; (*excitation voltage*)

pos = 0.00001; (*m*) vel = 10; (*m/s*)

Solving the Differential equation with resonant excitation

$\text{freqspectr} = \{\};$

$\text{For}[j = 1, j \leq \text{Length}[\text{f1}], j{+}{+}, (\text{sol} = \{\};$

$\text{AppendTo}[\text{sol}, \text{NDSolve}[\{$

$x''[t] == -e/\text{mRb85}\left(\partial_{x[t]}((\text{Vrf} * \text{Cos}[2\pi f t]\right.$

$+ \text{Vex} * \text{Cos}[2\pi \text{f1}[[j]]t]) * \text{Uinnerwires}[x[t], y[t], z[t]]$

$- 5 * \text{Uouterwires}[x[t], y[t], z[t]])),$

$y''[t] == -e/\text{mRb85}\left(\partial_{y[t]}((\text{Vrf} * \text{Cos}[2\pi f t]\right.$

$+ \text{Vex} * \text{Cos}[2\pi \text{f1}[[j]]t]) * \text{Uinnerwires}[x[t], y[t], z[t]]$

$- 5 * \text{Uouterwires}[x[t], y[t], z[t]])),$

$z''[t] == -e/\text{mRb85}\left(\partial_{z[t]}((\text{Vrf} * \text{Cos}[2\pi f t]\right.$

$+ \text{Vex} * \text{Cos}[2\pi \text{f1}[[j]]t]) * \text{Uinnerwires}[x[t], y[t], z[t]]$

$- 5 * \text{Uouterwires}[x[t], y[t], z[t]])),$

$x'[0] == \text{vel}, y'[0] == \text{vel}, z'[0] == \text{vel}, x[0] == \text{pos}, y[0] == \text{pos}, z[0] == \text{pos}\},$

$\{x, y, z\}, \{t, 0, \text{tmax}\}, \text{MaxSteps} \to 10000000, \text{EvaluationMonitor} :\to$

$\text{If}[(\text{Abs}[x[t]] > 0.004 \| \text{Abs}[y[t]] > 0.004 \| \text{Abs}[z[t]] > 0.004),$

$\{\text{AppendTo}[\text{freqspectr}, \{\text{f1}[[j]], t\}], \text{Continue}[]\}]];$

$\text{AppendTo}[\text{freqspectr}, \{\text{f1}[[j]], \text{tmax}\}];)]$

Program to find ion trap depth and spatial extent

The program solves the ion equation of motion in the ion trap potential for a range of initial velocities to estimate the trap depth given in Fig. 2.16. The program can be modified to find the spatial extent by solving for a range of initial positions as shown in Fig. 2.15

Parameters:

$f = 500 * 10^3$; (*rf frequency*)

$\text{nCy} = 5000$; (*number of cycle*)

$\text{tmax} = N[\text{nCy}/f]$;

$\text{Vrf} = 80$;

$\text{pos} = 0.00000001$; (*initialposition, m*)

Solving the Differential equation with different Vx:

$\text{KEx} = \text{Table}[i, \{i, 0, 0.72, 0.015\}]$; (*range of kinetic energy in eV*)

$\text{avgVx} = \sqrt{\frac{2 * \text{KEx} * e}{\text{mRb85}}}$

$$
\begin{aligned}
&\text{sol} = \{\};\\
&\text{NzerocrossVsBin} = \text{Table}[0, \{k, 1, \text{Dimensions}[\text{avgVx}][[1]]\}];\\
&\text{TimeVsVelX} = \text{Table}[0, \{k, 1, \text{Dimensions}[\text{avgVx}][[1]]\}];\\
&\text{For}[\text{ii} = 1, \text{ii} \leq \text{Dimensions}[\text{avgVx}][[1]], \text{ii++},\\
&(\text{AppendTo}[\text{sol}, \text{NDSolve}[\{\\
&x''[t] == -e/\text{mRb85}\left(\partial_{x[t]}(\text{Vrf} * \text{Cos}[2\pi f t] * \text{Uinnerwires}[x[t], y[t], z[t]]\right.\\
&\left. - 5 * \text{Uouterwires}[x[t], y[t], z[t]])\right),\\
&y''[t] == -e/\text{mRb85}\left(\partial_{y[t]}(\text{Vrf} * \text{Cos}[2\pi f t] * \text{Uinnerwires}[x[t], y[t], z[t]]\right.\\
&\left. - 5 * \text{Uouterwires}[x[t], y[t], z[t]])\right),\\
&z''[t] == -e/\text{mRb85}\left(\partial_{z[t]}(\text{Vrf} * \text{Cos}[2\pi f t] * \text{Uinnerwires}[x[t], y[t], z[t]]\right.\\
&\left. - 5 * \text{Uouterwires}[x[t], y[t], z[t]])\right),\\
&x'[0] == \text{avgVx}[[\text{ii}]], y'[0] == 0, z'[0] == 0, x[0] == \text{pos}, y[0] == \text{pos}, z[0] == \text{pos}\},\\
&\{x, y, z\}, \{t, 0, \text{tmax}\}, \text{MaxSteps} \to 10000000]];\\
&\text{xlim} = \text{Max}\left[\text{Table}\left[\text{Evaluate}[\text{Abs}[x[t]]/.\text{sol}[[1]]], \left\{t, 0, \text{tmax}, 10^{-7}\right\}\right]\right];\\
&\text{If}[\text{xlim} < 0.005, \text{TimeVsVelX}[[\text{ii}]] = \{\text{KEx}[[\text{ii}]], \text{tmax}\};];\\
&\text{If}[\text{TimeVsVelX}[[\text{ii}]] == 0,\\
&\text{fbin} = 40 * 10^3;\\
&\text{nbins} = \text{Round}[\text{fbin} * \text{tmax}];\\
&\text{bins} = \text{Table}\left[N\left[\tfrac{k}{\text{fbin}}\right], \{k, 0, \text{nbins}\}\right];\\
&\text{bx} = \text{by} = \text{bz} = \text{Table}[0, \{k, 1, \text{Dimensions}[\text{bins}][[1]] - 1\}];\\
&\text{xx} = \text{Table}[\text{Table}[\{N[t], \text{Evaluate}[x[t]/.\text{sol}[[1]]][[1]]\},\\
&\left\{t, \text{bins}[[j]], \text{bins}[[j+1]], 10^{-7}\right\}], \{j, 1, \text{nbins}\}];\\
&\text{For}[l = 1, l \leq \text{nbins}, l\text{++},\\
&\text{For}[m = 1, m \leq \text{Dimensions}[\text{xx}][[2]] - 1, m\text{++},\\
&\text{If}[\text{xx}[[l]][[m]][[2]] * \text{xx}[[l]][[m+1]][[2]] \leq 0, \text{bx}[[l]] = \text{bx}[[l]] + 1];\\
&]];\\
&\text{For}[s = 1, s \leq \text{nbins}, s\text{++}, \text{If}[\text{bx}[[s]] == 0 \| \text{bx}[[s]] > 3,\\
&\{\text{TimeVsVelX}[[\text{ii}]] = \{\text{KEx}[[\text{ii}]], \text{bins}[[s]]\}; \text{Break}[]; \}]];\\
&\text{sol} = \text{Delete}[\text{sol}, 1];)]
\end{aligned}
$$

Program to find polar molecule trap depth

The program calculates the trap depth for a dipolar molecule in an electrostatic trap as given in Fig. 2.23(b).

Molecular data:

dRbK = 0.615; dRbCs = 1.237; dKCs = 1.906;(*Debye*)

BRbK = 0.03839; BRbCs = 0.0169; BKCs = 0.03048;(*cmInv*)

Trap depth:

$J = 1$; Mj $= 0$;

dSqrByBRbK $= \frac{\text{dRbK}^2}{\text{BRbK}}$; dSqrByBRbCs $= \frac{\text{dRbCs}^2}{\text{BRbCs}}$; dSqrByBKCs $= \frac{\text{dKCs}^2}{\text{BKCs}}$;

dEmK[EF_, dSqrByB_]:=dSqrByB $* \frac{\text{DebyeToCm}^2}{\text{cmInvToJ}} * \text{EF}^2 * \frac{J(J+1)-3\text{Mj}^2}{2J*(J+1)*(2J-1)*(2J+3)} * \frac{10^3}{\text{kB}}$;

Plot3D $\left[\text{dEmK[EF, dSqrByB]}, \left\{\text{EF}, 10^4, 1.5*10^5\right\}, \{\text{dSqrByB}, 0, 150\}\right.$,

PlotRange $\rightarrow \{\{10^4, 1.5*10^5\}, \{0, 150\}, \{0, 13\}\}$,

AxesLabel $\rightarrow \left\{\text{Electric Field (kV/cm)}, "\frac{d^2}{B}\left(\text{Debye}^2 \middle/ \text{cm}^{-1}\right), \text{Trap Depth (mK)}\right\}$,

LabelStyle $\rightarrow$ Directive[Bold, FontFamily $\rightarrow$ Arial, FontSize $\rightarrow$ 20],

Ticks $\rightarrow \{\{\{20000, 0.2\}, \{40000, 0.4\}, \{60000, 0.6\}, \{80000, 0.8\}, \{100000, 1\}\}$,

$\{40, 80, 120, 160\}, \{2, 4, 6\}\}$,

Mesh $\rightarrow \{\{\{0, \text{Red}\}\}, \{\{\text{dSqrByBRbK}, \text{Directive[Thickness[0.005]]}\}$,

{dSqrByBRbCs, Directive[Dashed, Thickness[0.005]]},

{dSqrByBKCs, Directive[Black, Dotted, Thickness[0.005]]}}},

ImageSize $\rightarrow$ 900, ViewPoint $\rightarrow \{1, -2.2, 0.5\}]$

APPENDIX **C**

Numerical codes: molecular transitions

We provide the numerical codes in Mathematica to calculate the molecular continuum wave function, transition rate for bound to bound and bound to continuum transitions, branching ratio and the direct photo dissociation rate.

Constants and conversions:

Here we provide the physical constants, conversion factors and the ion trap potential which is common for the next programs.

Constants in SI units:

hcross $= 1.054571 * 10^{-34}$; mRbSI $= 1.409993199 * 10^{-25}$;

MURbSI $=$ mRbSI $*$ mRbSI$/($mRbSI $+$ mRbSI$)$;

eps0SI $= 8.854187817 * 10^{-12}$; c0SI $= 2.99792458 * 10^{8}$;

me $= 9.10938215 * 10^{-31}$; (*SI*)

Constants in atomic units (au):

mRbau $=$ SetPrecision $\left[\frac{\text{mRbSI}}{\text{me}}, 15\right]$; (*Rb mass atom in au *)

MURbau $=$ mRbau $*$ mRbau$/($mRbau $+$ mRbau$)$; (*Rb2 reduced mass in au*)

Conversions:

EnHartreeToCMinv $= 219474.63$; EnCMinvToJoule $= 1.98630 * 10^{-23}$;

EnJouleToCMinv $= 5.03445 * 10^{22}$;

Program to find the continuum wavefunction

The program solves the Schrodinger equation for nuclear motion of two colliding atoms using Numerov method as discussed in chapter 4.

PEC:

fid = OpenRead[F\\Work\\rb2+_1_1by2upot.txt];

V = ReadList[fid, {Number, Number}]; Close[fid];

fV = Interpolation[V];

Description of functions:

V : Potential energy in cm^{-1} vs meter.

KE : Kinetic energy in Joule; KEcm : Kinetic energy in cm^{-1}.

Nwf : unit normalised continuum wave function.

Numerov code:

g2[i_, j_]:=$\frac{2*\text{MURbSI}}{\text{hcross}^2} * (\text{fV}[\text{rmin} + (i-3) * \text{dx}] - \text{KE}[[j]])$

g1[i_, j_]:=$\frac{2*\text{MURbSI}}{\text{hcross}^2} * (\text{fV}[\text{rmin} + (i-2) * \text{dx}] - \text{KE}[[j]])$

g[i_, j_]:=$\frac{2*\text{MURbSI}}{\text{hcross}^2} * (\text{fV}[\text{rmin} + (i-1) * \text{dx}] - \text{KE}[[j]])$

KEcm = Table[$N[i]$, $\{i, 1, 16000, 1\}$];

KE = KEcm/EnJouleToCMinv; (*Joule*)

rmin = $2 * 10^{-10}$; rmax = $50 * 10^{-10}$; dx = $0.001 * 10^{-10}$;

Nx = (rmax − rmin)/dx + 1; posr50Ang = $\left(50 * 10^{-10} - \text{rmin}\right) / \text{dx} + 1$;

Off[InterpolatingFunction::dmval];

For[$j = 1, j \leq$ Dimensions[KEcm][[1]], j++,

psi = $\left\{\{\text{rmin}, 0\}, \left\{\text{rmin} + \text{dx}, 10^{-3}\right\}\right\}$;

For[$i = 3, i \leq$ Nx, i++,

AppendTo $\left[\text{psi}, \left\{\text{rmin} + (i-1) * \text{dx}, \frac{1}{1 - \frac{\left(g[i,j] * \text{dx}^2\right)}{12}} ((2 * \text{psi}[[i-1, 2]]) - \text{psi}[[i-2, 2]]\right.\right.$

$+\frac{\left(5*\text{g1}[i,j]*\text{psi}[[i-1,2]]*\text{dx}^2\right)}{6}+\frac{\text{g2}[i,j]*\text{psi}[[i-2,2]]*\text{dx}^2}{12}\Big)\Big\}\Big]\Big];$

$\text{dim} = \text{Dimensions}[\text{psi}][[1]] - 2; a = \{\}; b = \{\};$

$\text{For}[i = 1, i \leq \text{dim}, i{+}{+},$

$\text{If}[\text{Abs}[\text{psi}[[i,2]]] \leq \text{Abs}[\text{psi}[[i+1,2]]] \geq \text{Abs}[\text{psi}[[i+2,2]]],$

$\text{AppendTo}[a, \{\text{psi}[[i+1,1]], \text{Abs}[\text{psi}[[i+1,2]]]\}]]];$

$\text{Normfactor} = a[[\text{Dimensions}[a][[1]]]][[2]];$

$\text{Nwf} = \text{Table}\left[\left\{\text{psi}[[i,1]], \frac{\text{psi}[[i,2]]}{\text{Normfactor}}\right\}, \{i, 1, \text{posr50Ang}\}\right];$

$\text{fid} = \text{OpenWrite}[\text{F}\backslash\backslash\text{Work}\backslash\backslash\text{1\_1by2\_u\_} <> \text{ToString}[\text{KEcm}[[j]]] <> \text{CMI.txt}];$

$\text{Write}[\text{fid}, \text{Nwf}]; \text{Close}[\text{fid}];]$

Program to calculate spontaneous transition rate:

The program calculate the spontaneous emission rate from the excited bound vibrational state to the ground vibrational and free states.

Importing vibrational wavefunctions and TDM

```
Evex = {}; vibfnex = {};Evgn = {}; vibfngn = {};
fid = OpenRead["F\\Work\\molecule\\Vib_20u.txt"];
For[i = 1, i <= 291, i++,
line1=Read[fid,{String,String}];
Line1=Read[StringToStream[line1[[1]]],
{Word,Word,Number,Word,Number,Word,Number}];
AppendTo[Evex,{i-1,SetPrecision[Line1[[7]],8]}];
AppendTo[vibfnex, ReadList[fid, {Number, Number}]];] Close[fid];
fid = OpenRead["F\\Work\\molecule\\Vib_10g.txt"];
For[i = 1, i <= 124, i++,
line1=Read[fid,{String,String}];
Line1=Read[StringToStream[line1[[1]]],
{Word,Word,Number,Word,Number,Word,Number}];
```

AppendTo[Evgn, {i - 1, Read[fid, Number];}];

AppendTo[vibfngn, ReadList[fid, {Number, Number}]];] Close[fid];

fid2 = OpenRead["F\\Work\\molecule\\TDM_1_0g_2_0u.txt"];

TDM1 = ReadList[fid2, {Number, Number}]; Close[fid2];

fTDM1 = Interpolation[TDM1, InterpolationOrder -> 1];

Description of functions:

Evex: List of excited state vibrational energies in cm^{-1}

EvEx : excited state energy of the level considered (Vexc)

Evgn : List of ground state vibbrational energies in cm^{-1}

EvGn : ground state energy of the level considered (v)

vibfnex: list of vibrational wave function of the excited state Vs position in m

vibfngn : list of vibrational wave function of the ground state Vs position in m

vibfnexc : vibrational wave function of the excited state considered

vibfngnd : vibrational wave function of the ground state considered

TDM1 : transition dipole moment between the two states in Cm Vs m

KEJ : Kinetic energy in Joule; KECMI : Kinetic energy in cm^{-1}

gndcont : continuum wave function of the ground state.

Excited state vibrational level

Vexc = 252;

dim = Dimensions[vibfnex[[Vexc + 1]]][[1]];

EvEx = Evex[[Vexc + 1, 2]];

vibfnexc = vibfnex[[Vexc + 1]][[1 ;; dim - 1]];

r1exc = vibfnexc[[1, 1]]; r2exc = vibfnexc[[Dimensions[vibfnexc][[1]], 1]];

fexc = Interpolation[vibfnexc];

EnD2 = 12816.54678496(* from Steck*);

depthexc = 5920.074; depthgnd = 3994.1;

$$\text{SpConst} = 1 \Big/ \left(3\text{Pi} * \text{eps0SI} * \text{hcross} * \text{c0SI}^3\right);$$

Bound to bound spontaneous transition rate:

The program calculate the overlap integral between two bound vibrational wave functions and calculate the spontaneous emission rate from the excited to the ground vibrational state.

$$\text{gamap} = \{\}; \text{For}[v = 0, v \leq 123, v{+}{+},$$
$$\text{dim} = \text{Dimensions}[\text{vibfngn}[[v+1]]][[1]];$$
$$\text{EvGn} = \text{Evgn}[[v+1, 2]]; \text{vibfngnd} = \text{vibfngn}[[v+1]][[1;; \text{dim} - 1]];$$
$$\text{r1gnd} = \text{vibfngnd}[[1,1]]; \text{r2gnd} = \text{vibfngnd}[[\text{Dimensions}[\text{vibfngnd}][[1]], 1]];$$
$$\text{fgnd} = \text{Interpolation}[\text{vibfngnd}];$$
$$\text{Rmin} = \text{Max}[\text{r1exc}, \text{r1gnd}]; \text{Rmax} = \text{Min}[\text{r2exc}, \text{r2gnd}];$$
$$\text{If}[\text{Rmax} \leq \text{Rmin}, \text{AppendTo}[\text{gamap}, \{v, 0\}];,$$
$$\text{product} = \text{Table}[\{r, \text{fgnd}[r] * \text{fTDM1}[r] * \text{fexc}[r]\}, \{r, \text{Rmin}, \text{Rmax}, \text{dx}\}];$$
$$f = \text{Interpolation}[\text{product}, \text{InterpolationOrder} \rightarrow 2];$$
$$\text{I1} = \int_{\text{Rmin}}^{\text{Rmax}} f[r]\, dr;$$
$$\text{omega} = \frac{1}{\text{hcross}}(\text{EnD2} + (\text{depthgnd} - \text{EvGn}) - (\text{depthexc} - \text{EvEx})) * \text{EnCMinvToJoule};$$
$$\text{gamap} = \text{AppendTo}\left[\text{gamap}, \left\{v, \text{I1}^2 * \text{omega}^3 * \text{spconst}\right\}\right];\Big]\Big]$$

Bound to free spontaneous transition rate:

The program calculate the overlap integral between excited bound vibrational wave function and ground free wave function and calculate the spontaneous emission rate from the excited bound state to the ground free states.

$$\text{T1a} = \text{Table}[i, \{i, 20., 1000, 20\}]; \text{I11} = \{\};$$
$$\text{For}[i = 1, i \leq \text{Dimensions}[\text{T1a}][[1]], i{+}{+},$$
$$\text{fidcont}[i] = \text{OpenRead}[\text{F}\backslash\backslash\text{Work}\backslash\backslash\text{10g\_psi\_} <> \text{ToString}[\text{T1a}[[i]]] <> \text{uK.txt}];$$
$$\text{KEJ} = \text{Read}[\text{fidcont}[i], \text{Number}]; \text{KECMI} = \text{Read}[\text{fidcont}[i], \text{Number}];$$
$$\text{gndcont} = \text{Flatten}[\text{ReadList}[\text{fidcont}[i], \text{Expression}], 1]; \text{Close}[\text{fidcont}[i]];$$

$$\text{Enorm} = \sqrt{\frac{\sqrt{2*\text{MURbSI}}}{\text{Pi}*\text{hcross}*\sqrt{\text{KEJ}}}};$$

$$\text{r1gnd} = \text{gndcont}[[1,1]]; \text{r2gnd} = \text{gndcont}[[\text{Dimensions}[\text{gndcont}][[1]],1]];$$

$$\text{fgndcont} = \text{Interpolation}[\text{gndcont}];$$

$$\text{Rmin} = \text{Max}[\text{r1exc}, \text{r1gnd}]; \text{Rmax} = \text{Min}[\text{r2exc}, \text{r2gnd}];$$

$$\text{If}[\text{Rmax} \leq \text{Rmin}, \text{AppendTo}[\text{I11}, \{\text{KEJ}, 0\}];,$$

$$\text{product} = \text{Table}[\{r, \text{Enorm} * \text{fgndcont}[r] * \text{fTDM1}[r] * \text{fexc}[r]\}, \{r, \text{Rmin}, \text{Rmax}, \text{dx}\}];$$

$$f = \text{Interpolation}[\text{product}, \text{InterpolationOrder} \rightarrow 2];$$

$$\text{I1} = \int_{\text{Rmin}}^{\text{Rmax}} f[r]\, dr;$$

$$\text{omega} = \frac{1}{\text{hcross}}(\text{EnD2} - \text{KECMI} - (\text{depthexc} - \text{EvEx})) * \text{EnCMinvToJoule};$$

$$\text{AppendTo}\left[\text{I11}, \left\{\text{KEJ}, \text{I1}^2 * \text{omega}^3 * \text{SpConst}\right\}\right];\Big]$$

$$\text{NTMAX} = \text{Dimensions}[\text{I11}][[1]];$$

$$\text{f1} = \text{Interpolation}[\text{I11}, \text{InterpolationOrder} \rightarrow 1];$$

$$\text{GamaSp} = \int_{\text{I11}[[1,1]]}^{\text{I11}[[\text{NTMAX}]][[1]]} \text{f1}[r]\, dr;$$

Branching Ratio:

The program calculate the branching ratio of spontaneous emission from an excited state vibrational level to the ground state bound and free states.

$$\text{Vexc} = 0;\ \text{Gvv} = \text{gamap};\ \text{GvvTotal} = \text{Total}[\text{gamap}[[\text{All},2]]];$$

$$\text{GamaTotal} = \text{SetPrecision}[\text{GvvTotal} + \text{GamaSp}, 8];$$

$$\text{BR1} = \text{Transpose}[\{\text{Gvv}[[\text{All},1]], \text{Gvv}[[\text{All},2]]/\text{GamaTotal}\}];$$

$$\text{bb} = \text{SetPrecision}\left[\frac{\text{Gamapbb}}{\text{Gamaptotal}}, 8\right]; \text{bc} = 1 - \text{bb};$$

pp1 = BarChart[BR1[[All, 2]], BarSpacing -> 0, ChartStyle -> Darker[Blue], PlotRange -> {{0, 125}, {-0.02, 0.2}}, ChartLabels -> CL, LabelStyle -> Directive[22], ImageSize -> 400, Frame -> False, GridLines -> {{20, 40, 60, 80, 100, 120}, None}, GridLinesStyle -> Directive[Thickness[0.005], Black, Dotted], FrameTicks -> {{Automatic, None}, {None, None}}, FrameStyle -> Directive[Black, Thickness[0.004], FontSize -> 20, FontFamily -> "Arial"], PlotLabel -> Style["v'=0", 20]];

Direct photo dissociation rate

The program calculate the direct photo dissociation rate from a bound vibrational level in the ground state to the free states of the dissociating electronic state (the transition is allowed when both the electronic states have the same multiplicity).

Energy levels and TDM

depthg = 6194.48487800;

fid = OpenRead[“F\\Work\\molecule\\Vib_1by2g.txt”];

EBound = {}; wfBound1 = {};

For[i = 1, i <= 273, i++, line1 = Read[fid, {String, String}];

Line1 = Read[StringToStream[line1[[1]]],

{Word, Word, Number, Word, Number, Word, Number}];

AppendTo[EBound, {i - 1, SetPrecision[Line1[[7]], 8]}];

Off[ReadList::readn];

AppendTo[wfBound1, ReadList[fid, {Number, Number}]];

] Close[fid]; Clear[line1, Line1];

fid2 = OpenRead[path4 <> “TDM_1_1by2g_1_1by2u.txt”];

TDM2 = SetPrecision[ReadList[fid2, {Number, Number}], 8]; Close[fid2];

fTDM2 = Interpolation[TDM2, InterpolationOrder -> 1];

Description of functions:

EBound : List of ground state vibrational energies in cm^{-1}

EvBound : ground state energy of the level considered (Vbnd)

wfBound1 : list of vibrational wave function of the ground state Vs position in au

wfBound : vibrational wave function of the ground state considered

TDM2 : transition dipole moment between the two states in au

KEcm : Kinetic energy in cm^{-1}; KEau: Kinetic energy in Hartree

wfCont : continuum wave function of the dissociating state Vs position in au

bound vibrational level

Vbnd = 174;

dim = Dimensions[wfBound1[[Vbnd + 1]]][[1]];

EvBound = EBound[[Vbnd + 1, 2]];

wfBound = wfBound1[[Vbnd + 1]][[1 ;; dim - 1]];

r1bnd = wfBound[[1, 1]]; r2bnd = wfBound[[Dimensions[wfBound][[1]], 1]];

fbnd = Interpolation[wfBound]; Off[InterpolatingFunction::dmval];

dx = 0.001 (*au*);

Continuum wavefunction

bindingenergy = depthg − EvBound;

KEcm = Table[$N[i]$, $\{i, 5, 15000, 10\}$]; (*cm^{-1}*)

KEau = KEcm/EnHartreeToCMinv;

dEinau = KEau + (bindingenergy/EnHartreeToCMinv);

Cross section

I11 = {}; sigma = {};

For[$i = 1, i \leq$ Dimensions[KEcm][[1]], i++,

fid = OpenRead[F\\Work\\1_1by2_u_ <> ToString[KEcm[[i]]] <> CMI.txt];

wfCont = Flatten[ReadList[fid, Expression], 1]; Close[fid];

Enorm = $\sqrt{\frac{\sqrt{2*\mathrm{MURbau}}}{\mathrm{Pi}*\sqrt{\mathrm{KEau}[[i]]}}}$;

r1cont = N[wfCont[[1, 1]]]; r2cont = wfCont[[Dimensions[wfCont][[1]], 1]];

fcont = Interpolation[wfCont];

Rmin = Max[r1bnd, r1cont]; Rmax = Min[r2bnd, r2cont];

product = Table[$\{r,$ Enorm $*$ fcont$[r] *$ fbnd$[r] *$ fTDM2$[r]\}$, $\{r,$ Rmin, Rmax, dx$\}$];

f = Interpolation[product, InterpolationOrder $\rightarrow$ 2, Method $\rightarrow$ Hermite];

I1 = $\int_{\mathrm{Rmin}}^{\mathrm{Rmax}} f[r]\, dr$;

AppendTo[sigma, {dEinau[[i]] $*$ EnHartreeToCMinv,

$2.69 * 10^{-18} * \text{dEinau}[[i]] * \text{I1}^2\Big\}\Big]\,;\Big]$ (*cm^{-1}vs cm^2*)

Rate

power $= 40 * 10^{-3}$; (*W*)

BeamRadius $= 0.4$; (*cm*)

flux $=$ Table $\left[\frac{\text{power}}{\text{Pi}*\text{BeamRadius}^2*\text{sigma}[[i,1]]*\text{EnCMinvToJoule}},\right.$
$\{i, 1, \text{Dimensions}[\text{sigma}][[1]]\}]$; (*$\frac{\text{photon}}{\text{cm}^2 s}$*)

rate $=$ Table$[\{\text{sigma}[[i,1]], \text{sigma}[[i,2]] * \text{flux}[[i]]\},$
$\{i, 1, \text{Dimensions}[\text{sigma}][[1]]\}]$(*Hz*);

Behlke high voltage switch

We provide the circuit diagram for the Behlke high voltage switch used for switching the ion trap extraction voltages.

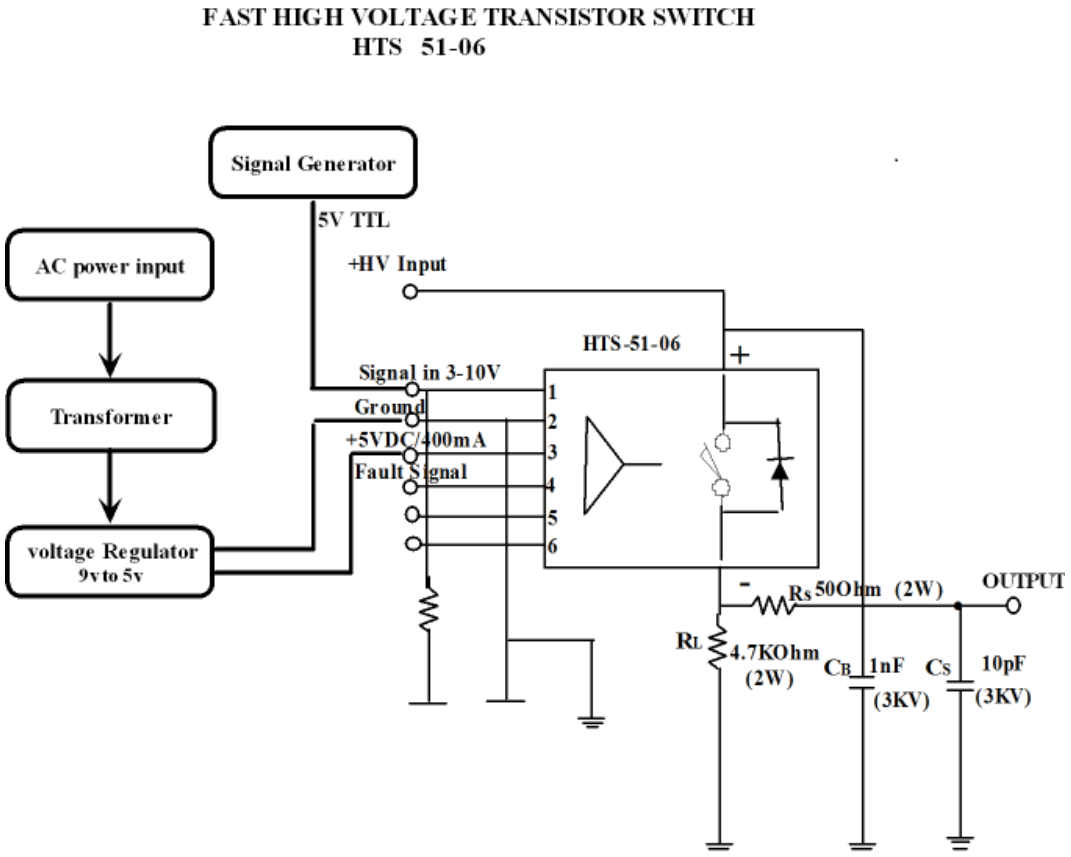

Bibliography

[1] Winthrop W. Smith, Oleg P. Makarov, and Jian Lin. Cold ion neutral collisions in a hybrid trap. *Journal of Modern Optics*, 52(16):2253–2260, 2005.

[2] Andrew T. Grier, Marko Cetina, Fedja Oručević, and Vladan Vuletić. Observation of cold collisions between trapped ions and trapped atoms. *Phys. Rev. Lett.*, 102:223201, Jun 2009.

[3] I. Sivarajah, D. S. Goodman, J. E. Wells, F. A. Narducci, and W. W. Smith. Evidence of sympathetic cooling of Na^+ ions by a Na magneto-optical trap in a hybrid trap. *Phys. Rev. A*, 86:063419, Dec 2012.

[4] K. Ravi, Seunghyun Lee, Arijit Sharma, G. Werth, and S.A. Rangwala. Cooling and stabilization by collisions in a mixed ion-atom system. *Nat Commun*, 3:1126, 2012.

[5] Felix H. J. Hall and Stefan Willitsch. Millikelvin reactive collisions between sympathetically cooled molecular ions and laser-cooled atoms in an ion-atom hybrid trap. *Phys. Rev. Lett.*, 109:233202, Dec 2012.

[6] Christoph Zipkes, Stefan Palzer, Carlo Sias, and Michael Kohl. A trapped single ion inside a Bose-Einstein condensate. *Nature*, 464:388–391, 2010.

[7] Stefan Schmid, Arne Härter, and Johannes Hecker Denschlag. Dynamics of a cold trapped ion in a Bose-Einstein condensate. *Phys. Rev. Lett.*, 105:133202, Sep 2010.

[8] Felix H. J. Hall, Mireille Aymar, Maurice Raoult, Olivier Dulieu, and Stefan Willitsch. Light-assisted cold chemical reactions of barium ions with rubidium atoms. *Molecular Physics*, 111(12-13):1683–1690, 2013.

[9] Steven Chu, L. Hollberg, J. E. Bjorkholm, Alex Cable, and A. Ashkin. Three-dimensional viscous confinement and cooling of atoms by resonance radiation pressure. *Phys. Rev. Lett.*, 55:48–51, Jul 1985.

[10] E. L. Raab, M. Prentiss, Alex Cable, Steven Chu, and D. E. Pritchard. Trapping of neutral sodium atoms with radiation pressure. *Phys. Rev. Lett.*, 59:2631–2634, Dec 1987.

[11] M. H. Anderson, J. R. Ensher, M. R. Matthews, C. E. Wieman, and E. A. Cornell. Observation of Bose-Einstein condensation in a dilute atomic vapor. *Science*, 269(5221):198–201, 1995.

[12] K. B. Davis, M. O. Mewes, M. R. Andrews, N. J. van Druten, D. S. Durfee, D. M. Kurn, and W. Ketterle. Bose-Einstein condensation in a gas of Sodium atoms. *Phys. Rev. Lett.*, 75:3969–3973, Nov 1995.

[13] F. G. Major V. N. Gheorghe and G Werth. *Charged particle traps*. Springer-Verlag Berlin Heidelberg, 2005.

[14] K. Ravi, S. Lee, A. Sharma, G. Werth, and S.A. Rangwala. Combined ion and atom trap for low-temperature ion-atom physics. *Applied Physics B*, 107(4):971–981, 2012.

[15] J. F. Barry, D. J. McCarron, E. B. Norrgard, M. H. Steinecker, and D. DeMille. Magneto-optical trapping of a diatomic molecule. *Nature*, 512:286–289, 2014.

[16] D. DeMille. Quantum computation with trapped polar molecules. *Phys. Rev. Lett.*, 88:067901, Jan 2002.

[17] M. A. Baranov, M. Dalmonte, G. Pupillo, and P. Zoller. Condensed matter theory of dipolar quantum gases. *Chemical Reviews*, 112(9):5012–5061, 2012. PMID: 22877362.

[18] Tridib Ray, Arijit Sharma, S. Jyothi, and S. A. Rangwala. Temperature measurement of laser-cooled atoms using vacuum rabi splitting. *Phys. Rev. A*, 87:033832, Mar 2013.

[19] Tridib Ray, S. Jyothi, N.Bhargava Ram, and S.A. Rangwala. A thin wire ion trap to study ionatom collisions built within a fabryperot cavity. *Applied Physics B*, 114(1-2):267–273, 2014.

[20] S. Jyothi, T. Ray, N. Bhargava Ram, and S. A. Rangwala. Hybrid ion, atom and light trap. *ArXiv e-prints*, December 2013.

[21] Tridib Ray. *Progression towards study of interactions with composite ssystem at ultracold temperature*. PhD thesis, Raman Research Institute, 2015.

[22] G. S. Agarwal and P. K. Pathak. dc-field-induced enhancement and inhibition of spontaneous emission in a cavity. *Phys. Rev. A*, 70:025802, Aug 2004.

[23] J. Kleinert, C. Haimberger, P. J. Zabawa, and N. P. Bigelow. Trapping of ultracold polar molecules with a thin-wire electrostatic trap. *Phys. Rev. Lett.*, 99:143002, Oct 2007.

[24] Abdul-Rahman Allouche and Monique Aubert-Frécon. Transition dipole moments between the low-lying $\omega g, u(+/-)$ states of the Rb_2 and Cs_2 molecules. *The Journal of Chemical Physics*, 136(11):–, 2012.

[25] B. Bussery and M. Aubert-Frécon. Potential energy curves and vibration-rotation energies for the two purely long-range bound states 1_u and 0_g^- of the alkali dimers M_2 dissociating to $M(ns^2S_{1/2}) + M(np^2P_{3/2})$ with $M = Na, K, Rb$, and Cs. *Journal of Molecular Spectroscopy*, 113(1):21 – 27, 1985.

[26] C. Amiot. Laser induced fluorescence of Rb_2: The $(1)^1\sigma_g^+(X)$, $(2)^1\sigma_g^+$, $(1)^1\pi_u(B)$, $(1)^1\pi_g$, and $(2)^1\pi_u(C)$ electronic states. *The Journal of Chemical Physics*, 93(12):8591–8604, 1990.

[27] R. J. Le Roy. *LEVEL 8.0: A Computer Program for Solving the Radial Schrödinger Equation for Bound and Quasibound Levels*. University of Waterloo Chemical Physics Research Report CP-663, 2007. see http://leroy.uwaterloo.ca/programs/.

[28] S. Jyothi, Tridib Ray, and S.A. Rangwala. Phase-sensitive radial extraction and mass spectrometry of trapped ions in a compact geometry. *Applied Physics B*, 118(1):131–138, 2015.

[29] Edgar Everhart, R. J. Carbone, and Gerald Stone. Differential cross-section measurements for large-angle collisions of helium, neon, and argon ions with argon atoms at energies to 100 kev. *Phys. Rev.*, 98:1045–1049, May 1955.

[30] T. S. Stein, W. E. Kauppila, V. Pol, J. H. Smart, and G. Jesion. Measurements of total scattering cross sections for low-energy positrons and electrons colliding with helium and neon atoms. *Physical Rev A*, 17:1600, 1978.

[31] S A Rangwala, S V K Kumar, E Krishnakumar, and N J Mason. Cross sections for the dissociative electron attachment to ozone. *J. Phys. B: At. Mol. Opt. Phys.*, 32:3795, 1999.

[32] H. Winter. Collisions of atoms and ions with surfaces under grazing incidence. *Physics Reports*, 367:387, 2002.

[33] J.D. Jackson. *Classical Electrodynamics*. Wiley, New York, 1975.

[34] G. Graff, F. G. Major, R. W. H. Roeder, and G. Werth. Method for measuring the cyclotron and spin resonance of free electrons. *Phys. Rev. Lett.*, 21:340, 1968.

[35] Thomas Beier, Hartmut Häffner, Nikolaus Hermanspahn, Savely G. Karshenboim, H.-Jürgen Kluge, Wolfgang Quint, Stefan Stahl, José Verdú, and Günther Werth. New determination of the electron's mass. *Phys. Rev. Lett.*, 88:011603, Dec 2001.

[36] Raymond E. March. An introduction to quadrupole ion trap massspectrometry. *Journal of Mass Spectrometry*, 32:351, 1997.

[37] W. Neuhauser, M. Hohenstatt, P. Toschek, and H. Dehmelt. Optical-sideband cooling of visible atom cloud confined in parabolic well. *Phys. Rev. Lett.*, 41:233–236, Jul 1978.

[38] K. Blaum, Yu. N. Novikov, and G. Werth. Penning traps as a versatile tool for precise experiments in fundamental physics. *Contemporary Physics*, 51(2):149–175, 2010.

[39] F. Diedrich, E. Peik, J. M. Chen, W. Quint, and H. Walther. Observation of a phase transition of stored laser-cooled ions. *Phys. Rev. Lett.*, 59:2931–2934, Dec 1987.

[40] D. J. Wineland, J. C. Bergquist, Wayne M. Itano, J. J. Bollinger, and C. H. Manney. Atomic-ion coulomb clusters in an ion trap. *Phys. Rev. Lett.*, 59:2935–2938, Dec 1987.

[41] S. A. Diddams, Th. Udem, J. C. Bergquist, E. A. Curtis, R. E. Drullinger, L. Hollberg, W. M. Itano, W. D. Lee, C. W. Oates, K. R. Vogel, and D. J. Wineland. An optical clock based on a single trapped $^{199}Hg^{+}$ ion. *Science*, 293(5531):825–828, 2001.

[42] Rosenband. T. et.al. Frequency ratio of Al^{+} and Hg^{+} single-ion optical clocks; metrology at the 17th decimal place. *Science*, 319(5871):1808–1812, 2008.

[43] D. Leibfried, R. Blatt, C. Monroe, and D. Wineland. Quantum dynamics of single trapped ions. *Rev. Mod. Phys.*, 75:281–324, Mar 2003.

[44] Wineland David Blatt, Rainer. Entangled states of trapped atomic ions. *Nature*, 453:1008–1015, 2008.

[45] Wolfgang Paul. Electromagnetic traps for charged and neutral particles. *Rev. Mod. Phys.*, 62:531–540, Jul 1990.

[46] Hans Dehmelt. Experiments with an isolated subatomic particle at rest. *Rev. Mod. Phys.*, 62:525–530, Jul 1990.

[47] D.M. Stamper-Kurn W. Ketterle, D.S. Durfee. *Proceedings of the International School of Physics Enrico Fermi", Course CXL*, pages 67–176, 1999.

[48] Anthony J. Leggett. Bose-Einstein condensation in the alkali gases: Some fundamental concepts. *Rev. Mod. Phys.*, 73:307–356, Apr 2001.

[49] L. Isenhower, E. Urban, X. L. Zhang, A. T. Gill, T. Henage, T. A. Johnson, T. G. Walker, and M. Saffman. Demonstration of a neutral atom controlled-NOT quantum gate. *Phys. Rev. Lett.*, 104:010503, Jan 2010.

[50] D Blume. Few-body physics with ultracold atomic and molecular systems in traps. *Reports on Progress in Physics*, 75(4):046401, 2012.

[51] H. R. Thorsheim, J. Weiner, and P. S. Julienne. Laser-induced photoassociation of ultracold sodium atoms. *Phys. Rev. Lett.*, 58:2420–2423, Jun 1987.

[52] P. D. Lett, K. Helmerson, W. D. Phillips, L. P. Ratliff, S. L. Rolston, and M. E. Wagshul. Spectroscopy of Na_2 by photoassociation of laser-cooled Na. *Phys. Rev. Lett.*, 71:2200–2203, Oct 1993.

[53] R. A. Cline, J. D. Miller, and D. J. Heinzen. Study of Rb_2 long-range states by high-resolution photoassociation spectroscopy. *Phys. Rev. Lett.*, 73:632–635, Aug 1994.

[54] John Weiner, Vanderlei S. Bagnato, Sergio Zilio, and Paul S. Julienne. Experiments and theory in cold and ultracold collisions. *Rev. Mod. Phys.*, 71:1, 1999.

[55] Nicholas R. Hutzler, Hsin-I Lu, and John M. Doyle. The buffer gas beam: An intense, cold, and slow source for atoms and molecules. *Chemical Reviews*, 112(9):4803–4827, 2012. PMID: 22571401.

[56] S. A. Rangwala, T. Junglen, T. Rieger, P. W. H. Pinkse, and G. Rempe. Continuous source of translationally cold dipolar molecules. *Phys. Rev. A*, 67:043406, Apr 2003.

[57] T. Rieger, T. Junglen, S. A. Rangwala, P. W. H. Pinkse, and G. Rempe. Continuous loading of an electrostatic trap for polar molecules. *Phys. Rev. Lett.*, 95:173002, Oct 2005.

[58] T. Junglen, T. Rieger, S. A. Rangwala, P. W. H. Pinkse, and G. Rempe. Two-dimensional trapping of dipolar molecules in time-varying electric fields. *Phys. Rev. Lett.*, 92:223001, Jun 2004.

[59] Hendrick L. Bethlem, Giel Berden, and Gerard Meijer. Decelerating neutral dipolar molecules. *Phys. Rev. Lett.*, 83:1558–1561, Aug 1999.

[60] Edvardas Narevicius, Adam Libson, Christian G. Parthey, Isaac Chavez, Julia Narevicius, Uzi Even, and Mark G. Raizen. Stopping supersonic oxygen with a series of pulsed electromagnetic coils: A molecular coilgun. *Phys. Rev. A*, 77:051401, May 2008.

[61] Michael S Elioff, James J. Valentini, and David W. Chandler. Subkelvin cooling NO molecules via "billiard-like" collisions with Argon. *Science*, 302(5652):1940–1943, 2003.

[62] B. K. Stuhl, M. T. Hummon, M. Yeo, G. Quemener, J. L. Bohn, and J Ye. Evaporative cooling of the dipolar hydroxyl radical. *Nature*, 492:396–400, 2012.

[63] M. Zeppenfeld, B. G. U. Englert, R. Glockner, A. Prehn, M. Mielenz, C. Sommer, L. D. van Buuren, M. Motsch, and G. Rempe. Sisyphus cooling of electrically trapped polyatomic molecules. *Nature*, 491:570–573, 2012.

[64] A. V. Avdeenkov and John L. Bohn. Linking ultracold polar molecules. *Phys. Rev. Lett.*, 90:043006, Jan 2003.

[65] J. J. Hudson, B. E. Sauer, M. R. Tarbutt, and E. A. Hinds. Measurement of the electron electric dipole moment using YbF molecules. *Phys. Rev. Lett.*, 89:023003, Jun 2002.

[66] L. A. Lugiato. *Progress in Optics, edited by E. Wolf*, XXI:70, 1984.

[67] Arijit Sharma, Tridib Ray, Rahul V. Sawant, G. Sheikholeslami, S. A. Rangwala, and D. Budker. Optical control of resonant light transmission for an atom-cavity system. *Phys. Rev. A*, 91:043824, Apr 2015.

[68] D. Goorskey H. Wang and M. Xiao. *Phys. Rev. A*, 65:051802(R), 2002.

[69] J. McKeever, A. Boca, A. D. Boozer, R. Miller, J. R. Buck, A. Kuzmich, and H. J. Kimble. Deterministic generation of single photons from one atom trapped in a cavity. *Science*, 303(5666):1992–1994, 2004.

[70] Matthias Keller, Birgit Lange, Kazuhiro Hayasaka, Wolfgang Lange, and Herbert Walther. Continuous generation of single photons with controlled waveform in an ion-trap cavity system. *Nature*, 431:1075, 2004.

[71] Peter F. Herskind, Aurelien Dantan, Joan P. Marler, Magnus Albert, and Michael Drewsen. Realization of collective strong coupling with ion coulomb crystals in an optical cavity. *Nat Phys*, 5:494, 2009.

[72] Thibault Peyronel, Ofer Firstenberg, Qi-Yu Liang, Sebastian Hofferberth, Alexey V. Gorshkov, Thomas Pohl, Mikhail D. Lukin, and Vladan Vuletic. Quantum nonlinear optics with single photons enabled by strongly interacting atoms. *Nature*, 488:57, 2012.

[73] J. M. Raimond, M. Brune, and S. Haroche. Manipulating quantum entanglement with atoms and photons in a cavity. *Rev. Mod. Phys.*, 73:565–582, Aug 2001.

[74] Tatjana Wilk, Simon C. Webster, Axel Kuhn, and Gerhard Rempe. Single-atom single-photon quantum interface. *Science*, 317(5837):488–490, 2007.

[75] H. G. Dehmelt and F. G. Major. Orientation of $(He^4)^+$ ions by exchange collisions with Cesium atoms. *Phys. Rev. Lett.*, 8:213–214, Mar 1962.

[76] J. R. Peterson and D. C. Lorents. Total charge-transfer cross sections for He^+ and Ar^+ on K, Rb, and Cs: Near-resonant reactions leading to excited final states. *Phys. Rev.*, 182:152–161, Jun 1969.

[77] Seunghyun Lee, K. Ravi, and S. A. Rangwala. Measurement of collisions between rubidium atoms and optically dark rubidium ions in trapped mixtures. *Phys. Rev. A*, 87:052701, May 2013.

[78] Michael Baer and Cheuk Y. Ng. A three-dimensional quantum mechanical study of the $H_2 + H_2^+$ system: Calculation of reactive and charge transfer cross sections. *The Journal of Chemical Physics*, 93(11):7787–7799, 1990.

[79] J.-P. Karr, A. Douillet, and L. Hilico. Photodissociation of trapped H_2^+ ions for REMPD spectroscopy. *Applied Physics B*, 107(4):1043–1052, 2012.

[80] J. E. Pollard, L. K. Johnson, D. A. Lichtin, and R. B. Cohen. State-selected reactive scattering. I. $H_2^+ + H_2 \rightarrow H_3^+ + H$. *The Journal of Chemical Physics*, 95(7):4877–4893, 1991.

[81] V. S. Lebedev, L. P. Presnyakov, and I. I. Sobelman. Photodissociative absorption by H_2^+ in the solar photosphere. *Astronomy Reports*, 44:338, 2000.

[82] Matthias Weidermuller and Claus Zimmermann, editors. *Cold Atoms and Molecules*. Wiley-VCH Verlag GmbH & Co., 2009.

[83] Daniel A. Steck. *Classical and Modern Optics*. June 2008.

[84] Daniel A. Steck. Rubidium 85 D line data. 19 September, 2012.

[85] L. Ricci, M. Weidemüller, T. Esslinger, A. Hemmerich, C. Zimmermann, Vladan Vuletić, W. König, and T.W. Hänsch. A compact grating-stabilized diode laser system for atomic physics. *Optics Communications*, 117(56):541 – 549, 1995.

[86] K. Ravi. *Trapping and Cooling of Ions and the Study of Ion Atom Interactions*. PhD thesis, Raman Research Institute, 2012.

[87] D. A. Dahl. *Simion 3D Version 7.0 User Manual. Bechtel BWXT, Idaho*. 2000.

[88] M. Aymar and O. Dulieu. Calculation of accurate permanent dipole moments of the lowest $^{1,3}\sigma^+$ states of heteronuclear alkali dimers using extended basis sets. *The Journal of Chemical Physics*, 122(20):–, 2005.

[89] S. Rousseau, A.R. Allouche, and M. Aubert-Frcon. Theoretical study of the electronic structure of the KRb molecule. *Journal of Molecular Spectroscopy*, 203(2):235 – 243, 2000.

[90] A R Allouche, M Korek, K Fakherddin, A Chaalan, M Dagher, F Taher, and M Aubert-Frécon. Theoretical electronic structure of RbCs revisited. *Journal of Physics B: Atomic, Molecular and Optical Physics*, 33(12):2307, 2000.

[91] R. Ferber, I. Klincare, O. Nikolayeva, M. Tamanis, H. Knöckel, E. Tiemann, and A. Pashov. The ground electronic state of KCs studied by fourier transform spectroscopy. *The Journal of Chemical Physics*, 128(24):–, 2008.

[92] M. Holzki. Untersuchung von gekoppelten nichtlinearen oscillationen einer ionenwolke in ionenfallen. Master's thesis, Johannes Gutenberg University, Mainz, 1997.

[93] I. N. Levine. *Quantum Chemistry*. Pearson Education Inc., New Jersey,U.S.A., 2009.

[94] R. D. Cowan. *The theory of atomic structure and spectra*. University of California Press, California, 1981.

[95] H. Friedrich. *Theoretical Atomic Physics*. Springer-Verlag, Berlin, Heidelberg, 2006.

[96] J. D. Miller, R. A. Cline, and D. J. Heinzen. Photoassociation spectrum of ultracold Rb atoms. *Phys. Rev. Lett.*, 71:2204–2207, Oct 1993.

[97] E. R. I. Abraham, N. W. M. Ritchie, W. I. McAlexander, and R. G. Hulet. Photoassociative spectroscopy of long range states of ultracold $^6Li_2$ and $^7Li_2$. *The Journal of Chemical Physics*, 103(18):7773–7778, 1995.

[98] H. Wang, P. L. Gould, and W. C. Stwalley. Photoassociative spectroscopy of ultracold ^{39}K atoms in a high-density vapor-cell magneto-optical trap. *Phys. Rev. A*, 53:R1216–R1219, Mar 1996.

[99] Bediha Beser, V. B. Sovkov, J. Bai, E. H. Ahmed, C. C. Tsai, F. Xie, Li Li, V. S. Ivanov, and A. M. Lyyra. Experimental investigation of the $^{85}Rb_2$ a $^3\sigma_u^+$ triplet ground state: Multiparameter morse long range potential analysis. *The Journal of Chemical Physics*, 131(9):–, 2009.

[100] Bing Ji, Chin-Chun Tsai, and William C. Stwalley. Proposed modification of the criterion for the region of validity of the inverse-power expansion in diatomic long-range potentials. *Chemical Physics Letters*, 236(3):242 – 246, 1995.

[101] H. M. J. M. Boesten, C. C. Tsai, B. J. Verhaar, and D. J. Heinzen. Observation of a shape resonance in cold-atom scattering by pulsed photoassociation. *Phys. Rev. Lett.*, 77:5194–5197, Dec 1996.

[102] T Bergeman, J Qi, D Wang, Y Huang, H K Pechkis, E E Eyler, P L Gould, W C Stwalley, R A Cline, J D Miller, and D J Heinzen. Photoassociation of ^{85}Rb atoms into 0_u^+ states near the 5S + 5P atomic limits. *Journal of Physics B: Atomic, Molecular and Optical Physics*, 39(19):S813, 2006.

[103] A. Jraij, A.R. Allouche, M. Korek, and M. Aubert-Frécon. Theoretical electronic structure of the alkali-dimer cation Rb_2^+. *Chemical Physics*, 290(23):129 – 136, 2003.

[104] C. Gabbanini, A. Fioretti, A. Lucchesini, S. Gozzini, and M. Mazzoni. Cold rubidium molecules formed in a magneto-optical trap. *Phys. Rev. Lett.*, 84:2814–2817, Mar 2000.

[105] A. R. L. Caires, V. A. Nascimento, D. C. J. Rezende, V. S. Bagnato, and L. G. Marcassa. Atomic density and light intensity dependences of the Rb_2 molecule formation rate constant in a magneto-optical trap. *Phys. Rev. A*, 71:043403, Apr 2005.

[106] Zhang Hong-Shan, Ji Zhong-Hua, Yuan Jin-Peng, Zhao Yan-Ting, Ma Jie, Wang Li-Rong, Xiao Lian-Tuan, and Jia Suo-Tang. Cold cesium molecules produced directly in a magneto-optical trap. *Chinese Physics B*, 20(12):123702, 2011.

[107] Abdul-Rahman Allouche. Private communication.

[108] Ewine F. van Dishoeck and Ruud Visser. *Laboratory Astrochemistry From Molecules through Nanoparticles to Grains*. Weinheim: Wiley-VCH, 2015.

[109] Gordon H. Dunn. Photodissociation of H_2^+ and D_2^+: Theory. *Physical Review*, 172:1, 1969.

[110] M. A. Bellos, R. Carollo, J. Banerjee, M. Ascoli, A.-R. Allouche, E. E. Eyler, P. L. Gould, and W. C. Stwalley. Upper bound to the ionization energy of $^{85}Rb_2$. *Phys.Rev.A*, 87:012508, 2013.